Technische Universität München
TUM School of Natural Sciences

ℸℸⅅℸ

Development and Validation of a
3D Neutron Therapy Treatment Planning Software for FRM II

Lucas Benedikt Sommer

Vollständiger Abdruck der von der TUM School of Natural Sciences der Technischen

Universität München zur Erlangung eines

Doktors der Naturwissenschaften (Dr. rer. nat.)

genehmigten Dissertation.

Vorsitz: Prof. Dr. Martin Zacharias

Prüfer*innen der Dissertation:

  1.   Prof. Dr. Jan J. Wilkens
  2.   Prof. Dr. Franz Pfeiffer

Die Dissertation wurde am 11.08.2022 bei der Technischen Universität München eingereicht

und durch die TUM School of Natural Sciences am 25.11.2022 angenommen.

DEPARTMENT OF PHYSICS

TECHNICAL UNIVERSITY OF MUNICH

Dissertation

Development and Validation of a 3D Neutron Therapy Treatment Planning Software for FRM II

Lucas Sommer

DEPARTMENT OF PHYSICS

TECHNICAL UNIVERSITY OF MUNICH

Dissertation

Development and Validation of a 3D Neutron Therapy Treatment Planning Software for FRM II

Entwicklung und Validierung einer 3D Bestrahlungsplanungssoftware für Neutronentherapie am FRM II

Author:	Lucas Sommer
Supervisor:	Prof. Dr. Jan J. Wilkens
Advisor:	Prof. Dr. Stephanie E. Combs
Mentor:	Dr. Tobias Chemnitz
Submission Date:	August 8th, 2022

Abstract

For the success of radiation oncology, treatment planning software is essential. While software for 3D dose calculation is commercially available for external radiation therapy with photons, ions, and also accelerator-based fast neutrons, no ready-to-use dose calculation software existed so far that could incorporate the particular characteristics of the Munich fission neutron therapy facility MEDAPP.

The mixed neutron-photon radiation field from the fission reactions providing neutrons for treatment and to a minor degree also the spatial extension of the reactor-based source made the development of a customized solution necessary. In the scope of the development of a treatment planning software for MEDAPP, the biological properties of neutron radiation in reference to photon radiation also needed to be addressed. The goal of the presented project was therefore to overcome the lack of patient-specific dose calculation abilities for MEDAPP and to also include biological modeling of the applied mixed neutron-photon treatment field.

For the calculation of physical dose, two approaches - well established in treatment planning - were realized in two separate dose engines. The first one is based on Monte Carlo simulations applying the Monte Carlo N-Particle code MCNP for radiation transport through the patient. Here, characteristics of the beamline can also be taken into account. For biological modeling according to the repair-misrepair-fixation model, the Monte Carlo Damage Simulation MCDS was included in this first dose engine. The second approach is based on decomposed pencil beam kernels originally developed for photon radiation. Pencil beam kernels are also applicable for fast neutrons when adequate correction methods for tissue heterogeneities are included.

A comparison of Monte Carlo dose calculations with dose measurements in water showed overall good results. For heterogeneous media, results of calculated dose deposition from neutrons showed tissue-dependent characteristics as expected from general considerations but could not be cross-checked with measurements. While the included biological modeling reproduces measured trends, results of the comparison need to be handled carefully. For the pencil beam approach, dose calculations showed reasonable agreement with Monte Carlo calculations.

It is discussed in the presented thesis that the Monte Carlo dose engine is expected to give accurate patient-specific results that provide high potential especially for retrospective studies. Here, the provided modeling of biological properties could also be included and investigated further. Leaving aside regulatory considerations for medical devices, a combination of the accurate Monte Carlo and the time-efficient pencil beam approaches would in principle provide a planning tool suited for prospective planning.

Kurzdarstellung

Bestrahlungsplanungssoftware ist eine essentielle Komponente für den Behandlungserfolg in der Strahlentherapie. So gibt es für die Teletherapie mit Photonen, Ionen und mit Hilfe von Teilchenbeschleunigern erzeugten schnellen Neutronen kommerziell verfügbare Software für die Dosisberechnung. Auf Grund der Eigenheiten der Spaltneutronenquelle MEDAPP am Münchner Forschungsreaktor FRM II war dort eine solche Software für die Dosisberechnung bisher nicht vorhanden.

Eine speziell auf die Gegebenheiten bei MEDAPP zugeschnittene Lösung war notwendig, um die Neutronen- und Photonenkomponente des durch Kernspaltung erzeugten Therapiestrahls berücksichtigen zu können. Hinzu kommt die räumliche Ausdehnung der Strahlungsquelle, die in herkömmlicher Bestrahlungsplanungssoftware nur bedingt berücksichtigt werden kann. Im Rahmen der Entwicklung einer 3D Dosisberechnungssoftware für Neutronentherapie an MEDAPP war es außerdem erforderlich, die von Photonenstrahlung verschiedenen biologischen Eigenschaften der verwendeten Neutronenstrahlung zu berücksichtigen. Das Ziel des im Folgenden behandelten Projekts war es daher, für MEDAPP eine Möglichkeit der individuellen Dosisberechnung unter Berücksichtigung anatomischer Gegebenheiten zu schaffen. Idealerweise sollten hierbei auch biologische Effekte berücksichtigt werden können.

Um diese Ziele zu erreichen, wurden zwei, in der Strahlentherapie bereits etablierte Ansätze für die Berechnung der im Körper absorbierten Dosis, verfolgt. Zunächst wurde die Möglichkeit geschaffen, die Dosisdeposition des Mischfeldes aus Neutronen und Photonen unter Berücksichtigung der MEDAPP-Strahlrohrgeometrie mittels Monte Simulationen zu berechnen. Hierbei wird der Strahlungstransport mit Hilfe des Monte Carlo N-Particle Codes MCNP berechnet. Für die Berücksichtigung biologischer Effekte auf Basis des Repair-Misrepair-Fixation Modells wurde die Monte Carlo Damage Simulation MCDS in die Dosisberechnung mittels MCNP integriert. Als zweite Möglichkeit zur Dosisberechnung wurden Pencil Beam Kernels erzeugt. Zwar wurde diese Methode ursprünglich für die Berechnung der Dosisdeposition von Photonenstrahlung entwickelt, doch lässt sie sich auf Grund prinzipieller Ähnlichkeiten der Photonen- und Neutronendosisdeposition auch auf die Dosisberechnung für Neutronen ausdehnen. Zur Berechnung der Neutronendosis in heterogenen Medien ist hierbei allerdings die Anwendung zusätzlicher Korrekturfaktoren notwendig.

Eine Plausibilitätsüberprüfung im Rahmen eines Vergleichs der mittels Monte Carlo Simulationen berechneten Dosisverteilung mit in Wasser gemessenen Dosisverläufen hat eine zufriedenstellende Übereinstimmung gezeigt. Zwar war ein solcher Vergleich für heterogene Medien nicht möglich, doch konnten die auf Grund von theoretischen Überlegungen erwarteten gewebespezifischen Charakteristika durch die Monte

Carlo Simulationen reproduziert werden. Für die Modellierung der biologischen Effekte war ein Vergleich zwischen Messungen und Simulationen möglich, dessen Aussagekraft zwar begrenzt blieb, der aber dennoch sinnvolle Ergebnisse geliefert hat. Eine zufriedenstellende Reproduktion der mit Monte Carlo berechneten Dosisverläufe konnte auch bei der Berechnung mittels Pencil Beam Kernels erreicht werden.

In der folgenden Arbeit wird dargelegt, dass und in welchem Maße die Dosisberechnung unter Einbeziehung anatomischer Gegebenheiten mittels Monte Carlo Simulationen vielfältige Möglichkeiten in retrospektiven Betrachtungen bietet. Dies bezieht sich zum einen auf die Berechnung der physikalischen Dosis und zum anderen auf die Modellierung der biologischen Wirkung des Mischfeldes im Vergleich zu reiner Photonenstrahlung. Regulatorische Randbedingungen für Medizinprodukte einmal außen vor gelassen, bietet eine Kombination des zwar aufwändigen, aber zuverlässigen Monte Carlo Ansatzes mit dem sehr effizienten Pencil Beam Ansatz im Prinzip auch Möglichkeiten im Rahmen der Realisierung einer Bestrahlungsplanungssoftware für klinische Anwendungen.

I confirm that this dissertation is my own work and I have documented all sources and material used.

Munich, August 8th, 2022   Lucas Sommer

Contents

1 Introduction

One of the world's few remaining facilities for the application of fast neutrons in external radiotherapy is located at the research neutron source Heinz Maier-Leibnitz run by the Technical University of Munich (TUM) located in Garching. Fast neutron therapy (FNT) with fission neutrons has been performed in Garching for over three decades now at two different research reactors; at the old FRM from 1985 till 2000 and at FRM II starting in 2007. Here, the acronym FRM stands for Forschungsreakor München - the German term for research reactor Munich. While FRM II is in operation since 2005, fast neutron therapy is performed at the medical application instrument MEDAPP since the license for medical operation was issued in 2007. In total, 841 patients were treated with neutron radiation in Garching. In the first years, treatments with fast neutrons were performed with both curative and palliative intent. Nowadays, fast neutrons are only applied in special cases of palliative treatment scenarios.

FRM II runs with $20\,\mathrm{MW}$ thermal power and provides neutrons for science, industry and medicine including not only FNT but also radioisotope production for application in nuclear medicine like ^{177}Lu. For external radiotherapy, thermal neutrons from the reactor core are converted to fast neutrons by two plates with a total mass of $540\,\mathrm{g}$ of highly enriched uranium [76]. At the MEDAPP beamline, different filters can be used for modification of the mixed neutron-gamma radiation field. In total, $15\,\mathrm{cm}$ of polyethylene (PE), $16\,\mathrm{cm}$ of lead (Pb), and $1\,\mathrm{cm}$ B_4C in epoxy can be used for beam filtering. Nonetheless, only a filter combination of $1\,\mathrm{cm}$ B_4C in epoxy and $3.5\,\mathrm{cm}$ Pb is in accordance with the license for medical operation and is therefore referred to as medical filter combination.

At MEDAPP, a multi leaf collimator (MLC) is used to shape the treatment fields according to the irradiated volume within the patient. After long time of in house construction and optimization, a new motorized MLC could be installed in 2019. While the dosimetric characterization as well as the neutron and gamma spectra at patient position in the treatment room for the old MLC were investigated before by Kampfer et al. [36], Wagner et al. [77], Breitkreutz et al. [11], Garny et al. [21], and Jungwirth et al. [34], limited information was available on the influence of the new MLC version on the treatment field and dosimetric characteristics. More details on both MLC versions will be addressed in chapter 3.

For the old MLC version, a neutron dose rate of $\dot{D}_n = 0.52\,\mathrm{Gy/min}$ at $2\,\mathrm{cm}$ depth in water was measured together with a gamma dose rate of $\dot{D}_\gamma = 0.20\,\mathrm{Gy/min}$ at identical position for a field size of 9×9 cm^2. The overall distance of the water phantom to the converter plates was about $6\,\mathrm{m}$. The depth of half maximum for the neutron component of the beam was determined to be somewhere at around

5 cm depth in water depending on the field size [77]. The mean neutron energy was determined to be $E_n = 1.9(1)$ MeV [11]. Due to the sharp dose gradient of the neutron depth dose curve and the estimated high RBE, mainly superficial lesions are treated at MEDAPP [64].

While first steps towards a treatment planning system were performed by Garny et al. ([23] & [20]), no ready-to-use computer based three-dimensional treatment planning software was available for treatment planning or evaluation at MEDAPP. From the title of the work presented here, it is probably evident to the reader that the **main goal** of this thesis is to proceed the work begun by others and tackle exactly this lack of computer aided treatment planning and dose calculation by the implementation of 3D dose calculation approaches into an existing treatment planning software. Implemented dose calculation approaches will be discussed and evaluated in chapter 4. *Two main objectives* for the three-dimensional calculation of dose deposited by the mixed neutron-photon radiation field under investigation were identified. First, a *reassessment of treatments* already performed with fast neutrons in the scope of retrospective studies is of highest interest. Second, moving *3D conformal planning* further towards clinical application in order to make state of the art treatment planning also available for radiotherapy with neutrons at MEDAPP is an objective of equal importance. For the verification of performed dose calculations, *dosimetry methods* for mixed fields needed to be revisited and are reassessed as background in chapter 3. In addition to the patient-specific dose calculation presented in chapter 4, modelling of the biological effect of the mixed neutron-photon radiation for MEDAPP will be discussed in chapter 5.

In a recently published retrospective evaluation of fast neutron therapy, Bleddyn Jones identifies three main reasons why - from his point of view - FNT has failed to match its goals in adequately balancing healthy tissue sparing and dose delivery to the tumor [33]. The first reason is that dose calculations in clinical routine did not adequately account for the neutron-hydrogen interactions. Especially taking into account the individual hydrogen content of different tissues is of highest importance for physical dose calculations. The second reason is related to the biological effects of neutron interaction. Here, the biological effect is entangled with the dose deposition from secondary charged particles and varies with different tissue types and also irradiation depth. Jones stated that taking the biological properties of neutrons into account for dose evaluation is therefore crucial. The third reason addresses the observation that severe normal tissue damage can occur after extended time periods after the treatment with fast neutrons which is of course a severe concern; especially in a curative scenario.

Despite these objections, a remaining interest in the application of fast neutrons in special therapeutic scenarios is reflected in recent publications. Retrospective studies on the application of FNT in distinctive treatment scenarios as performed by Aljabab et al. [2] on salivary gland tumours or by Loap and Kirova [40] on breast cancer may help to re-establish a higher level of acceptance for neutrons as a treatment option. Stepping

aside from a retrospective view, the combination of FNT with immunotherapy shows promising first results as reported by Macomber et al. [42] and will probably gain more interest in the future. With Boron Neutron Capture Therapy (BNCT), another application of neutrons in external radiotherapy is re-gaining attention [33]. The promising potential of BNCT as a tumor-selective dose delivery method is reflected in the formation of a BNCT Working Group by the Particle Therapy Co-Operation Group (PTCOG) in 2019 as announced on the PTCOG web page. Calculation studies for the biological effects in BNCT settings also consider a possible combination of BNCT with FNT as discussed by Streitmatter et al. [70]. Regarding conformal dose delivery in FNT, especially people at the University of Washington (UW) in Seattle are putting a lot of effort into making the delivery of neutron dose more conformal to the tumor volume. As discussed by Moffit et al. [46], progress in conformal dose distributions at the UW's Clinical Neutron Therapy System (CNTS) is achieved by using state of the art inverse treatment planning approaches for Intensity Modulated Neutron Therapy (IMNT).

With the presented approach to 3D dose calculation, a re-evaluation of treatments at MEDAPP is enabled. It is now possible to take into account patient-specific anatomy information and to model and investigate the biological parameters of the fission neutron source. This goes along with high potential for the identification of future treatment indications.

2 The Interaction Physics of Neutral Particles and Radiation Transport Calculations

As stated in the introduction, neutron and gamma radiation for irradiation at MEDAPP is generated in fission reactions in the converter plates at MEDAPP. Even though gamma radiation is an unwanted component of the treatment beam, a contamination is of course inevitable. It should be noted at this point that the general term *photon radiation* includes the term *gamma radiation* which names photons produced from nuclear interactions and reactions. Therefore, both terms will be used as synonyms when not explicitly stated differently. In the following chapter, the **interaction principles** of both **neutrons** and **photons** propagating through matter will be summarized. The description of the primary interactions is followed by a closer look on the interaction physics of the generated **secondary particles** and associated **dosimetric concepts**. A description of the practical calculation applying **Monte Carlo methods** for particle transport through matter used in this work is also included. The idea of this part of the thesis is to - of course - include all basic principles necessary for an understanding of the following chapters and - in addition - to cover the characteristics of neutron interaction that give rise to their special place in radiation therapy. These unique characteristics of neutron radiation are treated as examples in the last part of this chapter for the MEDAPP fission neutrons.

At this point, it is instructive to already introduce two concepts. One dealing with neutral particle transport and another one dealing with energy deposition in the transport medium by the particles under consideration. When neutral particles propagate through matter, one way to describe their interaction in the medium is by conceptualizing the interaction as singular events in which they can be scattered from their initial trajectory or be removed. By assuming singular events, the particles are simply described as particles while putting the wave-particle duality aside. Removal happens for example by absorption processes. In the energy range of neutrons and photons in radiotherapy, neutrons interact with the atomic nuclei and photons mainly interact with shell electrons. Thus, secondary charged particles like protons and electrons are generated and propagate further through the medium. These charged particles in turn lead to ionization. For that reason, neutrons and photons are both characterized as *indirectly ionizing radiation*. While neutral particles interact in single events, charged particles undergo constant Coulomb interactions. Exponential

attenuation of the primary fluence of neutrons and photons is observed ([51] & [54]) so that the attenuation of a parallel beam of primary neutral particles can be described by the following equation:

$$N(d) = N_0\, e^{-a\,d} \tag{2.1}$$

where the number of primary particles $N(d)$ at a given depth d in the propagation medium can be calculated from the initial number of particles N_0 and a material- and energy-specific attenuation coefficient a. On a macroscopic level, the attenuation coefficient can be interpreted as the sum of probabilities for all possible interactions within the transport medium. These interactions will be detailed for neutrons and photons in sections 2.1 and 2.2, respectively, both on an atomic or microscopic and on a macroscopic level.

The *imparted energy* ϵ by the interaction processes within a volume of interest is defined for example by the International Commission of Radiation Units and Measurements (ICRU) in Report 26 [28] to be:

$$\epsilon = \Sigma \epsilon_{in} - \Sigma \epsilon_{out} + \Sigma Q \tag{2.2}$$

Here, $\Sigma \epsilon_{in}$ and $\Sigma \epsilon_{out}$ respectively indicate the sum of energies of all primary and secondary particles entering or leaving the considered volume. ΣQ is the net amount of transformed inner energy.

2.1 Neutron Interactions in Matter

For neutrons traveling through matter, the overall interaction probability and the probability for a particular interaction with atomic nuclei to occur is energy-dependent. As stated above, the wave character of neutrons is put aside by the chosen particle picture. This is different for example in diffraction experiments with neutrons where choosing an appropriate wavelength associated to the neutrons' energies is crucial for the investigation of structural parameters of the investigated matter.

When considering neutrons in neutronics or dosimetry, it is common practice to classify them according to their kinetic energy and for some parts of the spectrum also according to the temperature their kinetic energy corresponds to. Mean neutron energy $\bar{E}_n$ and temperature T can be correlated via the Boltzmann constant k_B by $\bar{E}_n = 3/2\, k_B\, T$ so that the mean energy of neutrons in thermal equilibrium with the transport medium can be calculated. Throughout this work, the common *classification of neutrons into thermal, intermediate and fast neutrons* suggested for example by the ICRU [28] or the German Institute for Standardization (DIN e.V.) [19] are adopted. Neutrons with $E_n \leq 0.5\,\text{eV}$ are classified as thermal, with $0.5\,\text{eV} < E_n \leq 10\,\text{keV}$ as intermediate and with $E_n > 10\,\text{keV}$ are classified as fast.

As stated above, the attenuation of a parallel beam of neutrons described by equation 2.1 is due to interactions of the primary neutrons with the atomic nuclei of the propagation medium. Basically, the interaction processes can be separated into

two categories, namely *scattering* and *absorption*. Of course, the same interactions that govern primary neutrons also apply for the transport of secondary neutrons on their particular trajectories. The following discussion of the particular interaction processes partly summarizes their presentation by Rinard [54] and in the ICRU Report 26 [28]. It is also meant to highlight aspects important in the scope of this work. For the notation of interaction processes, the following form is used:

$$T(n, x)R \tag{2.3}$$

Here, T and R respectively indicate the *target* and *resultant* nucleus, n indicates the incident neutron, and x indicates the resultant particle from the interaction. For example, x can be a scattered neutron, a proton, or a gamma quantum.

The scattering of a neutron by a target nucleus happens either *elastically* or *inelastically*. Elastic scattering is noted as an (n, n)-reaction and inelastic scattering is noted as an (n, n')-reaction. While in the inelastic case kinetic energy is partly transferred to the nucleus so that an excited state can be formed, the total kinetic energy remains constant in elastic scattering. Thus, inelastic scattering is only possible when a nucleus can have excited states - which is not the case for hydrogen - and when the incident neutron's energy is high enough so that an excited state can be reached. The de-excitation of the nucleus after inelastic scattering in turn happens via γ-emission.

For materials with a high hydrogen content - like water or soft tissue - elastic scattering plays a crucial role in the description of neutron interaction and dosimetry. For the following discussion of elastic scattering process (cf. [38, p. 53 ff]), the target is approximated to be at rest. Then, the maximum energy transfer from an incident particle - in our case a neutron - to a target at rest can be expressed as:

$$\Delta E_{max} = E_{kin,n} \frac{4A_1 A_2}{(A_1 + A_2)^2} \tag{2.4}$$

where $E_{kin,n}$ is the kinetic energy of the incident neutron, A_1 is the atomic weight of the neutron, i.e. $A_1 = 1$, and A_2 is the mass of the target. The energy transfer is homogeneously distributed between $\Delta E = 0$ and $\Delta E = \Delta E_{max}$ so that the mean energy transfer from the neutron to the target can be expressed as:

$$\overline{\Delta E} = \frac{1}{2}\Delta E_{max} = E_{kin,n} \frac{2A_2}{(1 + A_2)^2} \tag{2.5}$$

Thus, for the elastic scattering of neutrons by hydrogen atoms with $A_2 = 1$ a mean energy transfer of $\overline{\Delta E} = \frac{1}{2}E_{kin,n}$ and a maximum energy transfer of $\Delta E_{max} = E_{kin,n}$ can be calculated. With increasing A_2, the mean and maximum energy transfer from elastic scattering decrease. With equation 2.5, the number n of interactions necessary to moderate the incident neutron's energy from $E_{kin,n}$ down to E_{mod} can be expressed as:

$$n = \frac{log(E_{mod}/E_{kin,n})}{log((A_2^2 + 1)/(A_2 + 1)^2)} \tag{2.6}$$

As an example, the number of elastic scattering events with hydrogen ($A_2 = 1$) and oxygen ($A_2 = 16$) necessary for the moderation of neutrons with $E_{kin,n} = 1.9$ MeV can be calculated for two different energies $E_{mod,1} = 10$ eV and $E_{mod,2} = 0.04$ eV. $E_{mod,2}$ corresponds to a neutron temperature of $T = 37\,°C$. For hydrogen, the respective number of interactions necessary for the moderation down to the two different energies are $m_{1,H} = 18$ and $m_{2,H} = 26$. For oxygen, the corresponding numbers are $m_{1,O} = 104$ and $m_{2,O} = 151$. Water is an important transport medium not only in reactor physics but also in dosimetry since it is recommended to be used as tissue substitute also for neutron dosimetry [19].

Besides scattering, the incoming neutrons can also be absorbed or captured by the target nucleus. Here, the internal structure of the nucleus changes and different pathways of the interaction are possible. Besides the emission of two or more secondary neutrons, there can be charged particle and gamma emission as possible outcomes.

Probably the most important example in the here considered energy range is the neutron capture reaction by hydrogen $H(n, \gamma)D$ where the hydrogen nucleus absorbs one neutron to form deuterium. This process happens by the emission of a γ-particle of energy $E_\gamma = 2.224$ MeV. For hydrogen rich (biological) materials and in the absence of other artificially added absorbers it is the dominant capture reaction. While there is no threshold for the neutron capture by hydrogen, thresholds can in general exist for example for the absorption and subsequent emission of charged particles. Taking again ^{16}O as an example, the thresholds for (n, α)- and (n, p)-reactions to occur in a relevant amount for fast neutrons are between $E_{(n,\alpha)} = 3.5$ MeV to 4 MeV and $E_{(n,p)} = 10.5$ MeV to 11 MeV [14].

The probability for a particular interaction to occur is expressed by the concept of *cross sections* denoted by σ. In a simplified manner, the cross section of an element can be interpreted as the area of an individual nucleus of this element extending into the neutron's trajectory. Therefore, the cross section has the unit of an area $[\sigma] = 10^{-24} cm^2 = 1b$ where b is called *barn*. From the discussion of the different possible interactions it is clear, that the cross section is not simply equal to the geometric cross section but it depends on both the neutron energy and the considered element. The total cross section can be calculated from the cross sections for all scattering and absorption processes by simply summing up the different contributions according to:

$$\sigma_t = \sigma_{sc} + \sigma_{ab} = \Sigma_i\, \sigma_i \tag{2.7}$$

Here, σ_{sc} and σ_{ab}, respectively, indicate the scattering and the absorption cross section and Σ_i indicates the sum over all possible interactions i.

Going back to equation 2.1, the attenuation coefficient a can now be replaced by $a = N\,\Sigma_i\,\sigma_i$. Here, N is the particle or atom density in the propagation medium that can be calculated from the physical density ρ, the molar mass M, and Avogadro's number N_a to be $N = M/(N_a\,\rho)$. By using the definition of the energy-dependent particle *fluence* $\Phi_n = dN/dA$ for N particles traversing a cross sectional area A,
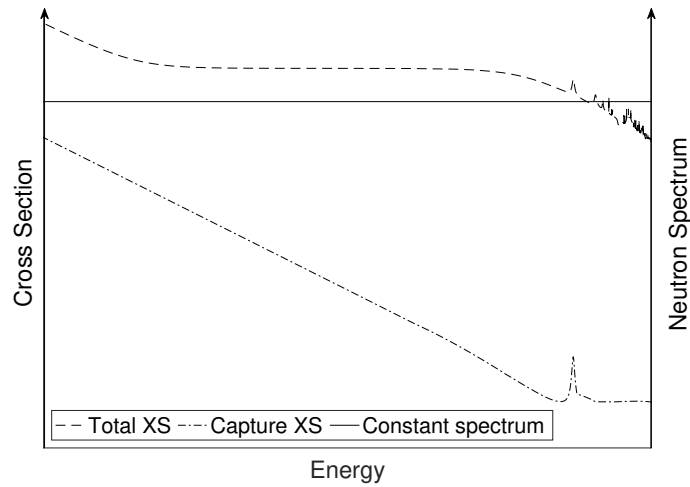
Figure 2.1: Schematic representation of the total and the neutron capture cross section for water in logarithmic scaling. In addition, a constant spectrum is drawn for visualization purposes (see text).

equation 2.1 can therefore be expressed by:

$$\Phi_n(d) = \Phi_{n,0} \, e^{-N \, \Sigma_i \, \sigma_i \, d} \tag{2.8}$$

Of course, this equation only holds true for monoenergetic neutrons propagating through a homogeneous medium. Nonetheless, the energy and material dependence can be included. By approximating the compound-material as a mixture of atoms without molecular binding effects, the overall cross section σ_m for material m can be calculated from:

$$\sigma_m = \Sigma_j \, p_j \, \sigma_j \tag{2.9}$$

where p_j indicates the weight-percentage per gram of the individual elements j in the compound. For an energy-dependent fluence $\Phi_n(E)$, the mean cross section $\bar{\sigma}_\Phi$ can then simply be calculated from the mean of $\sigma(E)_m$ over the spectral neutron distribution as follows:

$$\bar{\sigma}_\Phi = \frac{\int_0^{E_{max}} dE \, \sigma(E)_m \, \Phi_n(E)}{\int_0^{E_{max}} dE \, \Phi_n(E)} \tag{2.10}$$

Since the cross section is energy-dependent, it is clear that the spectral distribution and also the mean neutron energy of the primary neutron beam will change with depth in the propagation medium. From equation 2.10, only the mean cross section for the primary incident neutron spectrum can be calculated. In addition, scatter effects and thus a depth-dependent contribution of moderated neutrons will change the spectral distribution as well. This holds also true for the *energy flux* which - for monoenergetic neutrons - is defined as $\Psi = \Phi \, E$. In figure 2.1, the energy-dependence of the total cross section σ_t for water is shown schematically on a logarithmic scaling

for materials like water and soft tissue. While the elastic scattering cross section component is rather constant for neutron energies $E_n < 10 - 100 \, \text{keV}$ and above $0.1 \, \text{eV}$, a $1/v$ dependence on the neutron velocity v is shown for the neutron capture cross section. Furthermore, resonances are drawn which are material specific and in general occur when the neutron energy is close to the energy for an excited state of the nucleus. To visualize the depth-dependence of the neutron spectrum, an imaginary spectral distribution with a homogeneous distribution of primary neutrons over all energies is shown. It can be seen immediately that the probability for an interaction increases with decreasing energy so that the lower energy part of the spectrum will be attenuated to a higher degree.

On a macroscopic scale, the cross section for a given material is defined as:

$$\Sigma_t = N \, \bar{\sigma}_m \tag{2.11}$$

where Σ_t is called the total macroscopic cross section. The correlation between the macroscopic cross section and the mean free path - i.e. the mean path length a particle travels before an interaction - is given by the definition of the mean free path (cf. [52, p. 283]):

$$\bar{x} = \frac{\int x e^{-\Sigma_t x}}{\int e^{-\Sigma_t x}} = \frac{1}{\Sigma_t} \tag{2.12}$$

2.2 Photon Interactions in Matter

For photon or gamma radiation, the general interaction principles and the propagation of the primary beam component can be described in a similar way to neutrons. While above introduced for neutrons, the concepts *fluence* and *energy flux* are defined for photon radiation as well. At this point it is important to keep in mind that the gamma spectrum will not only be depth-dependent due to interaction processes of the primary beam but also due to a secondary gamma component from neutron interactions; for example from neutron capture reactions.

Equation 2.1 can also be used to describe the propagation of primary photons. By replacing *a* by the *linear attenuation coefficient* μ for photons, the depth-dependent fluence of primary photons can be expressed as:

$$\Phi_\gamma(d) = \Phi_{\gamma,0} \, e^{-\mu d} \tag{2.13}$$

The linear attenuation coefficient is again energy and material-dependent. From the definition of the mean free path in equation 2.12 - which also applies for gamma radiation - the connection of μ to the interaction probability is clear. The gamma radiation in the considered energy range below $10 \, \text{MeV}$ mainly interacts with the electron shell via *Compton* or *Thomson scattering* or via the *photoelectric effect*. But interaction can also happen in the Coulomb field of the atomic nuclei in *pair production* processes or - in exceptional cases - also with the atomic nuclei via *photonuclear*

interaction. Interaction without ionization can also happen with the whole atom via *Rayleigh scattering*. In the following, the aspects of the different interaction mechanisms are summarized only to a limited extend from their discussion presented by Podgoršak [52]. A very detailed discussion is given there. The focus is on the production of secondary charged particles that in turn contribute to ionization and therefore to the (locally) imparted energy.

In terms of energy deposition in a confined volume, *Rayleigh scattering* is of minor importance. The reason for that is twofold. First, the interaction of the photon happens with the whole atom and only a small amount of recoil energy is transferred to the atom. Also, the scattering angle is small for materials with low atomic number Z. Second, no ionization happens within the material so that no directly ionizing electrons are generated. Therefore, the imparted energy in equation 2.2 will be essentially zero in this process.

For the gamma energy present at MEDAPP, *photonuclear interactions* (γ, n) only play a minor role. This is due to the high energy threshold of $E_{thr} = 8\,\text{MeV}$.

In the Coulomb field of atomic nuclei, *pair production* of a secondary electron-positron pair can occur when the incident photon energy exceeds two times the rest mass of an electron. A similar effect - triplet production - can occur in the Coulomb field of an electron so that two free electrons and one free positron are generated with a threshold energy equivalent to four times the electron rest mass. While for the production of the electron-positron pair the mean energy transfer to the two particles can be calculated via $\bar{E}_{tr} = 1/2(h\nu - 2m_ec^2)$, essentially all distributions of the available energy between the electron and the positron are possible. Here, $h\nu$ denotes the incident photon's energy calculated from Planck's constant, h, and the frequency of the incident gamma, ν. For triplet production, the factor $1/2$ in the equation for the mean energy transfer is simply replaced by $1/3$. Energy deposition in dosimetric measures is then driven by the secondary charged particles, electrons and positrons. With increasing gamma energy, the trajectories of the generated particles are mainly oriented in forward direction.

Regarding the interaction with electrons, the electrons of the atomic shell are categorized into two groups, loosely bound or approximately free on the one hand and bound on the other. Electrons are categorized as approximately free when the energy of the incident photon is much larger than the electrons' binding energy. While photon interaction with an approximately free or loosely bound electron is referred to as *Compton scattering*, the *photoelectric effect* describes the total absorption of the photon in the interaction with a bound electron. For both types of interaction, one electron is released in the ionization process from the material and can in turn lead to secondary ionization. The Compton scattering is also referred to as *incoherent scattering* due to the fact that a photon with a shifted wavelength in reference to the incident photon is released in the process.

Like for neutron interactions, the total linear attenuation coefficient for photon interaction can be described as the sum of the individual linear attenuation coefficients.

While a detailed description of the energy and material dependence of the individual attenuation coefficients for the interaction processed discussed above was omitted in this section, it should be noted again that *photoelectric effect* and *Compton scattering* are the dominant interaction processes within the gamma energy range present at MEDAPP. As exemplified for water by Buzug [12], the interaction is dominated by the photoelectric effect up to gamma energies of about $E_\gamma \approx 30\,\text{keV}$. Above, Compton scattering dominates up to energies of $E_\gamma \approx 30\,\text{MeV}$. Above 1022 keV, the contribution of pair production increases but only starts to dominate the interaction above the maximum gamma energy at MEDAPP.

2.3 Dosimetric Concepts

According to ICRU Report 26 [28], *dose* is defined as mean energy imparted $\bar{\epsilon}$ per unit mass. This purely physical quantity carries the SI-unit *Gray (Gy)* and it will also be referred to as *physical dose* in the following. One Gray is defined to be $1\,\text{Gy} = 1\,\text{J}/1\,\text{kg}$. While the deposited energy can - in principle - be compared for all types of radiation, the biological effect highly depends on the type of radiation and whether the primary and secondary particle tracks show sparse or dense ionization characteristics [28]. Different models that account for the biological effects of different types of radiation are compared by Stewart et al. [67]. Usually, these models are based on the idea to relate the physical dose of a considered radiation to the physical dose of photons as a reference. In the following, dosimetric concepts for neutral and charged particles will be discussed. Modelling of the biological effects of fission neutrons will be discussed in the next chapter.

The dose is defined according to the following equation:

$$D = \frac{d\bar{\epsilon}}{dm} \tag{2.14}$$

Here, *dm* refers to the mass of the volume in which the deposition of energy according to equation 2.2 happens. From this equation it is evident that the balance between energy of particles entering and leaving the volume of interest depends on the energy transfer of primary particles, the range of secondary particles, and therefore the size of the volume. While the possible interactions of primary neutrons and photons were discussed above, measures for energy transfer of primaries and the interaction of secondaries will be summarized briefly. More profound discussions are provided in ICRU Report 26 and by Podgoršak [51].

For dosimetry of neutral particles as indirectly ionizing radiation, the *kinetic energy transferred per unit mass (KERMA)* is used as a measure for the energy transferred to directly ionizing radiation within a volume of interest. KERMA also carries the unit *Gray*. Even though of minor importance in the energy range present at MEDAPP, it should be noted that inelastic scattering for neutrons is conceptually not included in this definition. Also, capture reactions are only implicitly included when considering

the resulting secondary gammas as part of the mixed neutron-gamma field. In the special case of negligible secondary particle ranges, KERMA equals the difference of $\Sigma\epsilon_{in}$ and $\Sigma\epsilon_{out}$ in equation 2.2. With appropriate energy-dependent KERMA-factors $f_K(E)$ as tabulated for neutrons in ICRU Report 63 [31], KERMA can be calculated for a specific material from a given fluence $\Phi(E)$ by use of the following equation:

$$K = \frac{d\bar{E}_{tr}}{dm} = \int \Phi(E)f_K(E)dE \qquad (2.15)$$

For material compounds, KERMA-factors can be calculated by weighting the different element specific factors by the weight-percentage within the material (cf. [31]).

In general, the range of secondary charged particles is non-negligible so that these particles also contribute to the energy transport to and out of the considered volume. Therefore, a discrepancy between physical dose and KERMA occurs and they only coincide when *secondary charged particle equilibrium (CPE)* is present. Especially for photon energies in the MeV-range used in radiotherapy, the range of secondary electrons is large so that a build-up effect of CPE close to the surface of an irradiated object will occur. Whether or not this will happen depends on the types and spectra of secondary charged particles as well as on the transport medium.

For charged particles propagating through matter, the quantity *linear stopping power S* is defined in order to describe the expectation value of the particles' energy loss dE per unit path length dx. The process is dominated by Coulomb interaction with the electron shell in turn leading to ionization of the propagation medium. Furthermore, Coulomb interactions with the atomic nuclei and associated radiation losses via Bremsstrahlung are possible. Therefore, the stopping power can be expressed as the sum of collision and radiation stopping power, S_{col} and S_{rad}, according to:

$$S = -\frac{dE}{dx} = S_{col} + S_{rad} \qquad (2.16)$$

For heavy charged particles - i.e. particles with a rest mass larger than electrons, basically only collision stopping power has to be considered while for electrons and positrons also radiative energy loss needs to be taken into account. The mean range R_{CSDA} of charged particles in matter can be approximated from the stopping power by the *continuous slowing down approximation (CSDA)* [39, p. 121] via:

$$R_{CSDA} = \int_0^{E_{kin,0}} -S^{-1}dE_{kin} \qquad (2.17)$$

Here, the integration over the kinetic energy goes from zero to the initial kinetic energy of the particle. While the CSDA range gives the mean path length that a charged particle travels in matter, the projected range onto its original trajectory is even shorter. The stopping powers of electrons, protons, and alpha particles are tabulated for different materials by the National Institute of Standards and Technology (NIST) [7].

As discussed in section 2.1, the most important interaction process in terms of energy deposition for fast neutrons with a mean energy of 1.9 MeV and a maximum energy below 10 MeV are (n, p)-reactions. In order to estimate the maximum and mean range secondary ions from elastic scattering with neutrons will travel, proton spectra from (n, p)-reactions and proton stopping power can be used. The importance of protons can be seen from equations 2.4 and 2.5. These equations depend on the target nucleus' atomic mass and are maximized for hydrogen atoms. From the general formula for the stopping power of non-relativistic heavy ions, a proportionality to the inverse of the projectiles kinetic energy E_{kin}^{-1}, the square of its charge z_p^2, and its mass m_p is given [39]. All three factors are minimized for protons so that the stopping power for heavier particles from elastic scattering with neutrons will also be larger. Therefore, the CSDA range will decrease. From the formula for the stopping power, the well known *Bragg curve* with its characteristic *Bragg peak* can be calculated [39].

Another concept associated with stopping power but modified to take into account local effects is the *linear energy transfer (LET)*. The LET is defined as:

$$L_\Delta = S_{col} - \Sigma_i E_{kin,i} \tag{2.18}$$

where the sum goes over all particles i with a kinetic energy $E_{kin,i} > \Delta$. The cutoff energy Δ is defined individually in such a way that secondary particles - like for example δ-electrons from electron interactions - with energies high enough to escape the volume of interest are not considered in local energy deposition. In accordance with the literature, neutron radiation will also be addressed as high-LET and gamma radiation as low-LET radiation even though by the definition above actually the secondary charged particles are the radiation that is associated to high and low LET values.

2.4 Biological Effect of Fast Neutrons

In order to describe and compare the biological effect of different irradiation scenarios, a well established approach is the linear-quadratic (LQ) model. See for example [74] for a short summary. In the LQ-model, the survival fraction *SF* of irradiated cells in dependence of the dose *D* is described by:

$$SF(D) = exp(-\alpha D - \beta D^2) \tag{2.19}$$

On a logarithmic scale, the α- and β-value in the exponent, respectively, describe the linear and quadratic effect of the radiation dose. As an example, figure 2.2 shows the survival fraction for different α/β-values in a schematic way. Tissue with a dominant linear term expressed by a high α/β-value like $\alpha/\beta = 10$ Gy are referred to as early reacting tissue. Late reacting tissue is characterized by lower α/β-values like $\alpha/\beta = 3.5$ Gy.

For the comparison of different types of radiation - like for example high- and low-LET radiation - the *relative biological effectiveness (RBE)* is defined as the dose ratio
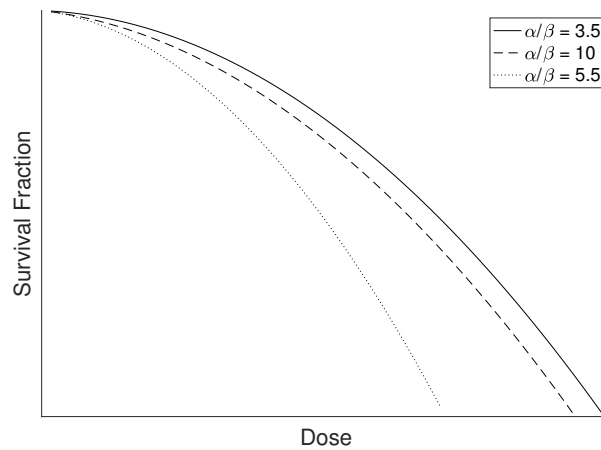
Figure 2.2: Schematic plot of survival curves for different α/β values as calculated from the LQ-model with ordinate in logarithmic scale.

of different types of radiation that need to be applied to achieve the same biological endpoint. Using ^{60}Co γ-radiation as a reference for an isoeffective cell survival SF_{iso}, the *RBE* for example for neutron radiation can be defined according to:

$$RBE := \frac{D_\gamma|_{SF_{iso}}}{D_n|_{SF_{iso}}} \tag{2.20}$$

It is often assumed - for example in [37] and [17] - that high-LET radiation mainly influences the α-value in cell survival curves while leaving the β-value unaltered. The plots of the solid and dashed lines in figure 2.2 were generated by increasing the α-value by a factor of approximately three while keeping the β-value constant. In contrast to the assumption of a LET-independent β-value, Jones discussed an increase in β-values in a retrospective evaluation of irradiation with fast neutrons [32]. There, an increase of $\beta_n = 1.82\beta_R$ in comparison to 4 MeV x-ray radiation as reference is reported. The effect on cell survival is evident from the dashed and dotted curves in figure 2.2, where now the α-value is kept constant while increasing the β-value by a factor of 1.82.

In order to incorporate tissue and radiation-type dependencies as well as the dose-dependence of the RBE, different models like the local effect model, the microdosimetric-kinetic model or the repair-misrepair-fixation model were developed and are review by Stewart et al. [67]. As stated there, all three models are based on the assumption that the LQ-model adequately describes experimental data and the dose-dependent $RBE(D)$ for a given dose or fraction D with respect to a reference radiation can be expressed by:

$$RBE(D) = \frac{(\alpha/\beta)_R}{2D}\left\{-1 + \sqrt{1 + \frac{4D}{(\alpha/\beta)_R}(1 + \frac{D}{(\alpha/\beta)_R}\frac{RBE_{HD}^2}{RBE_{LD}})RBE_{LD}}\right\} \tag{2.21}$$

In this equation, RBE_{LD} and RBE_{HD}, respectively, are the ratios of the α-values and

the square root of the β-values for the investigated and the reference radiation. For neutrons, they can be calculated via $RBE_{LD} = \alpha_n / \alpha_R$ and $RBE_{HD} = \sqrt{\beta_n / \beta_R}$.

2.5 Radiation Transport Calculation

For applications in medical physics like for example dose calculations in FNT or calculations of particle spectra of irradiation facilities at specific points in the treatment room, simple calculations of the primary fluence according to equations 2.1 or 2.13 are usually not accurate enough. In those cases of complex geometries with varying densities and elemental compositions of the transport medium, both the primary and the scattered component of the beam need to be included.

While in principle two approaches - one *analytical* and one *stochastic* - exist to incorporate effects of complex geometries, only the stochastic approach to radiation transport calculations will be used and therefore discussed in more detail in the following. The *analytical approach* is based on solving the deterministic Boltzmann transport equation and is reviewed for dose calculations in radiation therapy by Bedford [6]. The *stochastic approach* is based on the simulation of individual primary and secondary particle tracks by the application of *Monte Carlo (MC)* methods. Assuming an accurate description of the stochastic processes that govern individual particle interactions, the average behaviour of primary and secondary particles can be deduced by applying the central limit theorem for the considered scenario by simulating an adequate number of particle tracks [81, p. 1-2]. In practice, random numbers are used in order to model the stochastic nature of the considered processes.

For the purposes pursued in this work, the Monte Carlo N-Particle code MCNP version 6.2 [78] is used to simulate primary neutrons and gammas and their secondary particles. MCNP was originally developed for neutron and photon transport calculations in the low to higher energy regime up to 20 MeV [27]. Therefore, it is well suited for the application in the context of the MEDAPP fission source. MCNP version 6 also provides the capability to simulate the generation and propagation of charged particles [24]. Furthermore, existing models of the MEDAPP beamline could be used from [5] and [9]. In addition, MCNP is also applied by the FNT group at the University of Washington Clinical Neutron Therapy System for spectral and dosimetric characterization [45] so that an exchange on methodologies for neutron transport calculations is facilitated to a considerable degree.

As discussed in section 2.3, the calculation of deposited dose requires an accurate knowledge of the energy-dependent particle fluence in the considered medium. For treatment planning purposes, the patient geometry is discretized by using volume elements from imaging data - commonly referred to as *voxels*. For every voxel, a specific material can be defined and the particle fluence of uncollided and scattered primary particles and their secondaries within that voxel can be calculated using MCNP. MCNP offers the ability to transport neutral and charged particles depending on the considered problem and user selected options. Again, the difference in the

interaction of neutral particles in singular events with free flight in-between and charged particles undergoing constant interaction is reflected in how the processes are modelled [81].

For neutral particles in the energy range present at MEDAPP, tabulated interaction probabilities and cross sections are loaded by MCNP from the *evaluated nuclear data files (ENDF)* [24]. ENDF database version ENDF/B-VII.1 [14] evaluated at 293.6 K comprises tabulated data for all materials considered in this work so that the sampling of individual interactions - as described in sections 2.1 and 2.2 - and the production of secondary particles can be modelled. Only for hydrogen the older ENDF/B-VI.6:X was used since it extends to maximum neutron energies of 150 MeV. The final choice of the library for each chemical element was guided by the library's upper energy limit. Choosing libraries with the highest energy limits available should facilitate intercomparison with neutron spectra of higher mean energy. For neutrons with energies below 4 eV, cross section data for selected materials like water and polyethylene exist in order to account for solid- and liquid-state transport properties becoming important in the low energy range [27]. The default minimum cutoff energies for neutrons and photons are 0 eV and 1 keV, respectively, which can be adjusted to higher energy values.

While significant differences exist in the exact way charged particle transport is modelled for electrons and positrons on the one hand [81, 2-67 ff.] and ions on the other hand [82], the sampling of energy loss in the transport medium in both cases is mainly based on the continuous slowing down approximation using the collisional stopping power as discussed in section 2.3. The stochastic nature of the interactions is accounted for by sampling of energy straggling [24]. If secondary particle production cross section data exists for the considered energy range these cross sections are also sampled. Tabulated data can be favoured by using MCNP's mix and match option [79]. Multiple (small) scattering events are modelled stochastically as condensed histories but large scattering angle sampling is also enabled as they occur for example for nuclear scattering of heavy charged particles. Furthermore, delta-ray production from ion interactions is possible [78]. For electrons and positrons, Bremsstrahlung events or radiative energy losses can also be included. In cases, where only photons but no electrons are transported, the thick-target Bremsstrahlung model is used. In this model, electrons are generated but assumed to locally slow down to rest so that Bremsstrahlung is generated [81, p. 2-57]. Minimum cutoff energies in MCNP are 10 eV for electrons and 1 keV for ions.

One important option to control the particle population is MCNP's ability to sample specific interactions not analog to the actual physics but in an implicit way. For example, implicit neutron capture differs from the actual (analog) physics in a way that the neutron is not captured and therefore stopped by the corresponding probability upon an interaction event. The neutron rather is biased to survive but its contribution to the simulation result is reduced so that the capture event is accounted for in an implicit way.

MCNP offers a variety of *detectors* or *tallies* in order to provide the user with options to record problem specific quantities [79, p. 1-385 ff.]. For every voxel or in general for every confined volume element, particle fluence of all simulated particles can be estimated from the track lengths of the considered particles within the volume by an MCNP tally called *F4-tally*. Fluence-dependent quantities like KERMA or heating of individual particle species within the volume can be recorded by modified fluence tallies. For these so-called *F6-tallies*, energy-dependent multiplier like KERMA-factors are used. In case tabulated *average heating numbers* exist as estimates of deposited energy per track length, they are used to tally energy deposition by taking into account the interaction probabilities of individual processes. When no tabulated data is available, the collisional stopping power and nuclear recoil energies are tallied. These modified fluence tallies simply record the energy transfer of specified particles within a volume without offering the possibility to take into account energy of secondary particles leaving the volume. An adequate tallying of the net amount of deposited energy or dose as described by equation 2.2 is provided by MCNP with the *+F6-tallies* but with the restriction that no particle specific information can be recorded. Non-tracked secondary particles or particles falling below the energy-cutoff are assumed to deposit their energy locally. This - again - highlights the importance of an adequate energy cutoff that can be estimated from the mean free path.

2.6 Examples of Neutron Cross Sections and Dose Deposition

From measurements and Monte Carlo simulations by Breitkreutz et al. [11] and Garny et al. [21], the maximum neutron energy at MEDAPP was estimated to be below 12 MeV. For the simulated examples shown below, the maximum neutron energy was 10 MeV. This upper energy limit is especially important for the *examples of microscopic and macroscopic cross sections* presented in the following subsection 2.6.1. The cross sections given there are used for transport calculations using MCNP. In subsection 2.6.2, the *simulated dose deposition of the neutron component* and the generated secondary particles for a square field of size 6×6 cm^2 is given as another example.

2.6.1 Examples: Microscopic and Macroscopic Neutron Cross Sections

Figures 2.3 and 2.4, respectively, show the energy-dependent *microscopic cross sections* for neutron interactions in *soft tissue* as the most important medium for dose-to-tissue calculations and *water* as the recommended dosimetry medium for mixed neutron-gamma fields [19]. Microscopic cross sections for selected interactions are plotted as they were calculated by MCNP from tabulated ENDF data for the respective medium with elemental and isotopic composition as input. The color of the curves either

indicates the interaction type - like total or elastic cross section - or refers to the secondary particles produced in the neutron interaction. In cases where different reaction types lead to the production of the same secondary particle, broken lines are used to indicate different interactions.
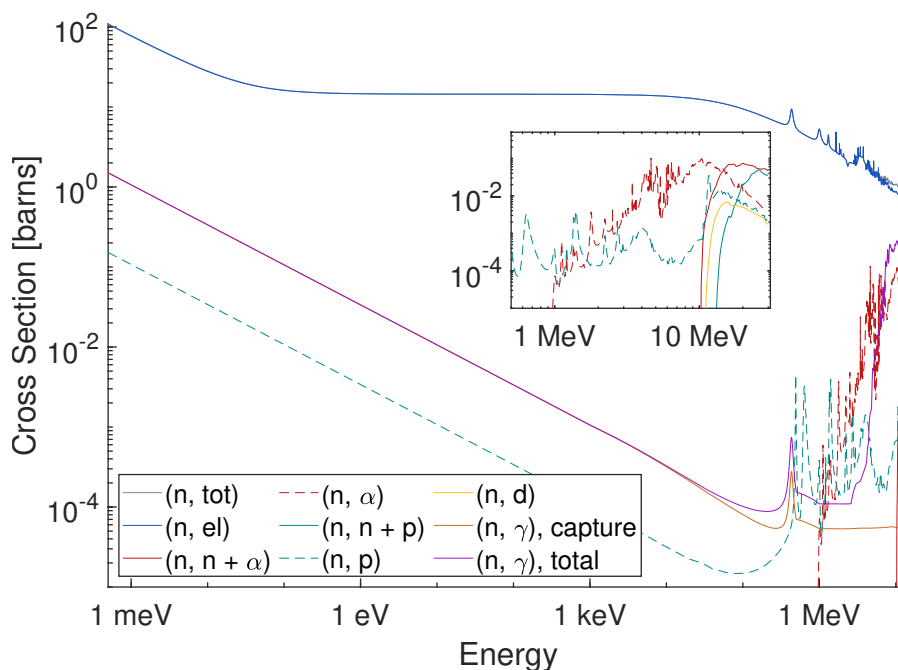

Figure 2.3: Selection of microscopic cross sections of **soft tissue** as calculated by MCNP from tabulated ENDF data.

It can be seen from figure 2.3 that the total neutron cross section (gray) for soft tissue is dominated by the cross section for elastic scattering (blue) between the incident neutrons and the nuclei of the transport medium. As discussed in section 2.1, the energy dependence of the microscopic cross section is clearly visible. Below 100 keV, the γ-production cross section (purple) is dominated by radiative neutron capture reactions (light brown). As indicated by the broken turquois line, secondary proton production from nuclear interactions - mainly from neutron-nitrogen-interactions by $N(n, p)C$-reactions - is also present for all energy ranges in soft tissue due to the soft tissue's nitrogen component. Thresholds for a significant contribution of charged particle production cross sections other than from elastic recoil and protons from $N(n, p)C$ can be seen in the small subplot to start at about 1 MeV. While these cross sections are about one to three orders of magnitude below the elastic cross section, they, nevertheless, highlight the importance to include secondary charged particles in the MC simulations - especially for the consideration of biological properties. From an inspection of the subplot in figure 2.3, α-particles and protons can be identified as the most important secondary charged particles in the considered energy range below 12 MeV besides recoil nuclei from elastic scattering. As an unfortunate matter of fact, protons from nuclear interactions and in part also α-particles for neutron energies

between 1 MeV to 5 MeV could not be included in the Monte Carlo simulations. Therefore, protons associated to the cross section indicated in turquois and in part the contributions from α-particles are missing in all of the following dose calculations.
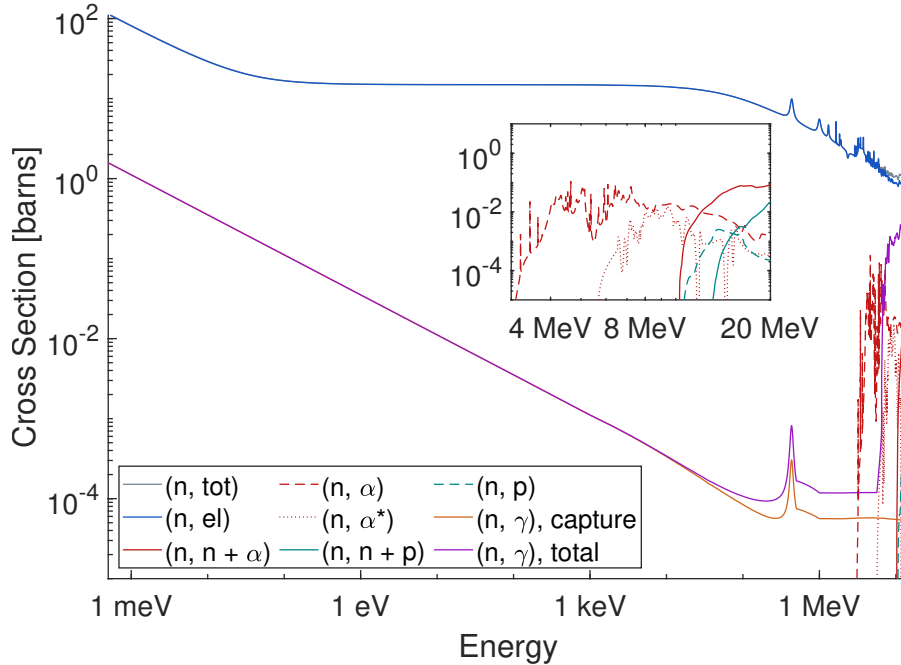
Figure 2.4: Selection of microscopic cross sections of **(light) water** as calculated by MCNP from tabulated ENDF data. The ∗ in the (n, α^*)-reaction indicates the residual nucleus to be in an excited state.

Figure 2.4 shows the microscopic cross section of water, again calculated by MCNP. Water is used as tissue substitute for neutron dosimetry due to its physical density and hydrogen content comparable to soft tissue. Again, the elastic cross section (blue) gives the largest contribution to the total cross section (gray) for neutron interactions. While the threshold for a significant contribution of secondary charged particle production other than elastic scattering is lower due to the different elemental composition, the general characteristics of the microscopic cross sections are comparable to the characteristics for soft tissue.

Besides the microscopic cross section data for interaction probabilities shown so far, it is also instructive to consider the *total macroscopic cross sections* of different materials and their influence on neutron propagation and on the mean free path length in the respective medium. As discussed in section 2.1, the material's density is included in the calculation of the macroscopic cross sections. For soft tissue, bone, lung tissue, and water, the total macroscopic cross sections are indicated as solid lines in figure 2.5. In addition, the contribution of the elastic scattering cross sections are indicated for the different materials by broken lines. While the macroscopic cross sections for soft tissue (green) and water (blue) only differ by a small amount, the influence of the physical density becomes evident from a comparison of soft and lung tissue cross sections. For
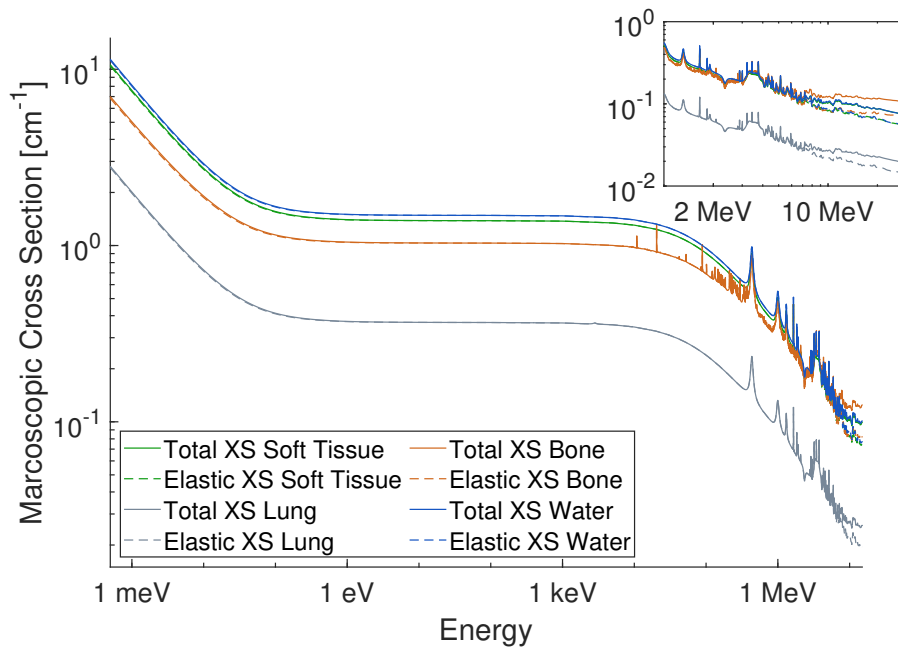
Figure 2.5: Comparison of **total** and **elastic macroscopic cross sections** of bone, lung, soft tissue, and water. While the color coding indicates the different materials, the solid lines show the total cross section and the broken lines the elastic one.

soft tissue and lung (gray), the elemental composition is not very different but the density differs by a factor of four. Approximately, this ratio can also be found in the plateau region of the cross sections between about 1 eV and 20 keV. For bone (light brown), not only the density differs from soft tissue but also the hydrogen content is much lower which results in a reduced total macroscopic cross section compared to soft tissue. The general trend of a dominance of the elastic cross section for neutron energies below about 7 MeV holds true for all shown materials. The solid and broken lines in figure 2.5 nearly coincide.

For the neutron spectrum present at MEDAPP, the average mean free path R_{mfp} of primary neutrons for soft tissue (st), lung (l), bone (b), and water (w) can be calculated to be: $R_{mfp,st} = 4.10\,\text{cm}$, $R_{mfp,l} = 15.64\,\text{cm}$, $R_{mfp,b} = 4.24\,\text{cm}$, and $R_{mfp,w} = 3.90\,\text{cm}$. Here, the average mean free path is simply the inverse of the average total macroscopic cross section.

2.6.2 Example: Dose Deposition from Neutron Radiation

In the above examples of microscopic cross sections, the difference in production probabilities for secondary charged particles as well as for secondary gammas and their production interactions are included. As another example, the *total dose deposition* and the contribution to the total dose from the energy deposition or heating of secondary particle species can be shown. In figure 2.6a, the total depth dose and the

depth-dependent heating from charged particles are shown for the neutron component of the treatment beam propagating though water simulated with MCNP. The cross section for water as shown above was used. The curves were calculated for a square field of size $6 \times 6 \ \mathrm{cm}^2$ and are normalized to the value of the total dose in $5 \ \mathrm{cm}$ depth. In order to record the depth dose curve, MCNP tallies to record the total dose and the individual particle species' heating curves were positioned along the central beam axis with their radius vector perpendicular to the beam direction. The tallies are shaped cylindrically with a diameter of $1.5 \ \mathrm{cm}$ and a heights of $2 \ \mathrm{mm}$. As reference, the black curve in figure 2.6a shows the total dose tallied within each detector cell along the beam axis by +F6-tallies with the correct summation and subtraction of the deposited energy. A build-up region for the total dose (black) and secondary proton heating (green) can be identified in figure 2.6a with a maximum in about $3 \ \mathrm{mm}$ depth. As expected for neutron heating (red), only a slight build-up region which is more a plateau region up to again $3 \ \mathrm{mm}$ depth in water can be seen. While for the direct contribution of neutrons an exponential decrease of the deposited energy is expected, the plateau region reflects the scatter contribution to the heating curve. A depth-dependent contribution of gamma heating mainly from neutron capture reactions can be seen from the yellow curve. The fact that the gamma and electron heating curves nearly coincide, indicates lateral charged particle equilibrium for electrons within the tally region.
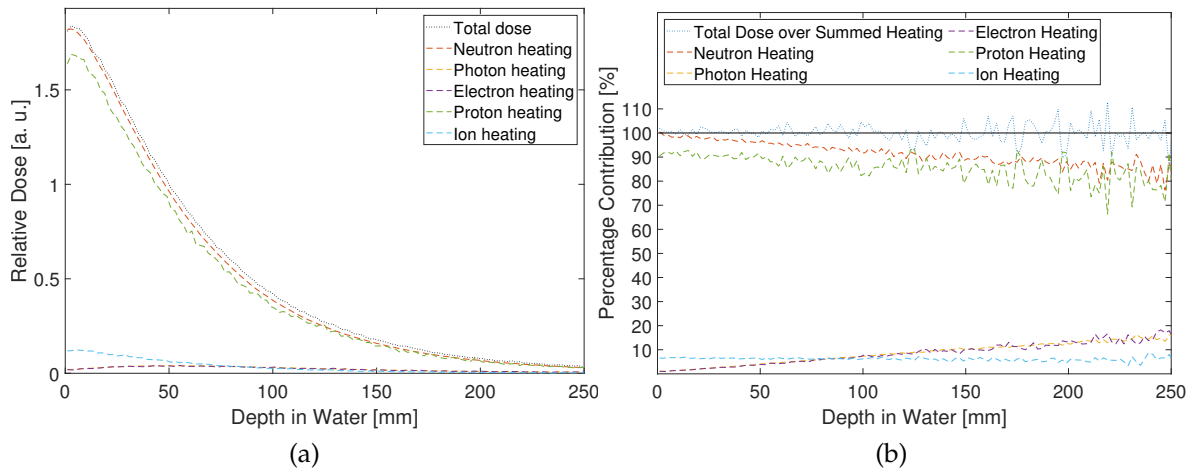
Figure 2.6: (a) Depth dose curve for neutron component of an irradiation field with size $6 \times 6 \ \mathrm{cm}^2$ calculated using MCNP. (b) Depth-dependent **percentage contribution** to the dose deposition in water of primary neutrons and secondary particles calculated by MCNP for the same irradiation field.

In figure 2.6b the percentage contribution of the different heating tallies as well as the ratio of total dose over the summed charged particle heating (blue dotted line) is shown for the depth-dependent data visualized in figure 2.6a. The blue dotted line indicates the agreement of the total dose on the one hand and the sum

of charged particle heating on the other hand as another method to calculate the dose deposition of secondary ionizing radiation. As discussed in section 2.3, this approximation is highly dependent on the secondary particle ranges and the presence of charged particle equilibrium. For the first 10 cm, figure 2.6b shows an agreement within 5 % and within 10 % up to a depth of 20 cm. The percentage of neutron heating contributing to the total dose decreases with increasing depth by the same amount as the contribution of secondary gamma heating increases. This decrease/increase is approximately linear with increasing depth. While for all depths the proton contribution is dominant, it is even larger than or equal to 90 % within the first 5 cm. The heating contribution of ions other than protons is approximately constant within $5 - 7$ %.

Of course, the characteristics discussed in this example are field-size-dependent so that for example the contribution of secondary gammas increases for larger fields due to an increasing number of neutrons being captured in the lateral region of the beam. Nonetheless, the depth of the secondary gamma dose deposition maximum is field-size-independent and is located at about $5 - 7$ *cm* depth in water. This maximum position is due to prompt gamma dose deposition primarily from neutron capture reactions associated to the thermalization of neutrons.

3 Background and Methods for Dosimetry and Treatment Delivery at FRM II

The following chapter provides a short summary of the *dosimetry method* using ionization chambers applied at MEDAPP. By this method, the neutron and the gamma component of the deposited dose in water can be measured separately. A discussion of the *calibration procedures* for the ionization chambers used at MEDAPP is also added. Furthermore, the components of the beamline important for beam application and *beam shaping* at MEDAPP are discussed briefly.

3.1 Two Chamber Dosimetry Method for Mixed Neutron-Gamma Fields

Dosimetry methods to infer the energy deposited in tissue substitutes using ionization chambers are well established in external radiation therapy including fast neutron therapy. In general, guidelines are provided by the International Commission of Radiation Units and Measurements, the American Association for Physicists in Medicine (AAPM), or the German Institute for Standardization. The following discussion of fast neutron dosimetry is based on guidelines formulated in ICRU reports 26 [28] and 45 [29], AAPM report 7 [1], and in DIN 6802-6 [19]. In this context, a unique characteristic is the importance to accurately determine the inevitable contribution from gamma radiation with biological properties different from neutron radiation.

3.1.1 The Two Chamber Method for Separation of Neutron and Gamma Dose

As already discussed by Gray in 1936 [25], the amount of charge produced from ionization in a small gas cavity brought into - for example - a tissue substitute medium can be used to calculate the energy deposited in the medium. One way to realize a detector based on this principle are ionization chambers (IC). ICs are made of a wall electrode surrounding a gas cavity in combination with a central electrode. The dose D to the gas cavity can be calculated from the collected charge Q (as reading R of the IC) and the mean energy $\bar{W}$ needed for an ionization event in the chamber.

This relationship is given in the following equation:

$$D_{gas} = \frac{Q}{m}\frac{\bar{W}}{e} \tag{3.1}$$

Here, *m* and *e*, respectively, are the mass of the gas in the cavity and the elementary charge. $\bar{W}$ depends on the used gas and on the type and energy of the produced secondary charged particles. As discussed in chapter 2, secondaries produced in the mixed neutron-gamma radiation field are mainly electrons from gamma radiation and ions from neutron interactions. The basic requirement for the construction of ionization chambers is that the presence of the cavity does not change or disturb neither the primary neutron and photon fluence nor the secondary charged particle fluence (cf. [28, p. 22] & [29, p. 23]). In reality, these requirements will never be fulfilled. However, two limiting conditions for an approximate fulfillment exist. Either *homogeneity conditions* regarding the elemental composition for the surrounding material, chamber wall, and the gas are met so that charged particle equilibrium is guaranteed throughout the sensitive volume. Or the *cavity dimensions are small* in comparison to the range of the secondary particles. Cavities fulfilling this last condition are often also referred to as *Bragg-Gray cavities*.

When homogeneity conditions are met, practical calculation of dose to a surrounding medium or tissue substitute from the charge generated within the gas can be performed by simply applying a KERMA conversion factor K_t/K_g to equation 3.1. This leads to:

$$D = \frac{Q}{m}\frac{\bar{W}}{e}\frac{K_t}{K_g} \tag{3.2}$$

K_t/K_g indicated the ratio of tissue (t) over gas (g) KERMA factors. In cases where the cavity can be considered as small, the ratio of KERMA factors for tissue and wall material (w) is used instead and an additional correction term $s_{w,g}$ for the average mass collision stopping power ratio between the wall material and the gas is introduced resulting in:

$$D = \frac{Q}{m}\frac{\bar{W}}{e}\frac{K_t}{K_w}s_{w,g} \tag{3.3}$$

In cases where Bragg-Gray cavity requirements are not fulfilled so that a significant contribution of secondary charged particles is produced in the cavity by primary radiation, the average mass collision stopping power ratio $s_{w,g}$ has to be replaced by a gas-to-wall absorbed-dose conversion factor $r_{w,g}$.

Clearly, extensive knowledge on the wall material, the gas composition, and secondary particles' spectra and ranges needs to be available in order to calculate dose from the IC reading, i.e. the charge generated in the cavity. The parameters in equations 3.2 and 3.3 can be combined to give the response function α so that - in general terms - the dose D can be calculated from the detector reading R by: $D = \alpha R$. The response function depends on the energy and type of considered radiation and can either be calculated from the respective equation above or gained from calibration

measurements. Its inverse $1/\alpha$ is referred to as the ionization chamber's sensitivity to a particular type of radiation.

Different calibration procedures are discussed in the afore mentioned ICRU reports or by Schlegel-Bickmann et al. [55]. The standard calibration procedure - also applied at MEDAPP on a recurrent basis - is performed in a *reference photon field* with known fluence and air-KERMA at the reference point. It is referred to as *fluence method* [55]. Here, usually gamma radiation from ^{60}Co with two discrete energies $E_\gamma = 1.1731$ MeV and $E_\gamma = 1.3325$ MeV is used to measure the response function. As an alternative, the calibration of ionization chambers can be performed in a *reference neutron field*. If possible, the neutron spectrum of the reference field should be comparable to the field where the actual dosimetry has to be performed. For fast neutron dosimetry, calibration in a neutron reference field provides two main benefits over calibration in a photon field [29]. First, the requirements for a small cavity need not be satisfied in cases where the reference field is comparable to the field of intended use. Second, parameters needed in equations 3.2 and 3.3 only need to be known as relative values - for the reference field and the field of interest - and not as absolute values. Even though calibration in photon reference fields is the standard, DIN 6802-6 recommends an individual calibration in neutron reference fields for specific types of ionization chambers. This is due to the fact that even for ionization chambers of the same type and identical design, large differences in the neutron sensitivity were reported [55].

For dosimetry in fast neutron fields with a significant primary gamma component, the *two chamber method* is recommended [19]. Here, two different ionization chambers of comparable size but different wall and gas compositions are used. Usually, one chamber with a high sensitivity to both neutron and gamma radiation - index T - and one with a low sensitivity to neutrons but a high sensitivity to gamma radiation - index U - are used. The wall of the neutron sensitive chamber is often made of A-150 *tissue equivalent (TE)* plastic and for the measurement it is flooded with TE gas. While metal chambers made from aluminum or magnesium provide low neutron sensitivities, magnesium has the benefit of reduced neutron activation. Argon is used to flood the gas cavity of metal chambers. The central electrodes need to be manufactured from the same material as the chamber walls.

For both types of ionization chambers, the total reading R_{total} from a dose measurement in a mixed field will be the sum of the charges generated by the neutron component R_n and the gamma component R_γ. Using a response function $\alpha_{\gamma,cal}$ known from calibration measurements in a photon reference field, a formal dose value can be calculated from equation 3.4 even though the actual dose will - of course - differ from the formal one. This effect is due to the difference between the neutron and gamma response functions.

$$D' = \alpha_{\gamma,cal}R_{total} = \alpha_{\gamma,cal}R_n + \alpha_{\gamma,cal}R_\gamma = D'_n + D'_\gamma \qquad (3.4)$$

Here, the primed last two terms D'_n and D'_γ indicate the dose formally associated to the ionization events from the two beam components. The ratio of the formal and the

actual neutron doses D'_n and D_n equals the ratio of the sensitivities in the reference photon field and the neutron field of interest. Therefore, the equality $D'_n/D_n = \alpha_\gamma/\alpha_n$ holds true. A similar relation exists for the gamma component. Introducing this ratio into equation 3.4 gives:

$$D' = \frac{\alpha_{\gamma,cal}}{\alpha_n}D_n + \frac{\alpha_{\gamma,cal}}{\alpha_\gamma}D_\gamma = kD_n + hD_\gamma \qquad (3.5)$$

Therefore, the sensitivity or response function k for neutrons and h for gammas of the used ionization chambers is always applied in reference to the calibration measurement. The reason to use ionization chambers with different sensitivities is that R_n and R_γ cannot be measured separately so that two measurements at identical measurement positions and dose rate need to be performed to infer the actual neutron and gamma dose at the measurement point. The sensitivity of one chamber should be small because for a small value even a large uncertainty of the sensitivity will only have a minor effect on the uncertainty of the absorbed neutron dose [28, p. 18].

With known response functions, the following set of equations:

$$D'_U = k_U D_n + h_U D_\gamma \qquad (3.6a)$$

$$D'_T = k_T D_n + h_T D_\gamma \qquad (3.6b)$$

for measurements with the TE and the metal chamber can be used to calculate the actual neutron and gamma dose component. Finally, D_n and D_γ can be calculated in dependence of the formal dose values D'_U and D'_T measured with the respective chambers via:

$$D_n = \frac{D'_T - D'_U}{k_T - k_U} \qquad (3.7a)$$

$$D_\gamma = D'_U - k_U D_n \qquad (3.7b)$$

While the relative neutron sensitivity values k_U and k_T differ from unity, the ratio of the photon sensitivities is usually assumed to be one due to the comparable energy range of the reference and the investigated photon field. Therefore, they were omitted in the equations above.

3.1.2 Dosimetry Equipment at MEDAPP

At MEDAPP, two sets of ionization chambers are available for dosimetry with the two chamber method. One set is manufactured by PTW-Freiburg. In this set, both ionization chambers - the tissue equivalent TM33053 and the magnesium TM33054 chamber - have a wall thickness of $d_w = 3\,\mathrm{mm}$ and the gas cavities have a volume of $V_{gas} = 1\,\mathrm{cm}^3$. The cylindrical shaped sensitive volume of these chambers has an axial extension of 25 mm and diameter of 8 mm including the central electrode. The

overall diameter is 14 mm. For the dosimetric characterization of MEDAPP, k_U and k_T values were calculated to be $k_U = 0.02$ and $k_T = 0.943$ as discussed by Wagner et al. [75]. Besides the latest air-KERMA calibration factor, additional factors as part of the response function in equation 3.4 are needed to calculate the (formal) dose. These are an air-to-gas conversion factor to account for the difference between air-filling during the calibration with photon radiation and the response of the gas-flooded chambers. In addition, an air-KERMA-to-tissue-dose conversion factor is needed. The air-to-gas conversion factor $k_{a,g}$ is measured right before dosimetry measurements with a ^{90}Sr source which is a β^--emitter. The air-KERMA-to-tissue-dose conversion factor is calculated to be $k_{a,t} = 1.112$. Furthermore, the ionization chamber measurements need to be corrected for temperature T and pressure p by multiplication with $k_f = (p_0 T)/(T_0 p)$. Here, the index 0 indicates the reference conditions during the calibration. This pair of ionization chambers is mainly used for the determination of neutron and gamma depth dose curves. If not indicated differently, the depth of the geometrical center of the ionization chambers was used as the nominal depth in water.

A second set of ionization chambers is manufactured by EXRADIN. In principle, one TE-chamber - called type T2 - and one Mg-chamber - type M2 - are again available. While the calculated neutron and gamma sensitivity are the same as for the PTW ICs, the dimensions of the T2 and M2 chambers are different. The sensitive volume is $V_{gas} = 0.5 \, \text{cm}^3$ and the wall thickness is $d_w = 1 \, \text{mm}$. Throughout this work, only the TE-chamber is used for profile measurements due to their smaller dimensions. Measurements with build-up caps for the EXRADIN chambers have shown a build-up effect up to a wall thickness of 3 mm for both types of EXRADIN ionization chambers [36].

As recommended in ICRU report 45, methane based TE-gas is used for flooding the TE-chambers and argon is used for measurements with the Mg-chambers. While a TE-gas composition of $64.4 \, \text{mol} - \% \, CH_4$, $32.4 \, \text{mol} - \% \, CO_2$, and $3.2 \, \text{mol} - \% \, N_2$ is suggested in ICRU report 45, the composition used for MEDAPP is $64.2 \, \text{mol} - \% \, CH_4$, $32.4 \, \text{mol} - \% \, CO_2$, and $3.4 \, \text{mol} - \% \, N_2$. Measurements are performed in a water phantom with outer size of $63.5 \, \text{cm} \times 63.5 \, \text{cm} \times 52 \, \text{cm}$ manufactured by PTW-Freiburg. The tank walls are made of 2 cm polymethylmethacrylat (PMMA) which is replaced by a 3 mm thin aluminum entrance window at one side of the phantom. A motorized stage is available for automated positioning of the ionization chambers via the measurement software Mephisto. While the TANDEM electrometer manufactured by PTW-Freiburg is used for measurements with Mephisto, a second UNIDOS electrometer is also available for cross-checking and consistency measurements.

3.1.3 Calibration Measurements in a Neutron Reference Field

As mentioned above, several methods for the calibration of k_U were applied in the past ([26] & [55]). Depending on the used technique, the value of k_T is either taken to

be identical with the calculated one from above or it is determined experimentally. For calibration measurements of the PTW ionization chambers in a neutron reference field performed in 2018, the methods discussed by Schlegel-Bickmann et al. [55] were adopted.

First, equations 3.6a and 3.6b were applied to determine the neutron sensitivity k_U for an experimentally determined ionization chamber reading. Here, a reference neutron field with negligible gamma component was used. In this *twin-detector method* dividing equation 3.6a by equation 3.6b and setting D_γ to zero leads to the following relation

$$k_U \propto k_T \frac{R_U}{R_T} \tag{3.8}$$

where R_i with $i \in \{T, U\}$ is the reading of the respective ionization chambers. Here, $k_T = 0.943$ was assumed to have remained unchanged from [75]. In order to check the determined values for k_U and the used value of k_T, equations 3.6a and 3.6b were used to determine k_U and k_T individually from the reference air-KERMA and the detector reading by the so-called *fluence method*. Again neglecting the gamma component of the radiation field, equations 3.6a and 3.6b can be re-written to give the following relation

$$k_i \propto \frac{R_i}{D_n} \tag{3.9}$$

Measurements free in air for the calibration were performed in the quasi-monoenergetic neutron fields provided by the national metrology institute, Physikalisch-Technische Bundesanstalt (PTB) in Braunschweig, Germany. More details on the neutron source are given in the discussion by Nolte and Thomas ([49] & [50]). The applied neutron fields had a mean neutron energy of the direct neutrons of 1.2(1) MeV and 2.5(1) MeV. At the reference position, photon over neutron ambient dose equivalent ratios in 1 cm depth in an ICRU sphere of tissue equivalent material of less than 0.0001 for $E_n = 1.2$ MeV and less than 0.001 for $E_n = 2.5$ MeV were given. For the evaluation of the calibration measurements, the mixed neutron-gamma field was approximated as pure neutron beam. Two reasons were essential to chose the neutron fields provided by PTB for calibration. One is the low photon contamination of the fields. The second reason is the energy range which is comparable to the 1.9(1) MeV mean neutron energy at MEDAPP. Thus, also the mean range of the secondary ions from elastic scattering is comparable for both the calibration and the treatment field. Therefore, the afore mentioned dependence of neutron sensitivity relative to the reference neutron field given in equation 3.5 - where $\alpha_{\gamma,cal}$ would be replaced by a $\alpha_{n,cal}$ reference value - is negligible.

In order to check the plausibility of the determined k_U values in the fission beam at MEDAPP, k_T was again taken to be constant and a measurement was performed in the mixed neutron-gamma field at a distance of 5.93 m from the converter plates. Lead shielding of additional 12.5 cm Pb was applied for the measurement to reduce the gamma component of the beam to the lowest amount possible. The lead shielding is estimated to reduce the gamma fluence at irradiation position by a factor of about

100. Since up to neutron energies of $E_n \approx 3\,\mathrm{MeV}$ the neutron cross section of Pb is dominated by elastic scattering, the neutron spectrum at irradiation position is approximated to be unaffected by the additional lead. Nevertheless, the values determined in the mixed radiation field at FRM II should be seen as an upper limit of the sensitivity due to the remaining contamination with gamma radiation.

Build-up caps are normally used for measurements with ionization chambers free in air in order to account for the build-up effect of charged particle equilibrium. For the calibrated set of ionization chambers manufactured by PTW-Freiburg, no build-up caps are available. But since the wall thickness of 3 mm for both PTW chambers is comparable to the overall wall thickness - including build-up caps - of calibration measurements for other ionization chambers using even higher neutron energies (for example discussed in [55]), the build-up effect can be considered to be accounted for in the presented calibration measurements. Measurements of the build-up effect with the EXRADIN chambers are also in good agreement with this statement [36].

As discussed above, the twin-detector method was used in both the reference neutron field at PTB and in the fission neutron field with lead shielding at MEDAPP. The neutron sensitivity of the Mg chamber was determined by equation 3.8 to be $k_U = 0.155(7)$ for a neutron energy of $E_n = 2.5(1)\,\mathrm{MeV}$ at PTB and $k_U = 0.186(6)$ in the neutron field at FRM II. No measurements were performed at $E_n = 1.2(1)\,\mathrm{MeV}$.

For the fluence method, equation 3.9 was used to determine k_i in the neutron field at PTB to be $k_U = 0.156(5)$ for $E_n = 2.5(1)\,\mathrm{MeV}$ for the Mg-chamber and to be $k_T = 0.944(33)$ and $k_T = 0.927(32)$ for the TE-chamber for neutron energies of $E_n = 2.5(1)\,\mathrm{MeV}$ and $E_n = 1.2(1)\,\mathrm{MeV}$, respectively. The calibration measurements summarized in table 3.1 were performed in July 2018. No calibration was performed for the EXRADIN ionization chamber.

To the author's best knowledge, the change in the neutron sensitivity of the metal ionization chamber is larger than any value - in the present energy range - reported before. It is remarkable that the calibration of the Mg-chamber led to a k_U value that is higher by a factor of about 8 than the one calculated and applied in [75]. This increase is not yet understood. Nevertheless, dosimetry routine measurements at MEDAPP indicate an increasing neutron sensitivity of the Mg-chamber over time.

Table 3.1: Results from calibration of PTW ionization chambers using the 'twin-detector method' in the first and second line and using the 'fluence method' in the last three lines.

Calibration	Ionization chamber	Neutron energy	Neutron sensitivity
twin-detector	TM33054 (Mg/Ar)	2.5(1) MeV	0.155(7)
method	TM33054 (Mg/Ar)	MEDAPP spectrum	0.186(6)
fluence	TM33054 (Mg/Ar)	2.5(1) MeV	0.156(5)
method	TM33053 (TE/TE)	2.5(1) MeV	0.944(33)
	TM33053 (TE/TE)	1.2(1) MeV	0.927(32)

Whether this is due to constant corrosion of the Mg components of the chamber or a completely different effect cannot be explained - and is out of the scope of this work. Nevertheless, the agreement of the results from the two calibration procedures gives good confidence that the results are reliable. Also the plausibility check performed at MEDAPP with the gamma component reduced by lead shielding agrees with the calibration. The higher k_U value determined at MEDAPP can be explained when keeping in mind that even with the large amount of lead, a non-negligible amount of gamma radiation is falsely attributed to the neutron component of the beam. For the tissue equivalent chamber, the calibration gave good reason to further apply the calculated value of $k_T = 0.943$ which agrees with the calibration measurements within the measurement uncertainty.
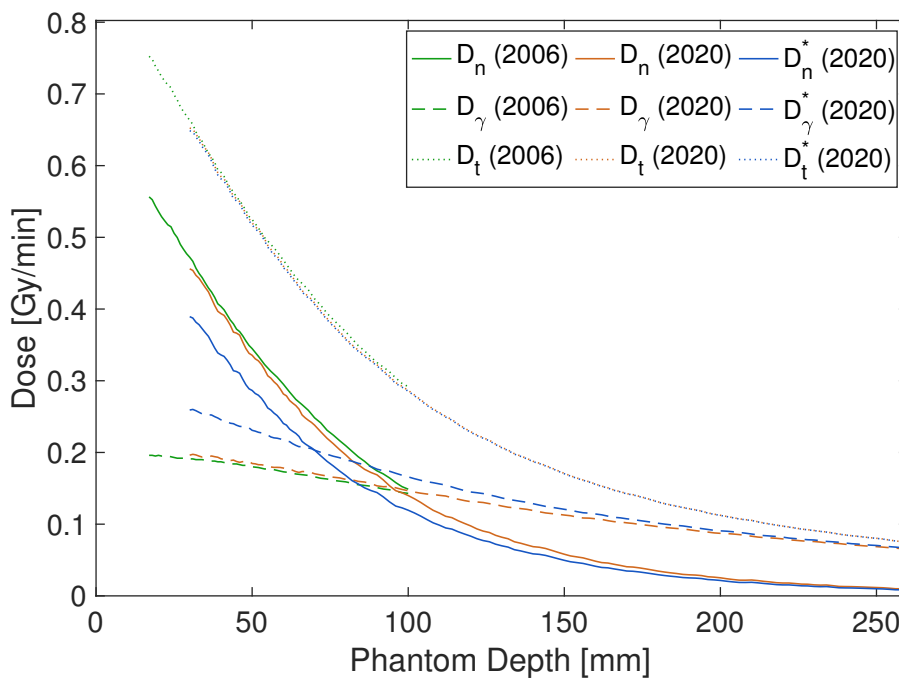
Figure 3.1: Comparison of depth dose measurements of total dose and neutron and gamma contribution from 2006 and 2020. For the blue curves, the star indicates an evaluation using $k_U = 0.02$ as also used for the data from 2006. The orange curves were generated using $k_U = 0.155$ from 2018.

In figure 3.1, a comparison of the depth dose curves of the total dose as dotted line and the neutron and gamma dose respectively shown as solid and dashed line is given for data from 2006 [75] and 2020. Since a new multi leaf collimator was introduced in 2019, the field sizes are different. In 2006, a field size of 90×90 mm^2 was used and a field size of 82×82 mm^2 was used in 2020. Also, the distance between the surface of the water phantom and the front end of the leafs facing the treatment room was changed from 112 cm in 2006 to 50 cm in 2020. For reference, the data measured in 2020 were not only evaluated with $k_U = 0.155$ as shown in orange but also with $k_U = 0.02$ as shown in blue. While the differences in the set-up need to be kept in

mind, an obvious higher reproducibility of the data from 2006 is given for $k_U = 0.155$ from the calibration measurement in 2018.

3.2 Beam Shaping for Fast Neutron Therapy at MEDAPP

For MEDAPP, the license for clinical operation was first issued in 2007. A general introduction to the set-up, spectral and geometrical beam shaping, safety measures, and dosimetric characterization was presented by Wagner et al. [77]. As mentioned above, a new multi leaf collimator (MLC) could be implemented in 2019 after a long time of in-house construction and optimization. After an intermediate version that was never actually introduced, this *MLC version 3 (MLC 3)* replaces the *first version of the MLC (MLC 1)*. The approval for treatment applications of the new MLC is ongoing. All other beam shaping devices like for example the filter combination for medical beam applications of 1 cm B_4C in epoxy (50 weight-%) and 3.5 cm lead remained unchanged. Since dose calculation approaches modelling both MLC versions were investigated in this work, the following subsections give a brief overview of both MLC versions together with examples of the depth dose and dose profiles for selected field sizes.

3.2.1 Multi Leaf Collimator 1

With MLC version 1, two leaf banks each with 20 leafs were available for field shaping. All leafs had a width of 15 mm and could be moved vertically by a portable electric drill. No leaf travelling over the central position was possible and a maximum field opening of 300×200 mm^2 was possible.

Due to the necessity to shield two different beam components, the leafs consisted of a sequence of iron, polyethylene, and lead with a total extension along the beam axis of 50 cm. As shown in picture 3.2a, the MLC was positioned within the treatment room's wall with a distance of 14 cm between the outer leaf edges facing the treatment room and the wall surface limiting the treatment room. The distance between the wall and the irradiation position was 100 cm so that an overall distance between the outer leaf edges and the irradiation position was 114 cm. Since no central leaf was present, square fields of sizes 30×30 mm^2 to 180×180 mm^2 and additional rectangular fields were available. Due to a low output and its inhomogeneous dose distribution, the smallest square field of 30 mm side length was not used for treatment.

3.2.2 Multi Leaf Collimator 3

As shown in figure 3.2b, the new MLC consists of one upper and one lower leaf bank each equipped with 19 leafs. Leaf traveling is possible in vertical up and down
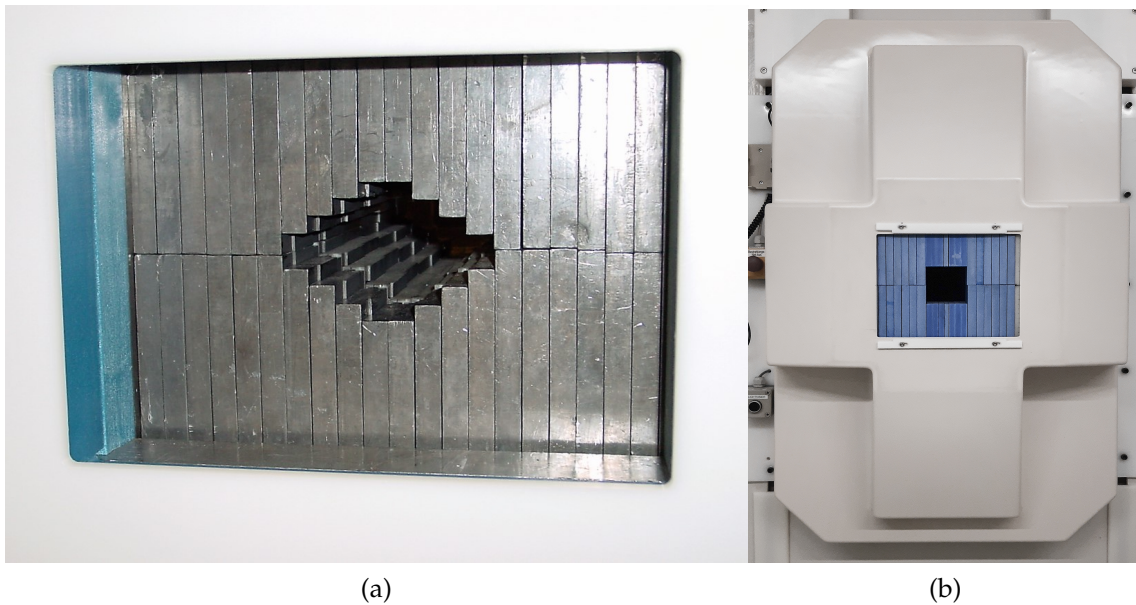
Figure 3.2: (a) Front view MLC 1. (b) Front view MLC 3.

direction, respectively, and 10 mm traveling over the central position is possible. The new MLC enables motorized leaf movement which can be controlled either via a panel inside the treatment room or from outside the room using the control computer. A time-efficient consecutive selection of different pre-defined field shapes is possible.

While all 38 leafs have identical length of 62.3 cm, the leafs' widths depend on their position within the leaf bank. The leafs are designed symmetrically around the central one and have different widths at the source-facing rear end and the front end facing the treatment room. This difference in horizontal extension accounts for the spatial extension of the converter plates. In table 3.2, field heights and widths for all possible square fields are given. In order to provide accurate values for the field sizes of the radiation fields, field sizes at the front end of the MLC were measured. All other values in table 3.2 were taken from the technical drawings of the MLC. By the design of the leafs it is intended to minimize the horizontal fall-off region for radiation fields up to 82 mm front width and to in general maximize the output for all treatment fields. Up to front widths of 82 mm, the source facing side of the MLC has a larger width than the front. For front widths starting at 146 mm, the rear sides have smaller widths. While front and rear heights are identical for all square fields, front and rear widths are only identical for 116 mm field size. For reference, the front and rear widths of the outer leafs of the different fields are given in table 3.2. The central leaf has a front width of 8.2 mm and a rear width of 18.2 mm. The maximum field opening for the new MLC is 200×268 mm^2.

Again, the leafs consist of a sequence of different materials which were selected for the attenuation of the different beam components. Since the individual leaf differ in their construction, only the material sequence of the central is given as an example.

Here, the thickness also depends on the vertical position in the leaf. Between 220 mm to 370 mm steel, between 235 mm to 385 mm boron enriched polyethylene (BPE) with a boron percentage of 20 % of weight, and between 15 mm to 25 mm aluminum (Al) are used for attenuation. A 5 mm thick window made of acrylic glass is mounted at the front end of the MLC to prevent pinching of external items when the leafs are moving. The glass is not shown in the photo in 3.2b. A layer of 3 mm boron enriched epoxy is attached to the rear end of the MLC.

The protruding front end of the new MLC extends 30 cm inside the treatment room. This extension inside the treatment room allows the treatment of patients in a sitting position very close to the collimator. The reference irradiation position is 50 cm away from the front end of the leafs and 80 cm away from the wall which leads to more flexibility for the movement of the treatment couch.

Table 3.2: Possible square field sizes and leaf widths for the new MLC. The ∗ indicates that the values were measured directly at the MLC.

Field size [mm]		Number of open leafs	Outer leaf width [mm]	
Vertical∗	Horizontal		Front	Back
34	34	6	11.5	11.5
58	58	10	11.5	11.5
82	82	14	11.5	11.5
116	116	18	17.5	7.5
146	146	22	14.5	14.5
176	176	26	14.5	14.5

3.2.3 Influence of MLC on Dose Distributions in Water

As a comparison, figure 3.3 shows the depth dose curves measured for comparable field sizes of 90×90 mm^2 and 120×120 mm^2 for MLC 1 and 82×82 mm^2 and 116×116 mm^2 for MLC 3. Figure 3.4 shows beam profiles measured in 5 cm depth in water for the same field sizes. Data from 2006 were measured by Kampfer et al. [75] and measurements from 2020 were evaluated using $k_u = 0.155$.

As shown in figure 3.3a for the field size between 8 cm and 9 cm, the neutron and gamma components of the beam measured in 2020 differ from the data from 2006. The neutron-over-gamma dose ratio in 5 cm depth in water in 2020 was measured to be 1.82 as opposed to 1.92 in 2006. It approaches unity at about 9.4 cm in depth compared to a depth of about 10 cm in 2006.

For the larger field sizes of around 12 cm, the depth dose curves for the neutron and gamma dose rate in water are shown in figure 3.3b. The neutron-over-gamma ratio in 5 cm depth is 1.76 and approaches unity at about 9.5 cm in the phantom. In 2006, a ratio of 1.79 in 5 cm depth in water was measured.
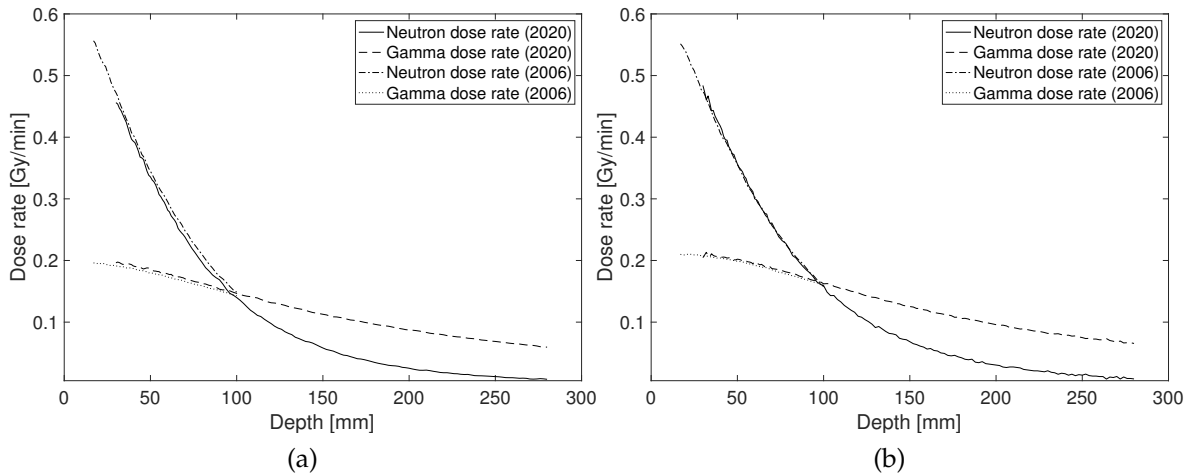
Figure 3.3: Measured depth dose components from 2006 with MLC 1 and from 2020 with MLC 3. (a) Field sizes for MLC 1 and 3 are 90×90 mm^2 and 82×82 mm^2 respectively. (b) Field sizes again for MLC 1 and 3 are 120×120 mm^2 and 116×116 mm^2.

Especially for the comparison of the beam profiles shown in figure 3.4, it is important to keep in mind that along with the MLC also the irradiation position was changed. While in 2020 the EXRADIN T2 TE ionization chamber was used for profile measurements, measurement results from 2006 for comparison were only available for the PTW TE-chamber. In figures 3.4a and 3.4b, beam profiles for the two field sizes discussed above in 5 cm depth in water are shown. Here, profiles are plotted in combination with profiles from square fields of side lengths 90 mm and 120 mm for the former MLC.

Figure 3.4a shows that the vertical and horizontal beam profiles are fairly symmetric for the square field with side length 82 mm. Nevertheless, a slightly steeper fall-off can be seen for the horizontal profile. The mean fall-off distances or penumbras for the dose to drop from 90 % to 20 % for both sides of the horizontal and the vertical profile in 5 cm depth are 23 mm and 25 mm, respectively. Beam profiles for the square field of 90 mm side length measured in 2006 show horizontal and vertical penumbras of 37 mm and 41 mm, respectively. This difference in the penumbras is also visible for the beam profiles shown in figure 3.4a. Here, the horizontal dose fall-off distance is measured to be slightly steeper than the vertical.

The penumbras for the larger field with side length 116 mm shown in figure 3.4b in 5 cm depth are determined to be 28 mm and 26 mm for the horizontal and the vertical profile, respectively. Fall-off distances for the former MLC shaping a square field with side length 120 mm are determined from measurements to be 38 mm in horizontal and 43 mm in vertical direction.

It was shown with the measured depth dose curves for the new MLC that the beam quality has not changed significantly in measures of neutron and gamma dose rates

(a)

(b)
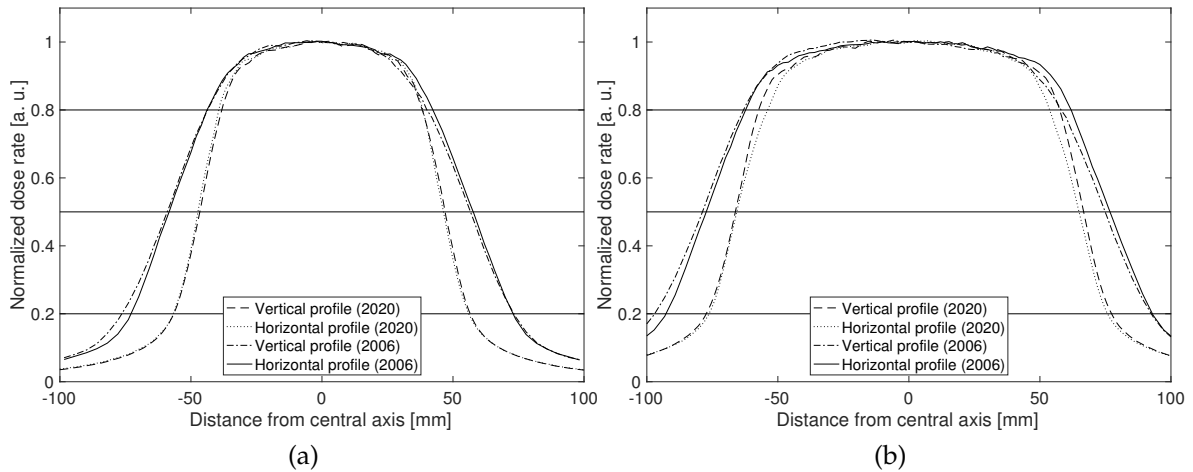
Figure 3.4: Comparison of horizontal and vertical beam profiles in 5 cm depth in water with data from 2006 for MLC 1 and from 2020 for MLC 3. (a) Field sizes for MLC 1 and 3 are 90×90 mm^2 and 82×82 mm^2, respectively. (b) Field sizes again for MLC 1 and 3 are 120×120 mm^2 and 116×116 mm^2.

in comparison to measurements from 2006 with the old MLC. Only a small change is reported. The decrease in neutron over gamma dose ratio by about 5 % from 1.92 to 1.82 in 5 cm depth in water cannot be explained solely by the uncertainty in the calibration of the k_U value. Nevertheless, it should be kept in mind that the calibration date in 2018 and the dose measurements performed in 2020 are about 1.5 years apart. In general, a lower neutron dose can be due to the fact that the field size for the measurements with the new MLC is smaller than the one used with the old MLC. This reduction of the field size of about 17 % leads to a lower contribution of neutron scattering for the smaller field size. In addition, the irradiation in 2006 was performed through the aluminum entrance window while the irradiation in 2020 was performed from the opposite side of the phantom through the PMMA wall. The attenuation of the gamma component by the 3 mm aluminum window is estimated to reduce the gamma fluence entering the phantom by about 4 % leading in turn to a lower gamma component in the irradiation condition from 2006. A gamma energy of 2 MeV was used for this estimation which is comparable to the mean gamma energy estimated for MEDAPP [34].

As shown in figures 3.4a and 3.4b, it is clear that the irradiation conditions have highly improved by the implementation of the new MLC. While the differences between horizontal and vertical beam profiles might not be as pronounced as intended by the design of the leafs, the reduced distance between irradiation position and MLC exit shows a high impact on the beam shaping abilities. Regarding the slightly steeper fall-off measured for the horizontal profile of the small field, an influence of the IC's extension in its lateral and axial directions might play a non-negligible role for the outcome of the measurement. The influence of the geometrical extension of the

ionization chambers is indicated by the fact that the large field is actually expected to be symmetrical but a clear difference is measured between the horizontal and the vertical profiles. The orientation of the IC was the same for all profile measurements. A much steeper lateral gradient is reported in comparison to fields with comparable sizes shaped by the former MLC version. Since this holds true for a field size of 116×116 mm^2 with identical field opening at the front and rear side, this is due to the reduced MLC-to-surface distance. Reducing this distance was enabled by the protruding front end of the new MLC and its extension by 30 cm inside the treatment room. With this modification a larger angle for couch rotation is feasible without colliding with the treatment room wall.

4 Implementation of Different Treatment Planning Approaches for Fast Neutron Therapy

After the discussions of the *basic principles* of fast neutron interaction and dose deposition in matter and of the *background* on mixed-field dosimetry in the previous chapters, the following chapter on the *implementation of dose calculation approaches* represents the core of this thesis.

Two approaches for dose calculation using patient anatomy information from computed tomography (CT) data were implemented. In the approach presented in section 4.1, fast dose calculation is based on decomposed **pencil beam kernels (PBK)**. As discussed for example by Söderberg et al. [63] and Kalet et al. [35], the characterization of neutrons and photons as indirectly ionizing particles motivates the application of dose calculation algorithms - like pencil beam algorithms - originally developed for photons also for neutrons. For the mixed neutron-gamma radiation field, the decomposition of PBKs is performed according to Bortfeld et al. [8]. While it is different from the analytic approach for particle transport calculations mentioned in section 2.5, this PB approach is often also referred to as analytical. Another, more time intensive but also more accurate calculation approach based on **Monte Carlo** methods is presented in section 4.2. Here, MCNP is used to directly calculate dose depositions from stochastic transport calculations (see also section 2.5).

Both approaches were integrated into the MATLAB-based open source research treatment planning software **matRad** presented by Wieser et al. [80]. The open source nature and extensive documentation of matRad showed to be highly beneficial in the implementation of changes necessary for mixed-field pencil beam calculations. For the Monte Carlo dose calculations, an additional component was implemented and added to run within the matRad infrastructure as a modular dose engine.

Besides the implementation of the dose calculation algorithms using decomposed pencil beam kernels, matRad provides all other features necessary for forward and inverse treatment planning. The most important are a data reader for patient CT and contouring data given in the digital imaging and communications standard in medicine (DICOM), a graphical user interface (GUI) for treatment planning, a ray tracing algorithm implemented according to Siddon [62], a dose-matrix-based optimization algorithm for intensity modulated radiation therapy (IMRT), and dose visualization and evaluation functions like dose visualization overlaid on CT data and

a dose volume histogram (DVH) viewer. Calculated dose information is saved in a *dose influence matrix D_{ij}*. In the D_{ij}-matrix, dose values for each bixel or in general for each field are saved as one column indicated by j. A bixel indicates a small beam element with a predefined geometric cross section. The index i indicates the voxels that are save in the matrix's rows. For linear voxel indexing, MATLAB linear matrix indexing is used. Modifications were implemented into *matRad version Alan v2.1.0* released in 2016 by the German Cancer Research Center (DKFZ). More information is provided by Wieser et al. [80] and on the project wiki on GitHub [72]. All data processing and evaluation was performed using MATLAB [43].

4.1 Dose Calculation using Pencil Beam Kernels

For the mixed neutron-gamma radiation field, the decomposition of pencil beam kernels is carried out individually for the neutron and the gamma component of the beam. For each beam component, the decomposition was done in parallel to the discussion by Bortfeld et al. [8]. For the generation of pencil beam kernels compatible with matRad, a collection of MATLAB scripts is provided by Bangert et al. [3] and was in parts used for this work. Parts of the work discussed in the following considering dose calculation using pencil beam kernels for MLC 1 were recently submitted as a paper (cf. chapter 6).

4.1.1 Methods

As shown in the example in section 2.6.2, dose deposition of primary neutron radiation is due to the interactions of secondary ions and electrons. Since the main part of electron dose deposition originates from secondary gammas that in turn generate those electrons, the contribution of gammas from neutron interaction is associated to the gamma component of the beam. Therefore, the gamma component of the depth dose curves comprises primary and secondary gammas. This separation of the aforementioned secondary ion component from neutron interaction on the one hand and the combined secondary electron component from neutron and gamma interaction on the other hand has the benefit that also the biological properties of ions and electrons could potentially be taken into account individually. Furthermore, primary and secondary gammas cannot be distinguished in measurements by the applied two chamber method. Therefore, a systematic difference between measured and simulated neutron dose is avoided when relating secondary gammas from neutron interactions to the gamma component of the beam. As discussed in section 2.3, neutron KERMA and dose deposition from secondary ions are expected to be in good correspondence for the spectrum present at MEDAPP.

As discussed in the original paper [8], the formalism can be applied to square fields by using the equivalent field size approach even though it was originally derived for

circular fields. In this approach, equivalent radii for the square fields are calculated by simply dividing the side lengths of the square fields by the square root of π.

The necessary beam parameters of the mixed neutron-gamma field for the generation of PBKs and their validation are output factors (OF), percentage depth dose (PDD) curves and beam profiles which were measured in water. In order to allow dose calculation in the build-up region close to the phantom surface and to distinguish between the direct and the scatter components of the neutron and the gamma dose deposition, Monte Carlo calculations were run. The actual steps for the generation of pencil beam kernels are discussed in the following paragraphs. This procedure was performed for both MLC versions.

Measurement of Dose Distributions at FRM II

For MLC 1, four square fields with side lengths of 6 cm, 9 cm, 12 cm, and 15 cm at the MLC exit were used for the generation of PBKs. For MLC 3, field sizes were limited to side lengths 3.4 cm, 5.8 cm, 8.2 cm, 11.6 cm, and 14.6 cm.

For MLC 1, measurements from the initial dosimetric characterization of MEDAPP from 2006 [36] were used. A dosimetric characterization of MLC 3 was performed in 2020 including the application of the new calibration factors discussed in section 3.1. Dose measurements for all square fields were carried out in the cuboidel water phantom manufactured by PTW-Freiburg present at MEDAPP. The phantom was placed at a distance of 114 cm and 50 cm from the exit of MLC 1 and MLC 3, respectively. The distance was measured between the outer leaf edge and the outer surface of the phantom facing the respective MLC. Output factors were measured in the water phantom in a reference depth $d_{ref} = 5$ cm.

Irradiation measurements in 2006 with MLC 1 were performed through the aluminum entrance window applying the two chamber method. Due to the finite extension of the ionization chambers and the entrance window, the measurements started at 17 mm depth in water. In 2020, measurements for MLC 3 were performed by irradiating the water phantom through the tank wall from the opposite side of the entrance window. Therefore, measured data start at 30 mm depth in the phantom after 20 mm tank wall and 10 mm water. No method for correction of the effective point of measurement of the chambers was applied. Selected results from the dosimetric characterizations of both MLCs were already shown in chapter 3.

Monte Carlo Simulation of Dose Distribution

The depth dose curves (DDC) in water for the generation of pencil beam kernels were generated using MCNP. As discussed above, MCNP offers a variety of tallies to adequately record dose deposition generated by radiation transport through media [79].

For the mixed neutron-gamma radiation field generated by the converter plates, two separate simulations - one for the neutron and one for the gamma component -

had to be run for each considered square field. The transport of neutrons, gammas, and secondary charged particles was not followed through the beamline repetitively in order to save computational resources. Instead, the neutron and gamma spectra known free in air at patient position in the treatment room were used as an input. A simplified simulation geometry of MEDAPP without filters was used. The components of the beamline other than the water phantom were voided so that all particles entering the void components surrounding the transport tunnel were not followed further and therefore deleted. This simplification was done in order to adequately approximate the particle velocity vector distributions at the MLC exit. The neutron spectrum obtained by Breitkreutz et al. [11] was used as input spectrum for the MCNP simulations. For the gamma spectrum, a modified version of the one discussed by Jungwirth et al. [34] as provided by Breitkreutz [10] was used.

A water cuboid with the same outer dimensions as the water phantom used for the measurement was positioned at 115 cm and 50 cm distance downstream from the exit of MLC 1 and MLC 3, respectively. For MLC 1, the difference of 1 cm in the distance between the water phantom and the MLC exit is due to a shift in the positioning of the water phantom in the simulations. The effect on the difference in the field sizes is estimated to be less than 0.5 % so that it was not necessary to re-run the simulations. The tank walls and the entrance window were not modeled in the simulation. The effect of the tank wall on the dose deposition in water was investigated for one square field of side length 8.2 cm for MLC 3. Within the first 13 cm depth in water behind the tank wall, it was found to cause deviations within 4 % for the gamma component and within 10 % for the neutron component. Apart from neutrons and photons, particle generation and transport was switched on using the MODE card for electrons and positrons as well as for protons and all heavier ions available in MCNP. Particle energies were defined using the CUT card so that neutrons were simulated down to 0 eV, photons and electrons down to 1 keV, and all ions down to 1 eV. Total energy deposition on the central beam axis tallies was recorded using +F6-tallies so that an adequate summation of energy transfer from primary to secondary particles could be guaranteed. In order to record the particle specific energy deposition, F6-tallies were used for the considered particle species.

In order to define the geometry of the F6- and +F6-tallies, cylinders of 2 mm heights were placed along the central beam axis with the radius vector perpendicular to the axis. Since the contribution of scattered particles towards the central axis is essential for the decomposition of PBKs [8], tallies were flagged to record not only the energy deposition inside the respective cylinder but also the contribution from particles and their secondaries entering the cylinder by passing through the lateral area. Cylinders were defined to have a diameter of $d_{cyl} = 1.5$ cm which is in approximate agreement with the outer diameter of the ionization chambers of $d_{IC} = 1.4$ cm used for the measurements. Regarding lateral charged particle equilibrium, the cylindrical tallies have a sufficient extension to cover the expected continuous slowing down electron range of about 1 cm from Compton electrons generated by interaction with

the $E_\gamma = 2.224$ MeV from neutron capture of hydrogen (cf. [54] & [7]). d_{cyl} also corresponds to the leaf width of MLC 1. The tally resolution in axial direction is chosen fine enough to record the build-up effect along the central axis. In order to tally the lateral beam profile, TMESH-tallies with a grid resolution of 2.5 mm were used. These tallies are an equivalent to the +F6-tallies but can be defined on a mesh.

For the accuracy of the simulation, an accurate sampling of the energy distributions of starting particles and a smooth distribution of particle velocity vectors at the beam exit window of the MLC are of high importance. In order to ensure an accurate particle distributions, 10^8 starting neutrons and gammas were sampled. This number of starting particles is a good tradeoff to ensure both a sufficient precision and an acceptable runtime.

Pencil Beam Kernel Decomposition

In the following, the decomposition of pencil beam kernels for the mixed neutron-photon field will be discussed in parallel to the structure of the theoretical description given by Bortfeld et al. [8]. Main aspects of the decomposition will also be mentioned in the following.

Coordinate System: Since the decomposition of the pencil beam kernels is originally based on an approximation of the source as a point source, the extension of the converter plates used to generate fast neutrons and gammas at MEDAPP makes it necessary to use a virtual point source position. The source to axis distance (SAD) of this virtual point source is approximated to be infinite by setting it to $SAD_{virt} = 50$ m.

With this virtual point source approximation, the transformation into a fan-line coordinate system as described in [8] and implemented in matRad (cf. [80]) is appropriate. In order to account for the fan-line system, the field sizes are not defined at the MLC exit but at the reference positions in air for the respective MLCs. While a large virtual SAD_{virt} is used, the actual geometry of the beamline in turn is used for the description of the reference field sizes where the converter plates are $SAD_{cp,1} = 5.97$ m and $SAD_{cp,2} = 5.77$ m away from the reference position for MLC 1 and MLC 3, respectively. For MLC 1, the field sizes at the reference position in air were calculated to be 7.4 cm, 11.1 cm, 14.8 cm, and 18.5 cm using a point source approximation with $SAD_{cp,1}$ for the square field sizes at the MLC exit. For MLC 3 with $SAD_{cp,2}$, field sizes at reference position were calculated to be 3.8 cm, 6.4 cm, 9.1 cm, 12.8 cm, and 16.1 cm. The SAD values were defined in a rather heuristic manner.

Base Data and Pencil Beam Kernel Decomposition: The base data for the PBK decomposition consists of two main components that both need to be gained for neutron and photon irradiation fields separately. The first component are output factors measured at reference depth in the water phantom by the two chamber method for all field sizes. Simulated PDDs normalized to reference depth in water are the second component. As given by equation 4.1, the actual depth dose curves $D(r_{eq}, d)$ can be reproduced for the equivalent circular field sizes r_{eq} by multiplication of the

simulated PDD curves with the measured output factors.

$$D(r_{eq}, d) = OF(r_{eq})_{meas} PDD(d)_{sim} \tag{4.1}$$

Simulated PDDs and measured OFs are extrapolated to zero field size. Following the decomposition in [8], equation 4.2 represents the approximation of the field-size-dependent depth dose curves by three components $D_i(d)$ that are weighted by $W_i(r_{eq})$. The components $D_i(d)$ represent the direct and scattered contribution for the smallest square field for $i = 1$ and $i = 2$, respectively, and the scattered contribution for the largest available square field for $i = 3$.

$$D(r_{eq}, d) \approx \sum_{i=1}^{3} W_i(r_{eq}) D_i(d) \tag{4.2}$$

Since $D(r_{eq}, d)$ is known from MC simulations for all square fields with their respective equivalent circular field sizes, fitting the contributions $D_i(d)$ to the field-size-dependent simulated PDDs in dependence of $W_i(r_{eq})$ gives the fitted values for weights. For the fitting procedure and also for the actual dose calculations, the components $D_i(d)$ need to be described analytically. As a modification of the approach used by Bortfeld et al. [8], equation 4.3 was chosen for fitting the simulated direct and scattered contributions. Here, a second exponential term was introduced in the convolution in order to allow higher flexibility in the fitting process.

In a first step, the parameter μ is obtained by an exponential fit of the direct contribution of the smallest field to the depth dose at the central beam axis. It can be interpreted as the attenuation coefficient from equation 2.8 and will of course be different for neutrons and photons. The four fitting parameters $\beta_{i,j}$ with $j \in \{1, 2, 3, 4\}$ are then obtained in a second step.

$$\begin{aligned} D_i(d) &= \int_{-\infty}^{\infty} e^{-\mu d} [\beta_{i,1} e^{-\beta_{i,2}(d-\hat{d})} + \beta_{i,3} e^{-\beta_{i,4}(d-\hat{d})}] d\hat{d} \\ &= \frac{\beta_{i,1}}{\beta_{i,2} - \mu} [e^{-\mu d} - e^{-\beta_{i,2}}] + \frac{\beta_{i,3}}{\beta_{i,4} - \mu} [e^{-\mu d} - e^{\beta_{i,4}}] \end{aligned} \tag{4.3}$$

Equation 4.4 states the final equation necessary for the calculation of the dose deposition D_{irr} at a lateral position (x_p, y_p) for an arbitrary field shape $F(x, y)$ along a pencil beam in depth d using a source-dependent primary energy fluence $\Psi(x, y)$.

$$D_{irr}(x_p, y_p, d) \approx \sum_{i=1}^{3} D_i(d) \int_{-\infty}^{\infty} \int_{-\infty}^{\infty} \Psi(x, y) \, F(x, y) \times w_i(x_p - x, y_p - y,) \, dx \, dy \tag{4.4}$$

The components $w_i(r_{eq})$ in equation 4.4 are obtained by differentiation of the initial weights $W_i(r_{eq})$ and division with the primary energy fluence normalization $\Psi_n(r_{eq}) = \int_0^{2\pi} \Psi(r_{eq}, \phi) \, r \, d\phi$. In practice, the numerical integration - here written in cylinder coordinates - is performed by discretization of the primary energy fluence

as a two-dimensional matrix and summing the contribution of all matrix elements with a specific radial distance. The primary energy fluence $\Psi(x, y)$ is defined for the largest possible square field at reference position in air.

As a result, equation 4.5 describes the decomposed pencil beam kernel as product of weights and direct and scattered contributions. To enable dose calculation of different field sizes other than the ones used as base data, the summands in equation 4.5 are interpolated in dependence of r.

$$K(r, d) = \sum_{i=1}^{3} w_i(r) \, D_i(d) \qquad (4.5)$$

An additional convolution of equation 4.4 with a Gaussian function to account for the spatial extension of the point source is originally suggested. For MLC 1, a Gaussian function is fitted to the beam profile at reference position free in air. The beam profile was calculated for the smallest field with 6 cm side length at the MLC exit as described by [11]. For MLC 3, the convolution with an additional Gaussian function is omitted.

Implementation of Dose Calculation

As already mentioned, the pencil beam kernels calculated by the procedure described above were generated in a way to be compatible with the matRad version Alan v2.1.0.

The open-source character of matRad allowed the following changes necessary for the calculation of mixed neutron-photon dose. First, the different MLC geometries had to be accounted for. Second, the second exponential term used for the convolution of equation 4.3 had to be added in the implemented dose calculation function. Finally, the dose calculation has to be performed in two steps in order to calculate both the dose contribution from neutrons and from photons. The additional benefit of this dose splitting regarding the use of multiplicative parameters for the two dose components was already mentioned above.

Corrections for Tissue Heterogeneities

A lookup table to convert Hounsfield Units (HU) to a voxel-specific relative electron density is usually used in the ray tracing process for photons to calculate the radiological depth of each point in the voxelized phantom (cf. [62] & [80]). For photons, the relative electron density is used to scale the linear attenuation coefficients for the photon radiation along the path through the voxels. A similar approach can be used for neutrons due to the comparable exponential depth dependence of the neutron attenuation. As suggested by Söderberg et al. [63], the linear attenuation coefficient for photons can be replaced by the macroscopic total cross section for neutrons in order to calculate the radiological depth d_{rad} for neutron radiation (see also chapter 2). Due to the energy dependence of the total macroscopic cross section, it is necessary to calculate an averaged value for the neutron spectrum present at MEDAPP according

to equation 2.10. The calculation of energy-dependent cross section data for water, soft tissue, lung tissue, and bone using MCNP for the MEDAPP spectrum was provided as example in section 2.6.1. It is clear that calculating the average total macroscopic cross section for the initial spectrum cannot account for the expected depth-dependent change in the neutron spectrum. Similar to the concept of relative electron density, the averaged cross section for water is used as the reference value.

Furthermore, Söderberg et al. [63] discuss dose correction factors for different tissues. They suggest that in order to obtain dose-to-tissue from dose-to-water calculated using the PBKs, the result should be multiplied by the ratio of the average KERMA factor for the particular tissue over the average KERMA factor for water. For the neutron spectrum present at MEDAPP, the averages of the KERMA factors $\bar{f}_K$ are calculated similar to the calculation of the averages of the cross sections for water, soft tissue, lung tissue, and bone. Data for the KERMA factors f_K were taken from ICRU report 63 [31]. Equation 4.6 gives the relation to calculate the depth-dependent dose-to-tissue $D_t(d)$ from dose-to-water $D_w(d_{rad})$:

$$D_t(d) = D_w(d_{rad}) \frac{\bar{f}_{K,t}}{\bar{f}_{K,w}} \tag{4.6}$$

Here, the indices t and w indicate tissue and water, respectively.

4.1.2 Results

In the following section, the performance of the PB algorithm in the calculation of dose-to-water for both MLC versions will be discussed. For MLC 1, additional results of dose-to-tissue calculations using the corrections for radiological depth and KERMA factors will be discussed for two different heterogeneous slab phantoms and an actual patient CT. For the discussion of the outcome, it is important to keep in mind that the generation and the depth-dependent fine tuning of the PBKs is mainly performed using data from MC simulations so that the PB algorithm can only perform in agreement with the simulation results. Therefore, the evaluation of the PB algorithm's performance refers to simulated data as ground truth.

Generation and Evaluation of Pencil Beam Kernels for MLC 1

In figure 4.1, the depth-dependent contribution of the direct and scattered secondary ion doses $D_i(d)$ and the field-size-dependent weights $W_i(r)$ for the PBK calculation according to equations 4.2 and 4.5 are shown for primary neutron radiation. Fitted curves and weights for the primary gamma component from fission reactions with an additional (secondary) contribution from neutron interactions within the medium are given in figure 4.2. In figures 4.1a and 4.2a, the red and green lines, respectively, show the direct and scattered contribution on the central beam axis simulated for the smallest square field of size 6×6 cm^2. The scattered contribution for the largest square field of size 15×15 cm^2 is shown in blue. Analytical fits to the simulated
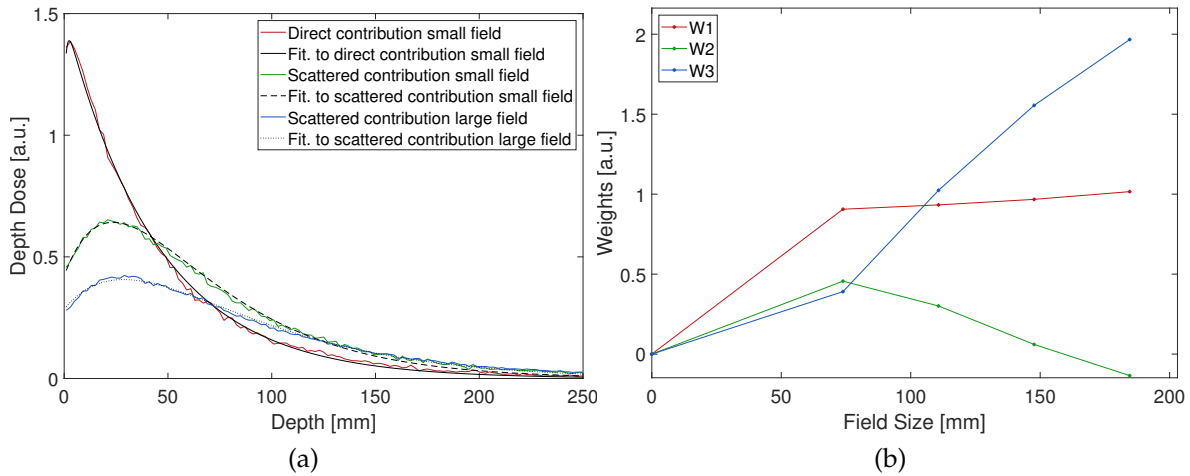
Figure 4.1: Pencil beam kernels for **neutron component** of MLC 1: (a) Analytical fits to normalized simulation data for direct and scattered contribution for primary neutrons. (b) Fitted weights for direct and scattered components of simulated dose for different field sizes.

data for the different components according to equation 4.3 are plotted as black solid, dashed and dotted lines. The shown depth dose curves are again normalized to the total dose for the respective field size in reference depth.

As shown in figure 4.1a for the **neutron** component, the contribution from scattered radiation in the small field starts to exceed the direct contribution to the cylindrical tallies on the central beam axis at a depth of $4-5$ cm. The fitted attenuation coefficient $\mu_{n,fit}$ - i.e. the macroscopic cross section - for neutrons in water in equation 4.3 was fitted to the direct depth dose curve of the smallest field. It was obtained to be $\mu_{n,fit} = 0.0225\,\mathrm{mm}^{-1}$. The fitted value $\mu_{n,fit}$ can be compared to the calculated one $\mu_{n,calc} = 0.0256\,\mathrm{mm}^{-1}$. The comparison indicates a deviation for the fitted value of 12 %. The β-values were obtained to be $\beta_{1,1} = 0.3427\,\mathrm{mm}^{-1}$, $\beta_{1,2} = 0.9936\,\mathrm{mm}^{-1}$, $\beta_{1,3} = 89.0877\,\mathrm{mm}^{-1}$, and $\beta_{1,4} = 77.7102\,\mathrm{mm}^{-1}$ for the direct component of the small field, $\beta_{2,1} = 29.2425\,\mathrm{mm}^{-1}$, $\beta_{2,2} = 69.3656\,\mathrm{mm}^{-1}$, $\beta_{2,3} = 0.0326\,\mathrm{mm}^{-1}$, and $\beta_{2,4} = 0.0347\,\mathrm{mm}^{-1}$ for the scattered component of the small field, and $\beta_{3,1} = 5.6998\,\mathrm{mm}^{-1}$, $\beta_{3,2} = 20.0289\,\mathrm{mm}^{-1}$, $\beta_{3,3} = 0.0168\,\mathrm{mm}^{-1}$, and $\beta_{3,4} = 0.0214\,\mathrm{mm}^{-1}$ for the scattered component of the large field. For the respective fits, the sums of squared residuals were obtained to be 0.006, 0.281, and 0.160.

The build-up effect is more pronounced for the depth dose curves of the **gamma** radiation shown in figure 4.2a. At a depth of $8-12$ cm, the contribution from the scatter radiation starts to exceed the direct contribution for the small field. Furthermore, the contribution of gammas from neutron capture reactions and other nuclear interactions can be identified especially in the scattered component of the large field as a shoulder in the region of exponential decrease between $6-14$ cm depth. The attenuation coefficient of water for gammas $\mu_{\gamma,fit}$ was fitted to be $\mu_{\gamma,fit} = 0.0051\,\mathrm{mm}^{-1}$
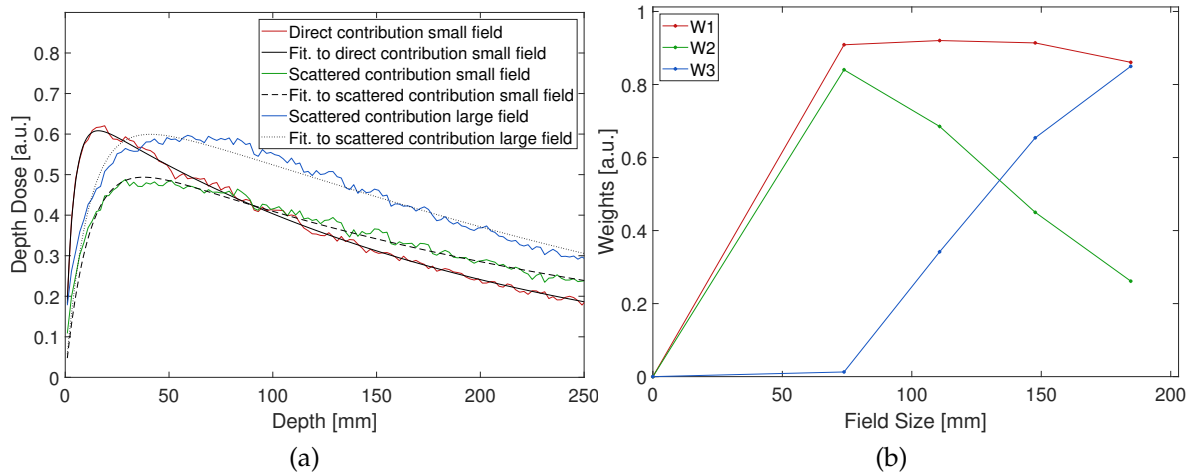
Figure 4.2: Pencil beam kernels for **gamma component** of MLC 1: (a) Analytical fits to normalized simulation data for direct and scattered contribution for primary gammas and additional secondary gammas. (b) Fitted weights for direct and scattered components of simulated dose for different field sizes.

and the β-values were obtained to be $\beta_{1,1} = 0.1054 \, \text{mm}^{-1}$, $\beta_{1,2} = 0.8855 \, \text{mm}^{-1}$, $\beta_{1,3} = 0.1261 \, \text{mm}^{-1}$, and $\beta_{1,4} = 0.2322 \, \text{mm}^{-1}$ for the direct component of the small field, $\beta_{2,1} = 0.0489 \, \text{mm}^{-1}$, $\beta_{2,2} = 0.8751 \, \text{mm}^{-1}$, $\beta_{2,3} = 0.0008 \, \text{mm}^{-1}$, and $\beta_{2,4} = 0.0030 \, \text{mm}^{-1}$ for the scattered component of the small field, and $\beta_{3,1} = 0.0024 \, \text{mm}^{-1}$, $\beta_{3,2} = 0.0077 \, \text{mm}^{-1}$, $\beta_{3,3} = 0.0575 \, \text{mm}^{-1}$, and $\beta_{3,4} = 0.0914 \, \text{mm}^{-1}$ for the scattered component of the large field. The sums of squared residuals were obtained to be 0.166, 0.073, and 1.572 for the respective fits.

In figures 4.1b and 4.2b, field-size-dependent weights $W_i(r)$ for the three components of the kernel are shown with the same color coding as in the figures on the left. Zero weights are set for zero field sizes for both neutrons and gammas. While the weights for the direct component only increase slowly with increasing field size for **neutrons**, strong dependence on the field size is shown for the scattered components of the small and large fields. The fitted weights for the scattered contribution are dominated by the large field contribution for three out of four field sizes. For the small field scatter contribution for the largest field size, a negative value is reported. As discussed in [8], the negative value obtained in the fitting procedure can be interpreted as a compensation for an over-estimation of the large field scatter.

The weights for the direct **gamma** contribution given in figure 4.2b also show a small dependency on the field size. A small decrease is observed for the last two field sizes in comparison to the second one. This decrease is probably due to the increasing contribution from secondary gammas that are not incorporated in the direct component but are associated to the scatter components of the small and large field. For these scatter components the weights are dominated by the small field for the smaller two field sizes and by the large field for the larger two field sizes. For the

weights of the gamma component, no negative values are reported.

For the depth dose curves from neutron and gamma radiation calculated for the available field sizes, the mean relative error for both neutron and gamma heating was below 3 % and the maximum relative error was below 10 %. As stated above, a tradeoff between runtime and precision had to be accepted for the Monte Carlo calculations so that the focus was on an acceptable low relative error for the primary beam components. For the secondary charged particle heating, the limited available runtime resulted in higher values for the relative error up to about 30 % for the mean and even 100 % for the maximum. An inspection of the depth-dependence of the relative error showed an increase with increasing depth, which was expected.

Evaluation of Calculated Dose Deposition in Water

For the neutron and gamma dose deposition in water, figures 4.3, 4.4, 4.5, and 4.6 show comparisons between measured PDDs (blue) and calculated PDDs using either MCNP (green) or the pencil beam algorithm (purple). Measured curves start at 17 mm depth in water. All PDDs are normalized to 5 cm reference depth in water.

Considering **neutron radiation** first, figures 4.3 and 4.4 respectively show the comparison for the smallest and the largest field size. The percentage deviation of the dose calculated with the PB algorithm from the MCNP dose calculation is indicated by the black curve associated to the right ordinate. As stated before, the MC dose calculation is used as reference. Within the first $5 - 7$ cm, deviation of less than 5 % are achieved for all field sizes. Deviations of less than 10 % are achieved up to 15 cm depth again for all field sizes. For larger depths, large percentage deviations are reported. It can be seen from figures 4.3 and 4.4 that the shape of the fall-off region can be reproduced quite well by the PB approach. The build-up effect is overestimated by the PB calculations especially for the large field as can be seen for the first millimeters in figure 4.4.

Several aspects need to be kept in mind that influence the accuracy of the MC simulations and therefore deviations between MC calculations and depth dose measurements evident in figures 4.3 and 4.4. First, the outcome of the comparison is affected by differences in the actual neutron spectrum present at MEDAPP and the input spectrum for the simulations. Furthermore, the actual sensitivity of the ionization chambers to neutron radiation used for measurements in 2006 potentially deviates from the theoretical value of $k_U = 0.02$ and might therefore also affect the separation of neutron and gamma components [55]. Measurements should only be performed in regions behind the maximum of dose deposition due to the requirement of secondary charged particle equilibrium for dose measurements with ionization chambers. This requirement is fulfilled for neutrons for all considered square fields.

A comparison between measured and calculated depth dose curves for the **gamma component** of the mixed field in water is shown in figures 4.5 and 4.6. The color code is the same as in in figures 4.3 and 4.4. Deviations of the PB calculation are again reported with reference to MC calculations. Deviations of more than 10 % are
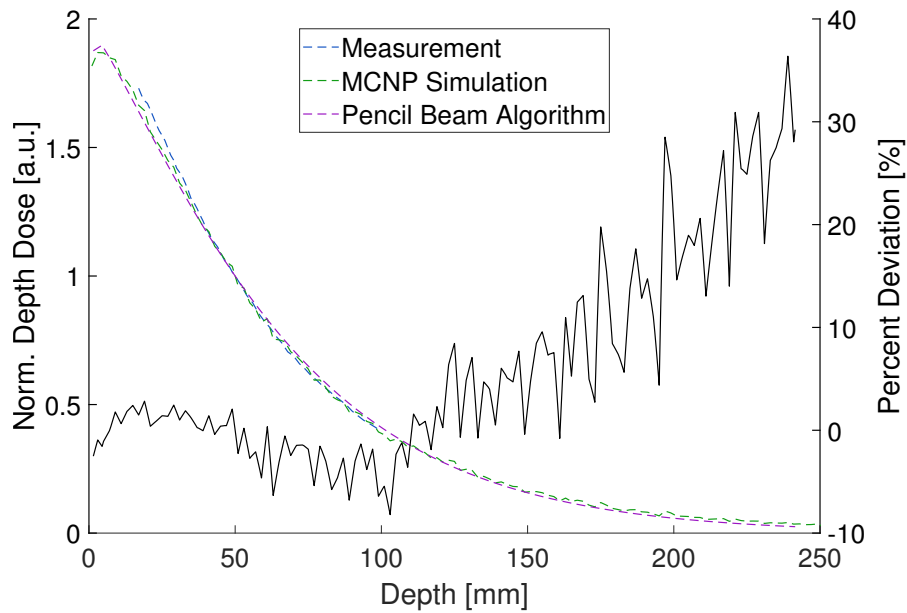
Figure 4.3: Comparison of measured depth dose curve (blue) and calculated ones using MCNP (green) and pencil beam kernels (purple) for **neutron** component and field size 6×6 cm^2.
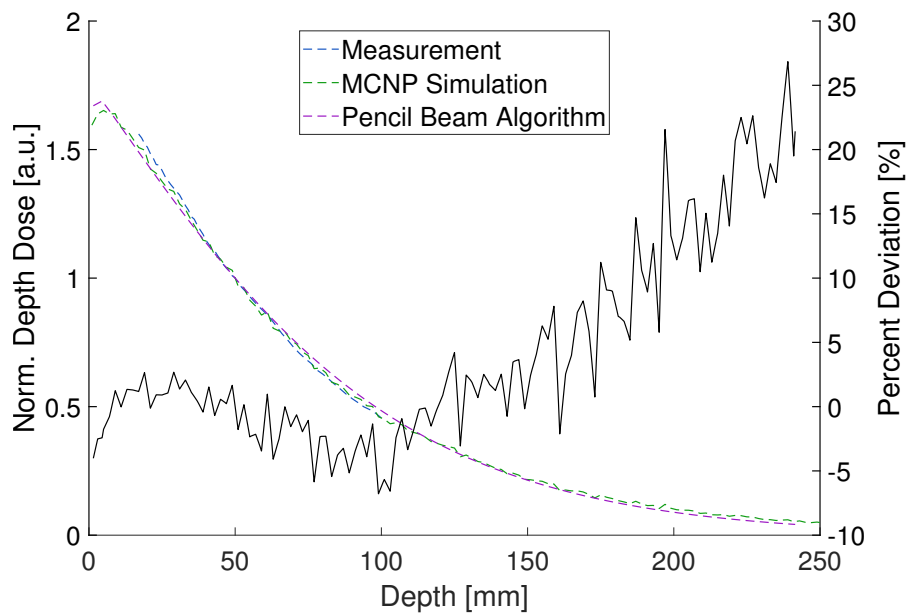
Figure 4.4: Comparison of measured depth dose curve (blue) and calculated ones using MCNP (green) and pencil beam kernels (purple) for **neutron** component and field size 15×15 cm^2.
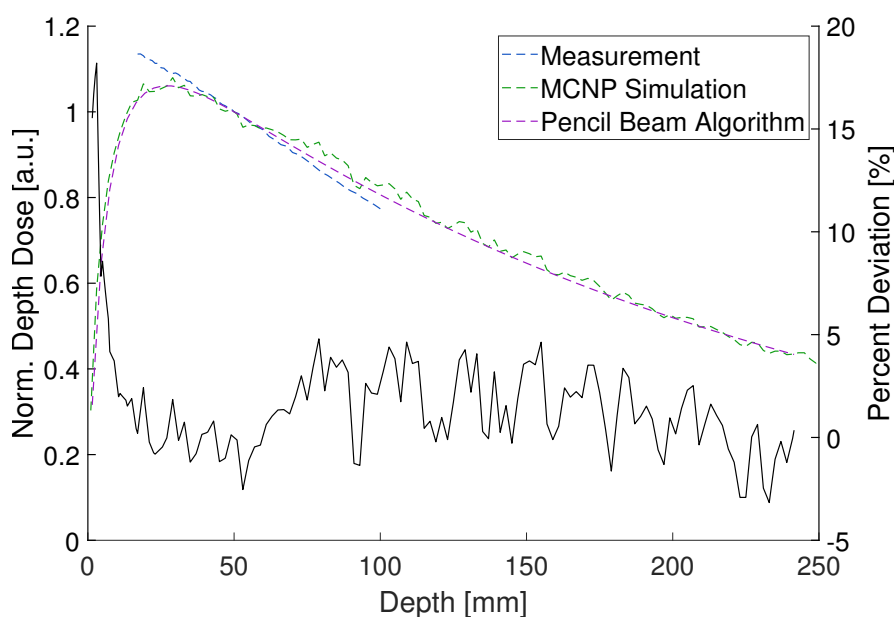
Figure 4.5: Comparison of measured depth dose curve (blue) and calculated ones using MCNP (green) and pencil beam kernels (purple) for **gamma** component and field size 6×6 cm^2.

reported depending on the field size for the build-up region in the first $5 - 10$ mm. Agreement within ± 8 % is achieved for all field sizes for depths larger than 10 mm. It can be seen from a direct comparison of the MC and the PB calculations that dose deposition from secondary gammas from neutron capture reactions in the fall-off region of the depth dose curve are hardly represented in the PB calculations. This effect is visible especially for the large field of 15×15 cm^2 for depths between 50 mm and 180 mm in figure 4.6.

Again, deviations between measured and simulated data are reported. While large deviations are visible for the small field, better agreement is given for the large field. The visible difference for the small field in the build-up region for gamma radiation can be explained by the requirement of CPE mentioned above. The MC simulations with the MEDAPP gamma spectrum indicate a minimum depth necessary for the agreement between photon KERMA and deposited dose that is field-size independent. A meaningful comparison of measured and simulated PDDs is possible starting at about $25 - 30$ mm depth. The ionization chamber's radius has to be added to the depth of agreement. Better agreement is achieved when comparing results starting at a depth of 30 mm. In addition to the influences of the simulation input and the measurement procedure discussed above, the primary and secondary gamma depth dose curves are expected to be slightly shifted in the measurement due to attenuation and neutron activation of the aluminum entrance window. The entrance window only affects the measurement and is therefore not modeled in the MC simulations of the PDDs for the PBK decomposition.

A comparison between measured and calculated *beam profiles* is shown in figures
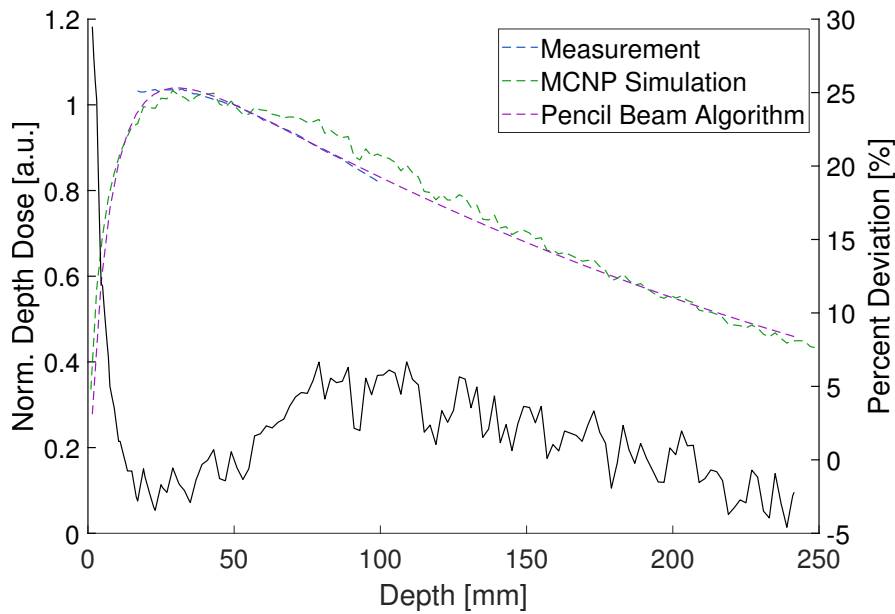
Figure 4.6: Comparison of measured depth dose curve (blue) and calculated ones using MCNP (green) and pencil beam kernels (purple) for **gamma** component and field size 15×15 cm^2.

4.7 and 4.8. Again, measured data is visualized in blue while the MC simulations and the PB results are indicated in green and purple, respectively. The beam profiles are shown in reference depth of 5 cm.

It can be seen in figure 4.7 for the **neutron beam profile** that the performance of the PB algorithm is better in the higher dose region down to about 40 % of the central axis dose. As discussed above, a convolution with a Gaussian function was used to model the penumbra by fitting the Gaussian to the smallest field profile free in air. Especially the reproduction of the beam profile's full width at half maximum was addressed with high priority in the fitting process. In the higher dose region, good agreement between measurement and calculation with the PB algorithm is achieved. In the low dose region, an overestimation of the dose probably leads to an overestimation of the scatter component in the lateral region. A high contribution of the scatter component as shown in figure 4.1b is not adequate in the lateral region since only a reduced amount of primary radiation can be scattered in the vicinity of the outer beam edges. Due to the more accurate representation of the beam line geometry and scattering effects in the medium by the MC simulation, better results in the reproduction of the beam profiles in comparison to measurements are achieved. For a direct comparison of the MC simulation with the measurements, the effect of the final extension of the used ionization chambers of $d_{IC} = 1.4$ cm has to be kept in mind. The extended sensitive volume of the ionization chambers acts like an average filter in the measurement. It can be seen in figure 4.7 that this effect is more pronounced in the lateral region of the beam profile where non-linear fall-off is present.

For the **gamma beam profile**, better agreement between the pencil beam calculations
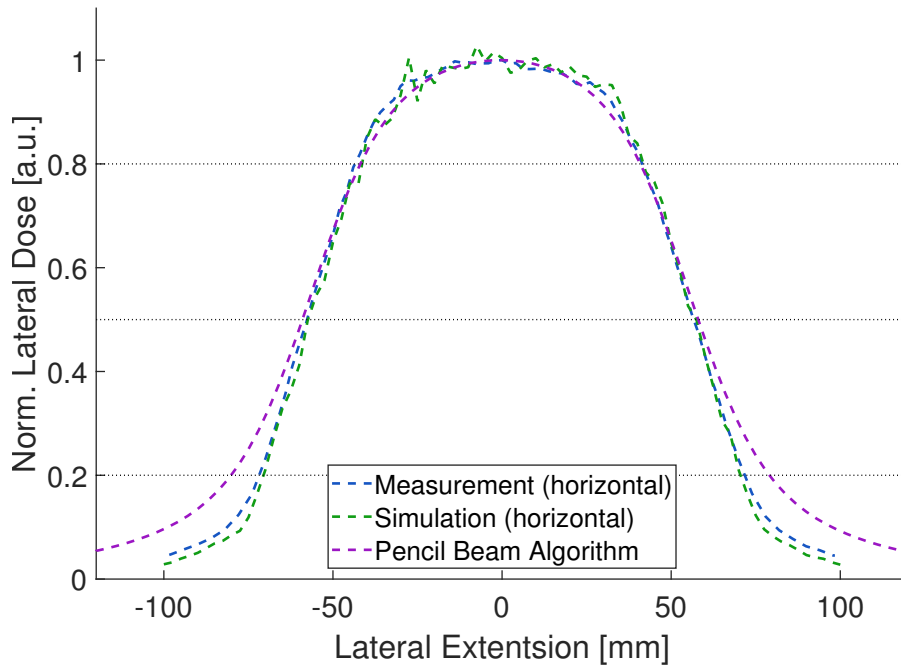
Figure 4.7: Horizontal beam profile comparison for measured (blue) and calculated data using MCNP (green) and pencil beam algorithm (purple) for **neutron** component and field size 9×9 cm^2 in 5 cm depth.
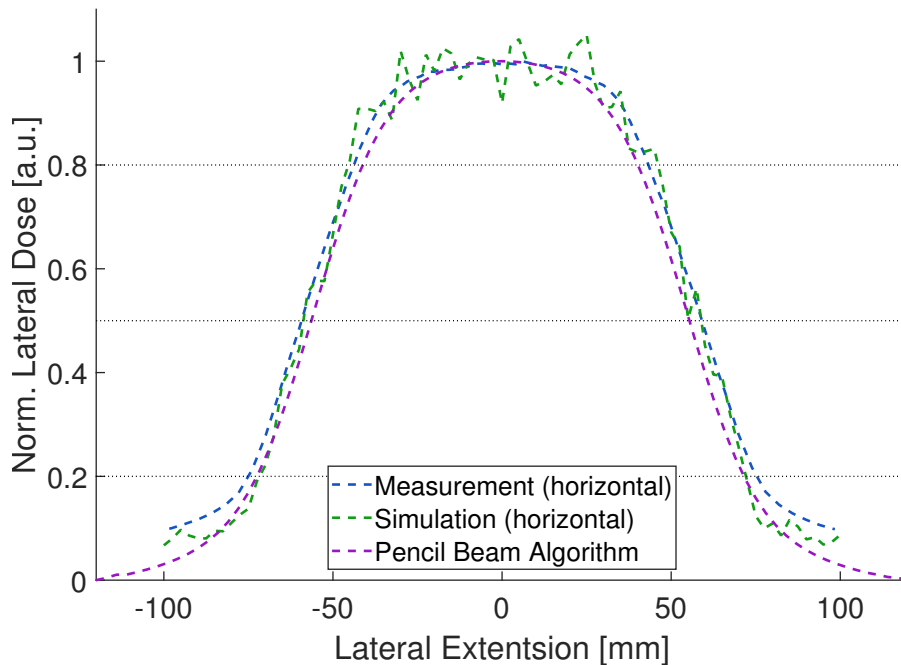
Figure 4.8: Horizontal beam profile comparison for measured (blue) and calculated data using MCNP (green) and pencil beam algorithm (purple) for **gamma** component and field size 9×9 cm^2 in 5 cm depth.

and the MC simulations is achieved as shown in figure 4.8. Good agreement between the calculated and the measured dose profiles is reported down to 20 % of the central axis dose. The better agreement of the PB results with MC simulations and measured data for the gamma radiation can be explained by the lower weights for the scatter radiation as shown in figure 4.2b.

Evaluation of Calculated Dose Deposition in Heterogeneous Slab Geometry

As discussed in the paragraph on corrections for tissue heterogeneities, correction factors for both, the radiological path length and the deposited tissue-dose, were calculated for lung, soft tissue, and bone for the primary neutron spectrum at MEDAPP. In the following, the impact of those corrections is detailed for MLC 1 while no conceptual difference is expected for MLC 3. Correction factors for the radiological path length were calculated to be $c_l \approx 0.25$, $c_{st} \approx 0.95$, and $c_b \approx 0.91$ for lung (l), soft tissue (st), and bone (b), respectively. As stated in the example in section 2.6.1, corresponding mean free path lengths obtained from the macroscopic total cross sections are $r_l \approx 15.64$ cm, $r_{st} \approx 4.10$ cm, and $r_b \approx 4.24$ cm. KERMA correction factors for the deposited dose relative to water were calculated to be $k_l = 0.96$, $k_{st} = 0.93$, and $k_b = 0.38$.
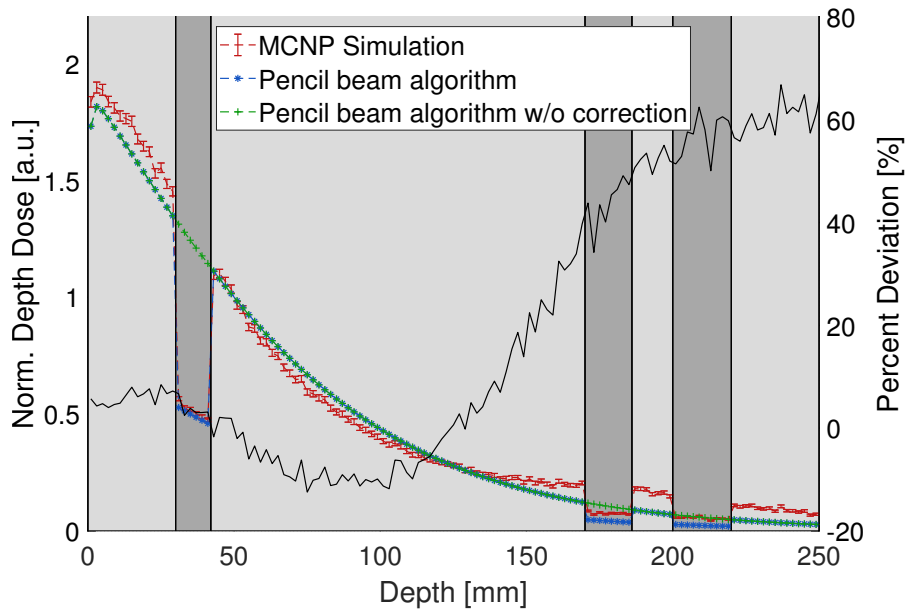
Figure 4.9: Comparison of depth dose curves in heterogeneous slab phantom for a field size of 6×6 cm^2. Results from Monte Carlo simulations are given in red. Results from pencil beam calculations are given in blue and green with and without KERMA corrections, respectively. Soft tissue is indicated by light grey and bone by dark grey.
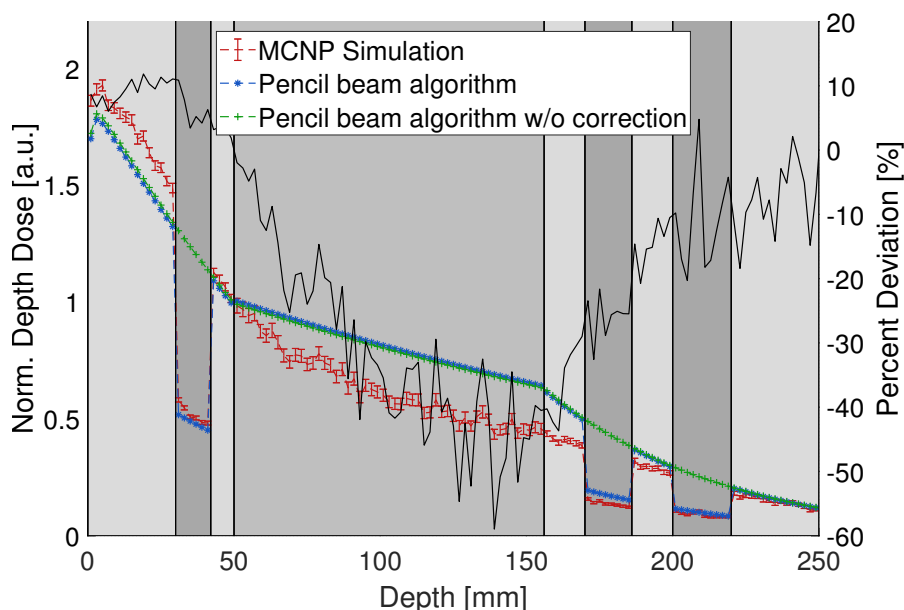
Figure 4.10: Comparison of depth dose curves in heterogeneous slab phantom with additional lung slab for a field size of 6×6 cm^2. Results from Monte Carlo simulations are given in red. Results from pencil beam calculations are given in blue and green, respectively, with and without KERMA corrections. Soft tissue is indicated by light grey, bone by dark grey, and lung by intermediate grey.

In figures 4.9 and 4.10 neutron depth dose curves for heterogeneous media are shown. The depth dose curves were calculated for slab geometries where the homogeneous water phantom was replaced by layers of different materials. The outer dimensions of the phantom were kept unchanged. For the geometry shown in figure 4.9, alternating slabs of soft tissue and bone were defined and are respectively indicated by light and dark grey. Boundaries between the materials are indicated as black vertical lines. For the geometry shown figure 4.10, an additional layer of lung tissue with a thickness of 10.6 cm was inserted as fourth layer. This layer is indicated in an intermediate grey. This last configuration of layers is defined to be comparable to the phantom used by Söderberg et al. [63] for the evaluation of correction factors. For both geometries, plotted results from MC calculations are given in red with errorbars. Results from the PB algorithm with radiologial pathlength correction applied are plotted in green. The blue curve indicates results from the PB approach where both corrections for neutron attenuation and dose-to-tissue conversion with KERMA factors are applied. Again, percentage deviations are indicated by the black solid curve. The differences between the MC and the PB calculation with all corrections applied are plotted. As discussed above, MC calculations are expected to give most accurate results and are therefore used as reference.

As shown in figure 4.9, the results from the PB calculations in heterogeneous

compositions of soft tissue and bone can be highly improved by the application of both correction procedures. Nonetheless, high deviations of $10 - 20\,\%$ from the MC reference calculation are reported for the first $15\,\text{cm}$. Even higher deviations are present for larger depths. In addition to the effect of the simulation input discussed above, the depth-dependent spectral neutron fluence also influences the performance of the correction factors.

For the lung slab shown in figure 4.10, large deviations are reported. The dose deposition in lung tissue is overestimated by the PB algorithm by up to $35\,\%$. Here, the normalization point in $5\,\text{cm}$ depth is located in the transition region between soft tissue and lung. For lung tissue, no significant improvement can be achieved by the application of the dose correction factors. The high deviations in the lung slab are most likely due to an overestimation of the scatter component by the pencil beam approach. The large mean free path in lung tissue of $r_l \approx 15.64\,\text{cm}$ can only be accounted for by corrections for the radiological path length on the central beam axis. Therefore, the scatter contribution remains uncorrected for in the PB algorithm so that it is expected to be overestimated. In contrast to the PB approach, MC methods can directly account for scattering effects towards the central beam axis and are therefore expected to give better results in material with large mean free path lengths.

Retrospective Dose Calculation on CT Data using Pencil Beam Kernels

As an example for a retrospective dose calculation, the *calculated dose deposition on a planning CT of an actual FNT treatment* will be discussed in the following. The head and neck treatment was performed at FRM II in 2012 as a neutron boost where four times $1.5\,\text{Gy}$ were applied. The patient suffered from an adenocystic carcinoma in the submandibular gland with beginning infiltration of the surrounding tissue. For the beam delivery, the patient's axis was oriented perpendicular to the beam axis and the radiation field was applied from the right. While a plan adaptation was done after three fractions, the following calculations are limited to the MLC shape used for the first three fractions. Leaf opening for the central four leafs in the upper leaf bank from left to right were $22\,\text{mm}$, $28\,\text{mm}$, $28\,\text{mm}$, and $18\,\text{mm}$. The central four leafs in the lower leaf bank - again from left to right - were $20\,\text{mm}$, $30\,\text{mm}$, $30\,\text{mm}$, and $26\,\text{mm}$. An irradiation time of $105\,\text{sec}$ was set in 2012 and the wall-to-patient-distance was $40\,\text{cm}$. Unfortunately for the retrospective evaluation, the wall-to-surface-distance differs significantly from the $100\,\text{cm}$ used for both the dosimetric characterization of MLC 1 and the generation of the pencil beam kernels. Dose calculations with the generated pencil beam kernels are therefore only reasonable for a wall-to-patient-distance of approximately $100\,\text{cm}$.

The isocenter in matRad was set to a point in $2.25\,\text{cm}$ within the patient so that the field size for the retrospective calculation was determined for a reference position $102.25\,\text{cm}$ away from the reactor wall. The distance between the reactor wall and the patient surface in the present example is therefore $100\,\text{cm}$. From the area generated by the MLC leaf opening, an equivalent field size of $r_{eq,1} \approx 31\,\text{mm}$ was calculated. The

output factors or dose rates were then extrapolated to be $OF_{n,1} \approx 0.20\,\text{Gy}/\text{min}$ and $OF_{\gamma,1} \approx 0.12\,\text{Gy}/\text{min}$ in 5 cm depth in water. For the actual dose calculation using the extrapolated OFs, a reference depth of 5.26 cm within the patient was calculated for neutrons using the correction factor for the radiological depth in soft tissue. Since in this work no effort was made to gain a HU lookup table for the CT scanner used in 2012, the radiological depth for gammas was approximated by the geometrical depth. Therefore, the dose deposition of the gamma component was calculated in reference to 5 cm geometrical depth in the patient. This is reasonable since the beam passes only soft tissue on the central beam axis. For the calculation of the gamma dose deposition, the matRad standard lookup table for HU was used.

Figures 4.11 and 4.12 show the resulting dose calculated in matRad using the pencil beam kernels for both beam components in axial and coronal view, respectively. For all dose visualizations in figures 4.11 and 4.12 and in the following, isodose lines are set to 0.25 Gy, 0.5 Gy, 0.75 Gy, 1 Gy, 1.25 Gy, and 1.5 Gy with colors indicated by the colorbar. In figures 4.11b and 4.12b an additional line was included for isodoses of 0.125 Gy for visualization purposes. The planning target volume (PTV) and the submandibular gland are contoured in light green and light yellow, respectively. The isocenter is indicated as a black cross. Further organs and tissues like bone, the mandibular, brain stem, and larynx are contoured in grey, off-white, orange, and green.

The effect of the correction factors on the neutron dose is clearly visible in figures 4.11a and 4.12a in the regions where bone tissue is contoured. Furthermore, the steeper gradient of the neutron dose in comparison to the gamma dose deposition can be seen by comparing figures 4.11a and 4.12a respectively with figures 4.11b and 4.12b. Also, only for gamma radiation a build-up region is present while the exponential decrease of the neutron dose deposition begins close to the patient surface.

The summed dose of both beam components from above is given in axial and coronal view in figures 4.13a and 4.14a. It can be seen from both images that the 0.5 Gy isodose line reaches far beyond the PTV in distal beam direction. As a result, the part of the larynx shown in figure 4.13a is covered by the 0.5 Gy isodose line.

For demonstration purposes of the CT-based planning and optimization approach for MEDAPP, a simple *plan modification* was done. A visual inspection of the dose distribution especially in figure 4.12a suggests to move the isocenter in matRad or - in more general terms for MEDAPP - the central beam axis in cranial direction and to add an additional field. Therefore, the isocenter was moved by one leaf width of 15 mm in cranial direction so that for the modified plan three leafs to the left and only one leaf to the right were opened in both the upper and lower leaf bank. The field shape was chosen to be identical with the original treatment field. For plan optimization, an additional field with only the two central upper and lower leafs opened was defined. These four leafs were opened by the same amount like in the main field. For the additional field, an equivalent field size of $r_{eq,2} \approx 22\,\text{mm}$ was calculated. The extrapolated OFs were calculated to be $OF_{n,2} \approx 0.14\,\text{Gy}/\text{min}$ and
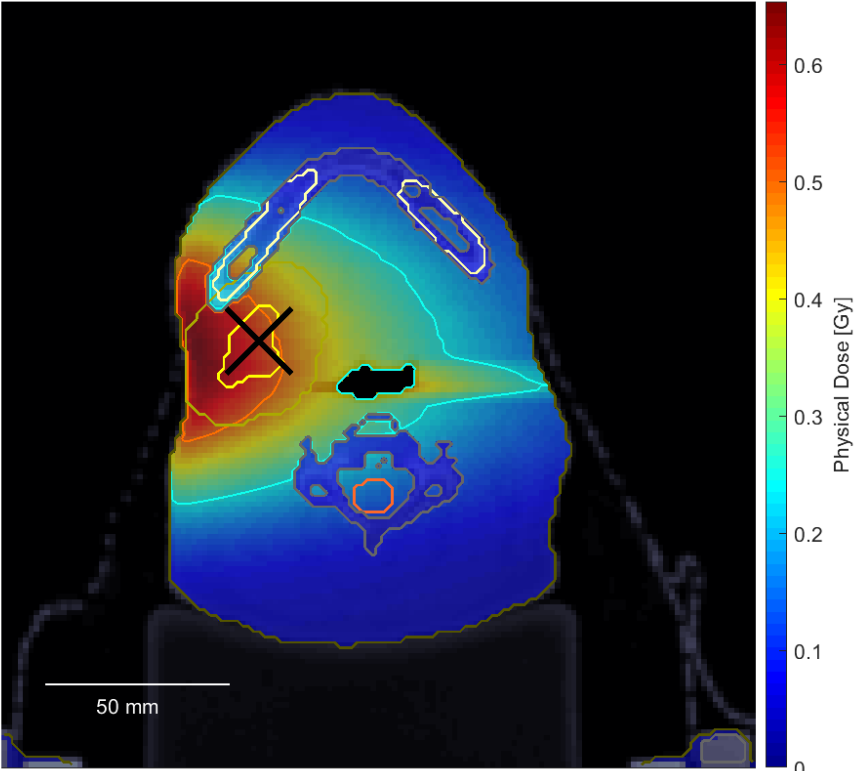
(a)
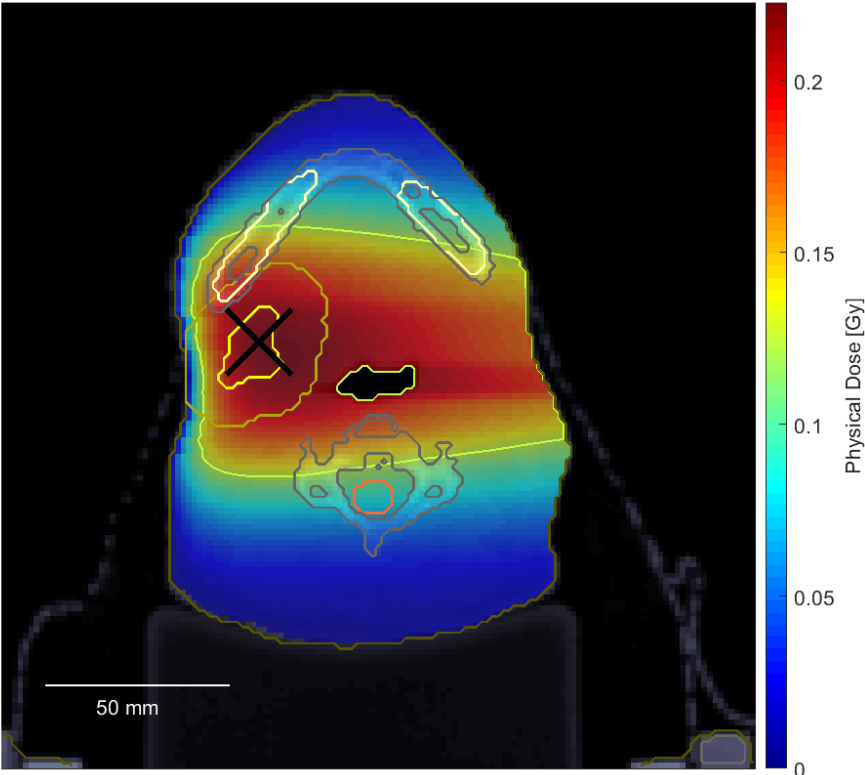
(b)

Figure 4.11: Dose calculated in matRad using PBKs for (a) the neutron and (b) the gamma component in axial view, matRad isocenter as black cross.
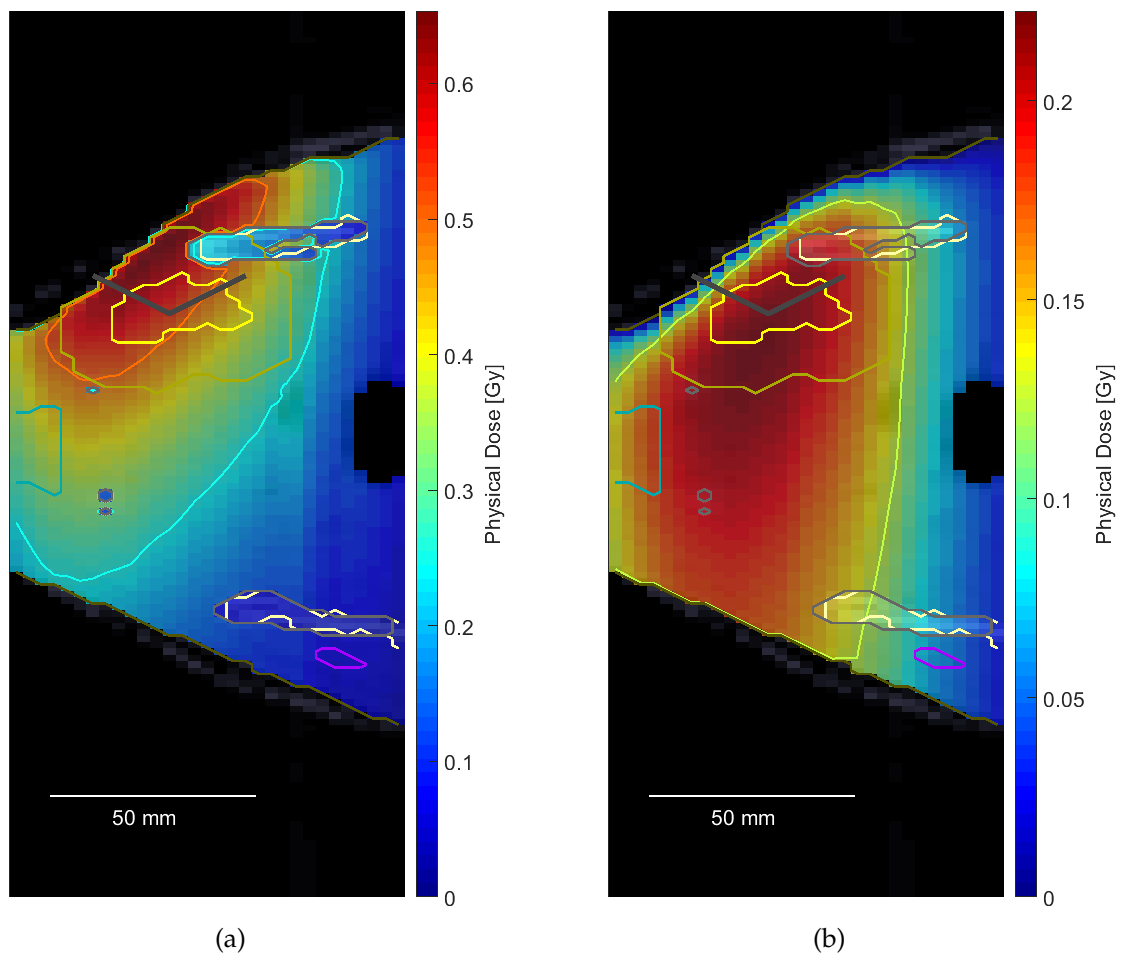
Figure 4.12: Dose calculated on CT data in matRad using PBKs for (a) the neutron and (b) the gamma component in coronal view.
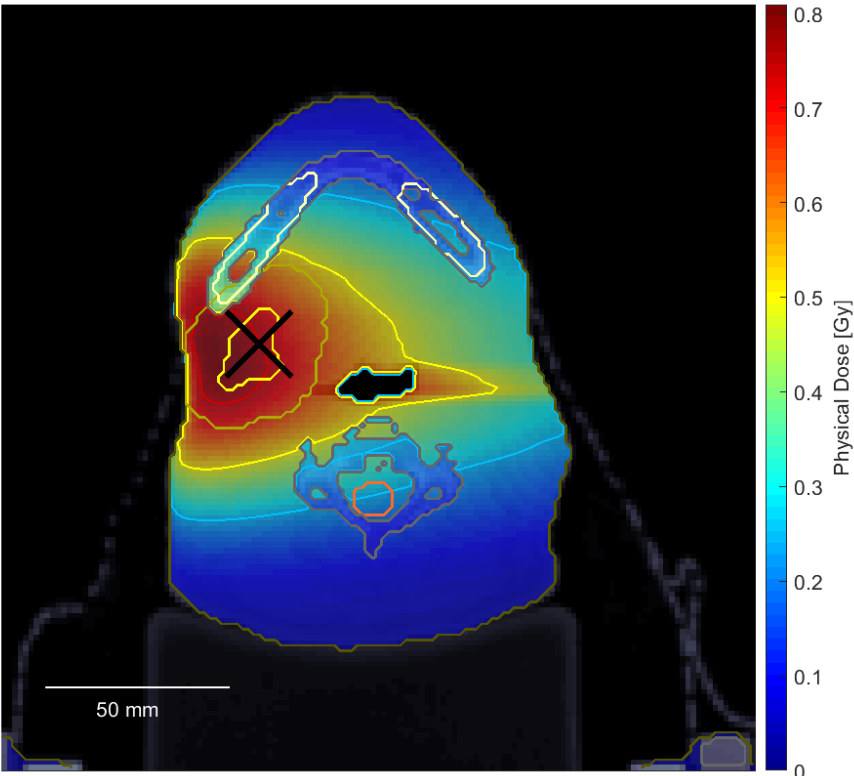
(a)
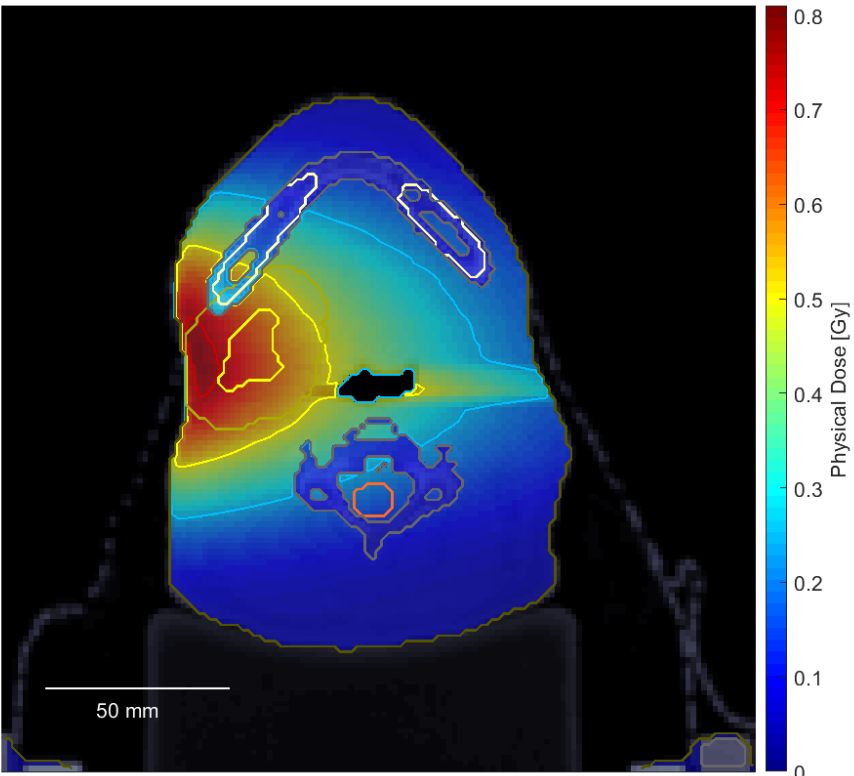
(b)

Figure 4.13: Axial view of summed neutron and gamma dose calculated using PBKs for (a) retrospective dose calculation and (b) plan modification.
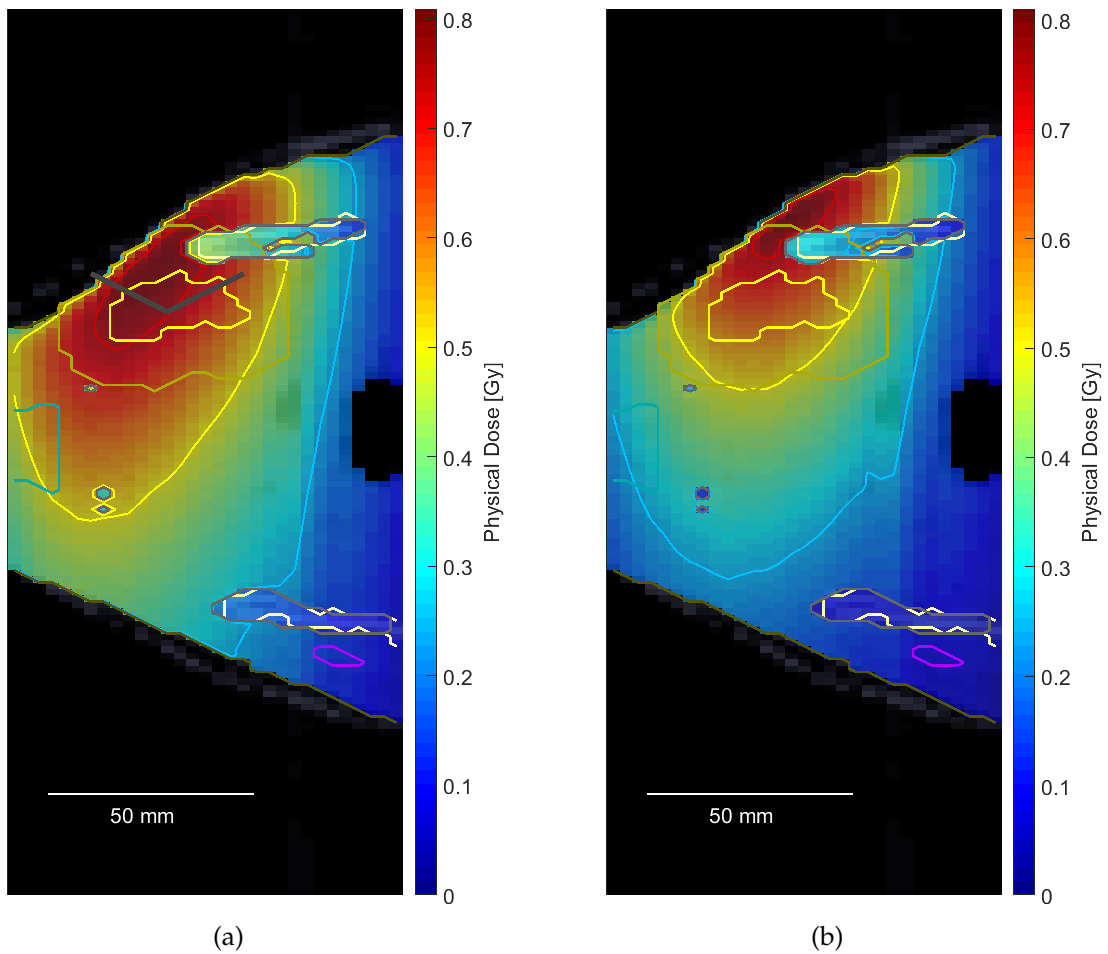
Figure 4.14: Coronal view of summed neutron and gamma dose calculated using PBKs for (a) retrospective dose calculation and (b) plan modification.

$OF_{\gamma,2} \approx 0.08\,\text{Gy/min}$. The reference depth for neutrons after isocenter modification was not significantly altered even though four voxels of bone tissue are now located between the patient surface and the reference position along the central beam axis. This is due to the previously discussed small difference in the mean free path of neutrons in soft tissue and bone.

From running the pencil beam calculation for both field shapes, a dose influence matrix D_{ij} with two columns - one for each field - was obtained. D_{ij}-values were saved as dose rate in Gy per sec. In the next step, the matRad inverse optimization function was run with the objective to achieve the same maximum dose value as in the first scenario. Field weights were obtained to be $w_1 = 34.7$ for the main field and $w_2 = 37.1$ for the additional field. Since the dose influence matrix is saved as dose rate, the weights can be interpreted to carry the unit seconds. The result of the re-planning is given in figures 4.13b and 4.14b. While matRad of course offers different optimization approaches than the maximum dose value, it was decided to optimize the modified plan to have the same maximum dose as the original plan. This makes the qualitative comparison as given in figures 4.11 and 4.12 easily accessible. Besides, the purpose of the plan modification was not an actual retrospective optimization but a demonstration of the now available abilities for 3D planning with pencil beam kernels for the mixed neutron-gamma radiation field in matRad. A qualitative comparison of figures 4.13a and 4.14a respectively with figures 4.13b and 4.14b shows that the extension of the $0.5\,\text{Gy}$ isodose line is reduced for the modified plan. Nevertheless, the PTV coverage is also reduced.

In order to make the dose calculations performed in matRad also available for further evaluation outside of matRad in a clinical dose evaluation software, the export function of matRad was used to export both the CT data and the calculated dose cubes into nrrd file format. Nrrd is an acronym for nearly raw raster data and is used for example for the exchange between treatment planning systems. The nrrd-files were passed on to the medical physics unit of the radiation oncology department and could there be loaded into the Eclipse treatment planning software provided by Varian. While dose volume histograms are also available in matRad, a more convenient comparison of the dose distributions generated by one field and the modified scenarios with two fields is possible in Eclipse. To give the reader an impression of the plan evaluation abilities, the comparison in Eclipse is shown in figure 4.15. Here, the original plan is shown on the left and the modification is visualized on the right. In the DVH, dose values for the PTV and OARs can be inspected. For example, the red lines indicate the dose to the PTV and the blue and turquoise, respectively, indicate the dose to the submandibular gland and the larynx. Triangular markers indicate the original plan and square markers the modified one.

Generation of Pencil Beam Kernels for the MLC 3

In parallel to the decomposition of pencil beam kernels for MLC 1, kernels were also generated for MLC 3. A comparison of the dosimetric characteristics of the MLC
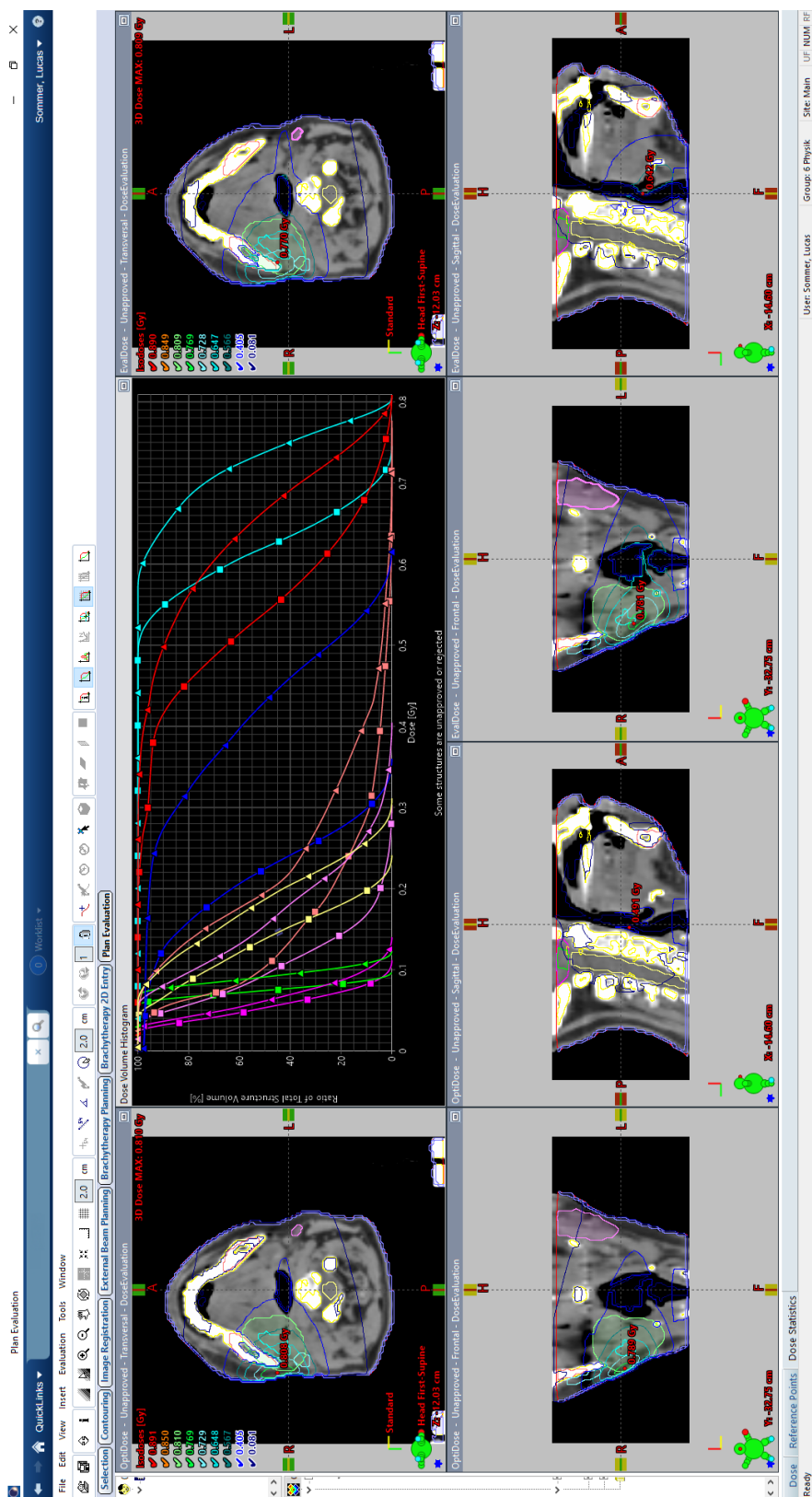
Figure 4.15: Plan visualization in Eclipse for the original and the modified scenario.

(a)   (b)
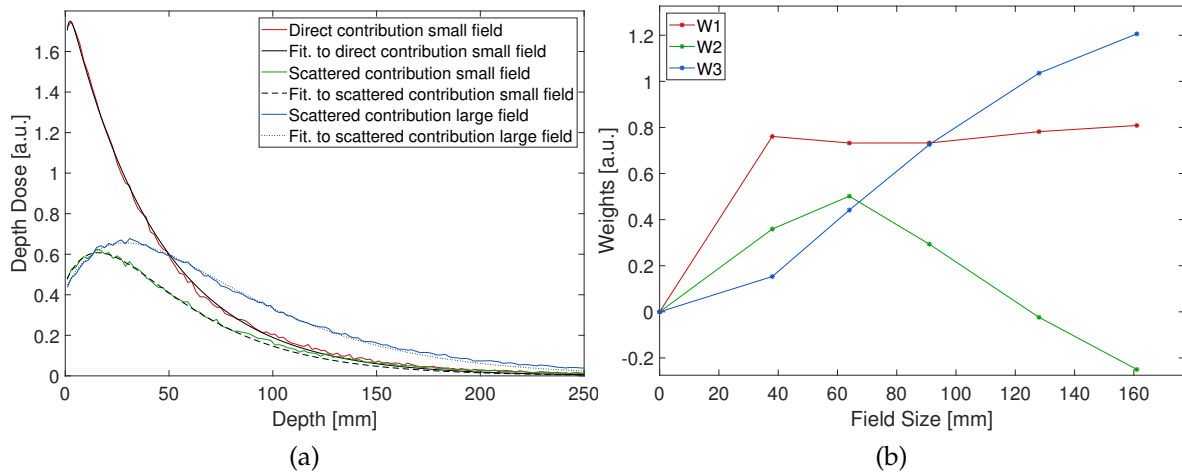
Figure 4.16: Pencil beam kernels for neutron component of MLC 3: (a) Analytical fits to simulated data for direct and scattered contribution for primary neutrons. (b) Fitted weights for direct and scattered components to simulated dose for different field sizes.

versions was already provided in chapter 3. Here, the depth dose characteristics of MEDAPP were shown to remain rather unchanged after the implementation of the new MLC. Nevertheless, the different field sizes for MLC 3 and the changed distance between MLC exit and reference position made it necessary to generate a different set of PBKs for MLC 3. During the dosimetric characterization of the new MLC, the Mg-IC was replaced by a modified chamber with a wall electrode made from aluminum and a central electrode made of plastic which is not in agreement with the recommendations in [19]. Output factors for all square field sizes were only measured with the Al-IC so that these measurements had to be used for the generation of PBKs. Calibration measurements in 2018 were also performed for this Al-IC (cf. chapter 3). Depth dose curves and beam profiles for side lengths 82 mm and 116 mm were again measured with the Mg-IC from above and could be used for the evaluation of the PBKs.

In figure 4.16, the analytical fits to simulated data and the weights for the three components in the decomposition are shown for the neutron component of the beam for MLC 3. While PBKs were also generated for the gamma component, they differ only slightly from the ones for MLC 1 and are therefore not discussed. The components of the small and the large fields used for the decomposition are shown in figure 4.16a. Side lengths of the square fields at the MLC exit are 34 mm and 146 mm for the small and the large field, respectively. Depth dose curves were again normalized to 5 cm depth. The mean and maximum relative error for neutron and gamma heating calculated for all available field sizes were below 4 % and below 11 %, respectively. Again, higher relative errors had to be accepted for the secondary charged particle heating.

It can be seen from figure 4.16a that the direct contribution to the central axis dose for the small field remains dominant up to a depth of about 13 cm. For larger depths, the direct and the scatter contribution are approximately identical. As expected, the build-up effect for the direct contribution is small while it is more pronounced for the scatter contribution of both the small and the large field. The fitting parameters μ for equation 4.3 was obtained to be $\mu_{fit} = 0.0231 \, \text{mm}^{-1}$. The β-values were fitted to be $\beta_{1,1} = 14.8900 \, \text{mm}^{-1}$, $\beta_{1,2} = 9.5970 \, \text{mm}^{-1}$, $\beta_{1,3} = 0.2731 \, \text{mm}^{-1}$, and $\beta_{1,4} = 0.8135 \, \text{mm}^{-1}$ for the direct component of the small field, $\beta_{2,1} = 0.0332 \, \text{mm}^{-1}$, $\beta_{2,2} = 0.0545 \, \text{mm}^{-1}$, $\beta_{2,3} = 2.0380 \, \text{mm}^{-1}$, and $\beta_{2,4} = 4.4500 \, \text{mm}^{-1}$ for the scattered component of the small field, and $\beta_{3,1} = 4.5730 \, \text{mm}^{-1}$, $\beta_{3,2} = 10.6700 \, \text{mm}^{-1}$, $\beta_{3,3} = 0.0294 \, \text{mm}^{-1}$, and $\beta_{3,4} = 0.0233 \, \text{mm}^{-1}$ for the scattered component of the large field. The sums of squared residuals for the respective fits were obtained to be 0.430, 0.025, and 0.067.

As shown in figure 4.16b, the weights for the direct contribution in the decomposition are approximately constant at about 0.75 to 0.8. They dominate for three out of five discrete field sizes used for the decomposition and are exceeded by the weight for the scatter contribution of the large field at an equivalent field size radius of $r_{eq} \approx 90 \, \text{mm}$. For the largest field size, weights for the scatter contribution of the large field exceed the weights for the direct contribution of the small field by a factor of about 1.5. For MLC 1, this ratio was about 2. Furthermore, the absolute values of the negative value for the weight of the scatter contribution of the small field is about 17 % of the value for the large field. For MLC 1, the compensation of the large field scatter by the small field scatter weight was 7 %.

Figures 4.17 and 4.18 show comparisons of the neutron depth dose curves calculated with the pencil beam algorithm (purple) in reference to the MC calculations (blue) for square fields of side length 82 mm and 116 mm, respectively. Measured DDCs are shown in blue starting at a depth of 3 cm. For both field sizes, simulated data could be reproduced within $\pm 5 \%$ up to a depth of $10 - 12$ cm. Large deviations up to 35 % are reported for larger depths. Also deviations between the MC data and the measured curves are visible. Like for MLC 1, the slope of the measured curves is steeper than that for the simulated curves.

Figures 4.19 and 4.20 show the horizontal beam profiles in 5 cm depth for square fields of side lengths 82 mm and 116 mm, respectively. The color coding is identical to the one in figures 4.17 and 4.18. For both field sizes, an adequate reproduction of measured and simulated data by the pencil beam algorithm in the dose region of about 30 % to 75 % of the central axis dose is reported. While the PB algorithm overestimates the lateral dose below 30 %, the degree of discrepancy is smaller than for MLC 1. Above 75 % of the central axis dose, all three curves show good agreement for field size 82 mm but for field size 116 mm differences are reported between the simulated data on the one side and measured data and data from the PB algorithm on the other side.
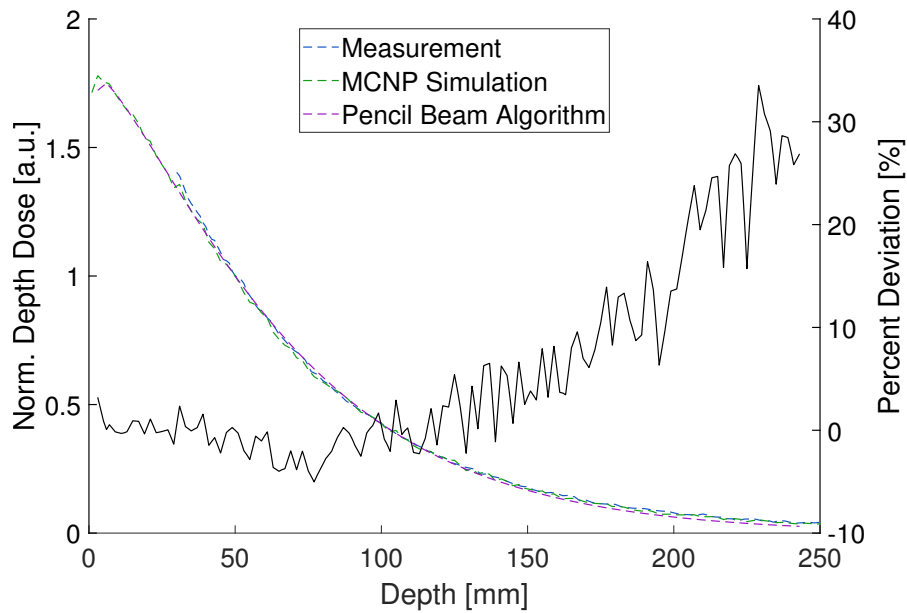
Figure 4.17: Comparison of measured depth dose curve (blue) and calculated ones using MCNP (green) and pencil beam kernels (purple) for **neutron** component and field size 82×82 mm^2.
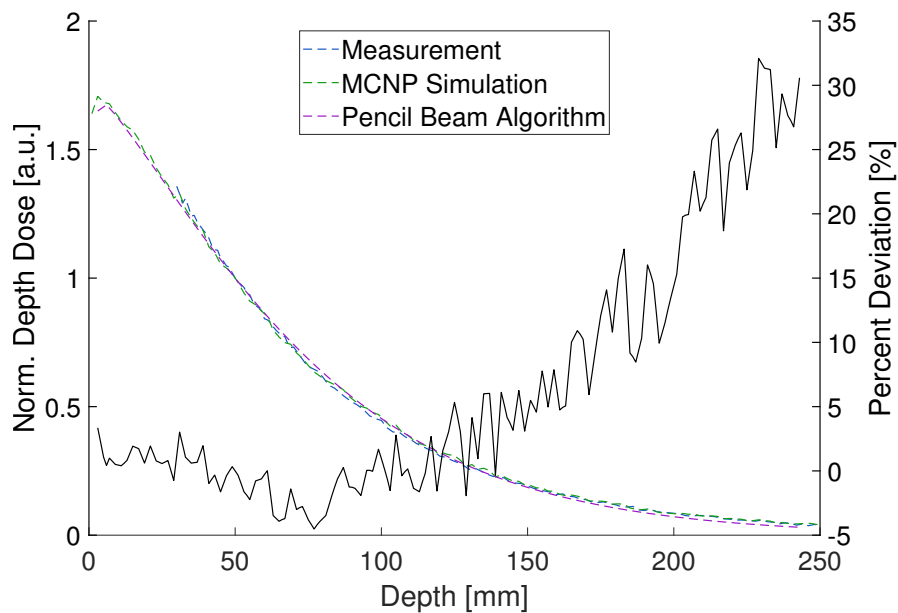
Figure 4.18: Comparison of measured depth dose curve (blue) and calculated ones using MCNP (green) and pencil beam kernels (purple) for **neutron** component and field size 116×116 mm^2.
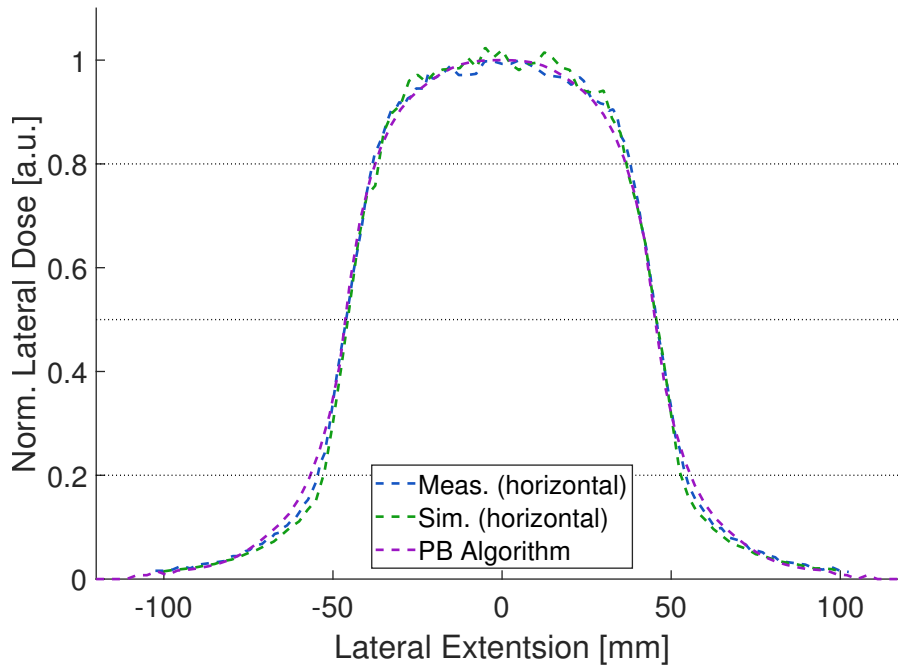
Figure 4.19: Horizontal beam profile comparison for measured (blue) and calculated data using MCNP (green) and pencil beam algorithm (purple) for **neutron** component and field size 82×82 mm^2 in 5 cm depth.
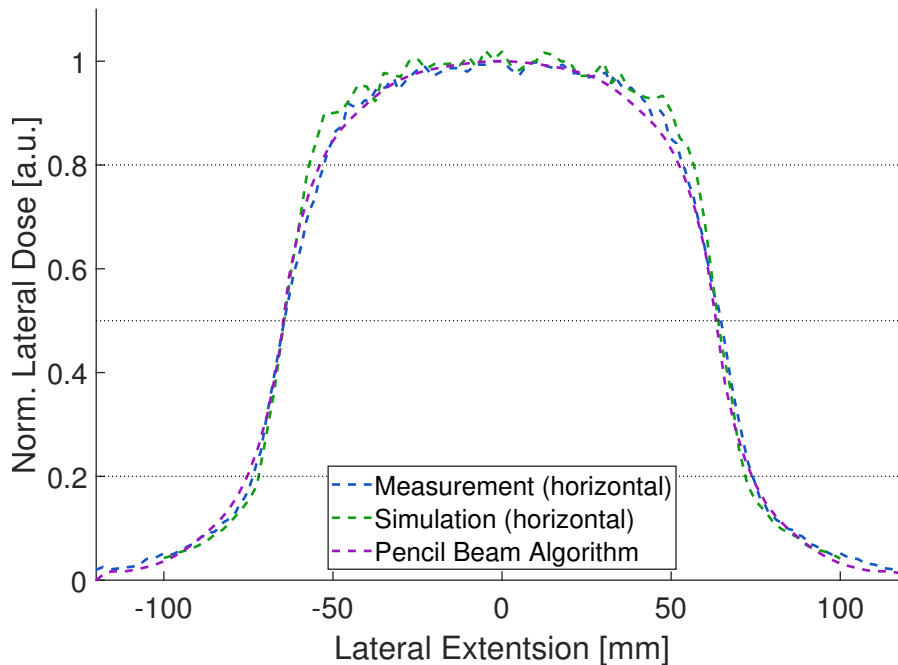
Figure 4.20: Horizontal beam profile comparison for measured (blue) and calculated data using MCNP (green) and pencil beam algorithm (purple) for **neutron** component and field size 116×116 mm^2 in 5 cm depth.

4.1.3 Discussion

The generated pencil beam kernels for the mixed neutron-gamma field allow a separate and time-efficient reproduction of depth dose curves from Monte Carlo simulations for both beam components in water. For the neutron dose deposition, agreement within $5 - 10$ % for the first $12 - 15$ cm depth in water were demonstrated. Depending on the field size, this depth comprises the $80 - 90$ % dose fall-off region. As shown for MLC 1, dose calculations for heterogeneous slab phantoms could be highly improved by the application of tissue-dependent correction factors. While the performance in the two material slab phantom of soft tissue and bone shows promising results for the application in head and neck treatment scenarios, dose to lung is highly overestimated by the pencil beam approach. Nonetheless, an overestimation of lung dose might be of minor importance in the application for example in chest wall recurrence irradiations.

A comparison of the performance of the PBKs for neutrons for the two MLC versions shows differences in the ability to reproduce lateral beam profiles. While in general a difference in the beam profiles is due to the different geometry and reference positions of the two MLCs, the difference in the field sizes used as small field for the decomposition of PBKs for MLC 1 and MLC 3 might have a non-negligible effect. But since for MLC 1 the field size in clinical applications was limited to a minimum field size of 6×6 cm^2, it was decided to use this field as reference for the PBK generation.

4.2 Dose Calculation using Monte Carlo Methods

While the general good performance of MCNP in dose calculations in water was already shown in comparison to measurements in section 4.1, the following section on Monte Carlo simulations for dose deposition will expand this approach to heterogeneous patient geometries.

4.2.1 Methods

For the discussion of the implementation of the Monte Carlo dose engine, it is instructive to simply follow the logical order in which functions of the implementation are executed in the dose calculation process. Therefore, the extraction of tissue information from CT data will be discussed first. Second, the way to set up the geometry for particle transport in MCNP will be addressed. The used tallies and the parameters to adequately account for the physics discussed in chapter 2 will also be presented. Furthermore, the definition of the radiation source and the outcome of the actual MCNP simulation will be discussed.

Segmentation and Post-Processing

In order to simulate radiation transport using MCNP, information on the transport medium needs to be available. As discussed above, using planning CT data is the

first choice for the application of the PB algorithms for primary gammas and was also used for dose calculation applying neutron PBKs. Since methods to gain voxel-based tissue information for MC simulations are well established (cf. [18] & [58]), this method could easily be applied here and will be discussed in the following. Two additional reasons to use CT imaging for both PB calculations and MC simulations can be identified. First, using the same imaging data for both dose calculation approaches facilitates the workflow. Second and more importantly, it is more likely that for retrospective dose calculations for MEDAPP at least a planning CT scan is available.

Air, soft tissue, lung tissue, cortical bone, and skin tissue are defined for radiation transport calculations. The elemental composition of the different types of human tissue as tabulated for adults in ICRU report 46 [30] was used. A detailed list of the weight-% of the different elemental composition including the composition of air can be found in table 4.1. For air, the elemental composition was defined according to the material tables provided by NIST [47]. Here, carbon was neglected due to its low fraction by weight of less then one per mill.

On a voxel-basis, patient CT data is segmented into air, lung, soft tissue, and bone by using Hounsfield-Unit-intervals. The segmentation using HU was adopted from the discussion by Schneider et al. [59] and DeMarco et al. [18]. The HU-intervals actually used in this work are summarized in table 4.2. An approach to calculate material density from CT data was also presented by Schneider et al. [58] and a MATLAB function provided by Treeby and Cox [73] applying this method is used here.

After the segmentation according to HU-intervals is done, post-processing is performed in order to reassign voxels falsely categorized as lung tissue to assign them either to air or soft tissue. A false classification can for example happen in transition regions between air cavities and the body where Hounsfield Units can potentially be quantified in the lung interval. In cases where the lung is visible and contoured on the CT data, all other false lung voxels are reassigned by a nearest-neighbour-approach to air or soft tissue. In cases where the lung is visible but not pre-segmented, a simple auto-segmentation is applied by searching for the largest coherent voxel accumulation of lung tissue from the segmentation using HU-intervals. Here, using a pre-defined lung contour is favourable. Furthermore, a skin layer of default thickness of 1 mm is fitted around the patient. Besides the PTV contour, the body is the only other contour

Table 4.1: Elemental tissue composition in weight-% used for MC simulations.

	H	C	N	O	Na	P	S	Cl	Ar	K	Ca
Soft tissue	10.1	11.1	2.6	76.2	-	-	-	-	-	-	-
Lung	10.3	10.4	3.1	74.9	0.2	0.2	0.3	0.3	-	0.2	-
Bone	3.4	15.5	4.2	43.5	-	10.3	-	-	-	-	22.5
Skin	10.0	20.4	4.2	64.5	0.2	0.1	0.2	0.3	-	0.1	-
Air	-	-	75.5	23.2	-	-	-	-	1.3	-	-

compulsory for the MC dose engine to run. This is due to the fact that the body contour is extended within the patient and the voxels in the layer generated by this procedure are assigned to skin tissue. Again, a nearest-neighbour-approach is used for the extension of the hull.

As a result, information on the material and the density for every voxel in the image data set is available for the definition of the simulation volume.

As an addition to the tissue segmentation for FNT, an option to define a PTV for BNCT was also implemented. In cases where a contour named *PTV_BNCT* is defined in the data set, the voxels associated to this particular contour will be re-defined to contain soft tissue with a pre-selected ^{10}B-concentration. While currently only one contour can be defined to contain ^{10}B, the option to define more volumes of interest with individual ^{10}B-concentrations could easily be added.

Table 4.2: Hounsfield-Unit-intervals for tissue segmentation of CT data.

Material	Air	Lung Tissue	Soft Tissue	Bone
HU values	-1000 to -950	-950 to -170	-170 to 280	280 to 4000

Simulation Geometry

For the simulation of particle transport, the main simulation volume in MCNP is subdivided into cuboids corresponding to the voxels from the planning CT. The *lattice option* from MCNP is used to set up the geometry and fill every cuboid/voxel with the associated material from the segmentation discussed above. For filling the voxels, MCNP provides *material universes* where every universe is defined to contain one material type as defined in table 4.1. Even though the density is calculated for each voxel individually, all voxels of one specific universe are filled with the mean density of that particular material calculated from the respective set of material voxels.

Surrounding the whole voxel geometry, an additional air layer of thickness $d_{layer} = 150$ cm is added for source positioning outside the CT volume. Particles crossing the outer surface of that outer layer are deleted from the transport calculation and no back-scattering is considered.

Typical voxel dimensions are $1 - 3$ mm in lateral and $3 - 5$ mm in axial direction. matRad also provides an option to resize the CT data and the associated contouring information to other voxel sizes than the ones read from DICOM files. For variance reduction, the *cell importance* function of MCNP is implemented and the user is provided with the option to select material-specific values for the importance. A simple way to look at MCNP's importance function is that every particle travelling from one voxel to another is duplicated by the ratio of the importance values associated to the respective voxels. Even though MCNP provided much more sophisticated variance reduction techniques, their implementation was not pursued since their execution also needs supervision by the user. While this is of course possible, the

ability to run dose calculations without profound MCNP knowledge was envisaged in this work.

Tally Set-up

For the purpose of dose calculation, two different options for tally definition in the MCNP simulation were implemented. Which option to choose depends on the needed accuracy of the dose calculation and the application in general. The first option is to use KERMA-factors as energy-dependent multipliers for a fluence tally. Here, a FMESH4-tally is used which is an analog to an F4-tally but on a mesh geometry. Using the mesh geometry, one tally is located in each voxel so that KERMA values can be recorded for every voxel individually. KERMA-factors are saved as text file in the repository of the dose engine and can be modified if necessary. The KERMA-factors used for neutrons and photons were taken from ICRU report 46 [30]. They were not calculated by the elemental composition of the tissue types but rather taken as tabulated for the tissues of interest. Air-KERMA was set to zero both outside the patient contour and inside body cavities.

The second option is to tally total dose deposition by a TMESH-type-3-tally which is equivalent to a +F6-tally but again defined on a mesh geometry. Dose deposition is recorded for every voxel individually. In the following, the two options will be referred to as *KERMA option* and *total dose option*.

Interaction Physics

MCNP's abilities to accurately simulate the interaction processes governing the propagation of both primary and secondary particles was already discussed in chapter 2. Depending on the selected tally option from above, either only a subset of these abilities is used or the code's abilities are widely exploited to model the propagation of primary neutrons and gammas and also of charged and neutral secondary particles. In general, the selection of an adequate subset of interactions to be modelled can be seen as a trade-off between simulation accuracy and simulation speed.

In order to simply tally neutron and photon KERMA, secondary particle transport is switched off completely by running MCNP with *MODE N*, *MODE P* or a combined *MODE N P*. In MCNP, the user has to specify particles for tracking by the *MODE* keyword. Here, *N* and *P* indicate neutrons and photons, respectively. While electron transport is switched off then, Bremsstrahlung-contribution to the KERMA from secondary electrons is still included from the thick-target Bremsstrahlung approximation [79].

When an accurate total dose calculation is needed, all important particles have to be included by using *MODE N P E -E H D T S A #*. Electrons and positrons are respectively indicated by *E* and *-E*, protons by *H*, deuterium by *D*, tritium by *T*, ^{3}He by *S*, α-particles by *A*, and all heavier ions than α-particles by *#*. The default physics settings in MCNP indicated by the keyword *PHYS* were partly changed for neutrons,

photons, and ions. For neutrons in combination with the total dose tally option, the seventh entry associated to the *PHYS*-keyword was changed to one so that light-ion recoil is on. For simple KERMA calculations, the default options were used. For the total dose option, the photon physics is changed from default by setting the fourth entry to one so that implicit photonuclear particle production by for example (γ, n)-reactions is on. The photonuclear effect is neglected for simple KERMA calculations. For protons, the seventh entry was set to one and the sixteenth entry was set to minus one to switch on light-ion recoil and δ-ray production, respectively. For all other ions, δ-ray production was also turned on by changing the seventeenth entry to minus one.

In order to spare computational resources, it is advisory to use the energy cutoff function available in MCNP. The selection of the energy cutoff is governed by the range of the regarding particles in reference to the size of the used voxels. As stated above the minimum extension was set to 1 mm, which should therefore be the reference for the selected cutoff energy. For neutrons, the mean free path can be calculated from the macroscopic cross sections shown in figure 2.5. For a neutron energy of $E_n = 10\,\mu\text{eV}$ propagating through the materials discussed above, the mean free path has a maximum for lung tissue with a value of $R_{mfp,l} \approx 0.5\,\text{mm}$. Therefore the *neutron cutoff energy* is set to $E_{cut,n} = 10\,\mu\text{eV}$. Even though $E_n = 10\,\mu\text{eV}$ is well below the ionization potential of for example water - which is 75 eV [47] - neutrons can propagate with low energies through the material and will eventually undergo a capture reaction. The neutron cutoff energy from above was selected in order to account for the path traveled by the neutron before undergoing a (n, γ)-reaction. For the *photon cutoff energy*, $E_{cut,\gamma} = 3\,\text{keV}$ was used. According to mass attenuation coefficients provided by NIST [48], the mean free path in water and lung tissue of photons with an energy of 3 keV is below 0.5 mm. *Electron cutoff energies* were set to $E_{cut,e} = 50\,\text{keV}$. For electrons with this energy, a CSDA range in water of $R_{CSDA} \approx 40\,\mu\text{m}$ is given in the ESTAR data tables [7] so that electron transport down to 50 keV is for sure adequate for a voxel extension of 1 mm. According to ICRU report 26 [28, p. 15], the maximum ranges of the most abundant ions for neutron energies below 20 MeV are below the ranges of recoil protons. This holds true also for α-particles from nuclear $^{16}O(n, \alpha)^{13}C$-reactions for which the α-particles' energy is maximized beyond the possible nuclear reactions in the considered energy range. For a neutron energy of $E_n = 20\,\text{MeV}$, the maximum range of recoil protons in turn with $E_p = 20\,\text{MeV}$ is $R_{max} = 0.5\,\text{mm}$. *Proton and ion cutoff energies* were set $E_{cut,p} = 1\,\text{MeV}$ and $E_{cut,ions} = 1\,\text{MeV}$, respectively, so that their ranges are well below the used voxel dimensions.

Within the simulation volume, temperatures for the free-gas approximation were set to 20 °C for voxels containing air and to 36 °C for all voxels containing tissue material.

Definition of Neutron and Gamma Source

For the purpose of treatment planning with an external particle source, a surface source can be defined in MCNP. Depending on the intended use in dose calculation or the step in treatment planning, two different options were implemented for the
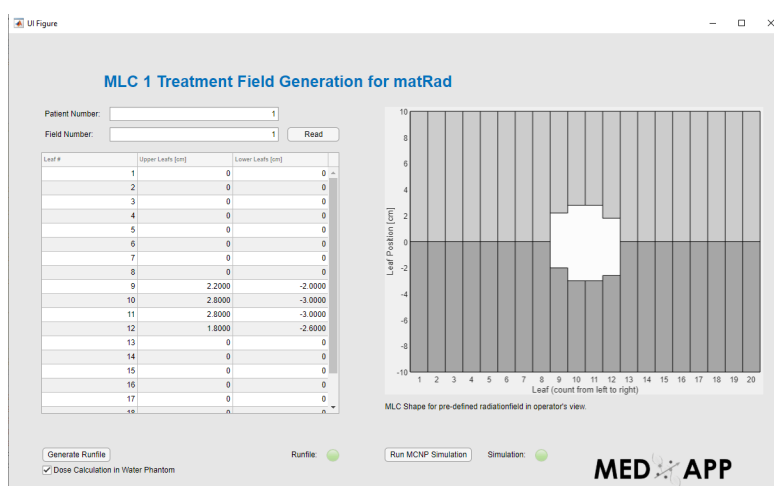
Figure 4.21: MATLAB app to control treatment field shape of MLC 1 and run MCNP simulation for the generation of a surface source as input for dose calculation.

user to select. One option (A) is the simple definition of a square area source where neutrons and/or gammas start with a mono-directional velocity vector distribution parallel to the beam axis. The extension of this square can either be specified as one of the square fields given by the version of the MLC or as the bixel size of the particular MLC. The spectral information for neutrons and gammas is taken from Breitkreutz et al. [11] and Jungwirth et al. [34], respectively. These primary neutron and gamma spectra are saved as text-files in the MCNP dose engine's repository and can easily be modified in case improved spectral information becomes available.

For option (B), energy and direction information of the primary irradiation field are read from a MCNP-specific *surface source file*. These files need to be generated by a previous MCNP run that includes a simplified geometry of the beamline and a pre-defined MLC shape. For the purpose of dose calculation for a given MLC-shape, a MATLAB application was implemented to read leaf information in tabulated format. As an example, the interface of the app is shown in figure 4.21 for the leaf configuration of the retrospective example for MLC 1 mentioned in section 4.1.2. An additional feature is the option to directly run the MCNP simulation with the water phantom from above included at the patient position. The dose distribution calculated in this MCNP run could potentially be used in a quality assurance or general validation process for the irregularly shaped treatment fields. However, the main application will be the generation of source files for the retrospective calculation of dose depositions on CT data.

Due to MEDAPP's geometry, the positioning of the source is limited to the horizontal plane around the patient. Therefore, the gantry angles in matRad has to be fixed at 90° or 270°. The patient couch can be rotated by 360° for dose calculation for the fixed beamline.

Calculated Dose Deposition and Tally Statistics

The physical dose or KERMA values calculated by MCNP are saved for each voxel and field in the *dose influence matrix* D_{ij}. In cases where only one square field or one MLC shape was calculated, only one column exists in the dose influence matrix.

In general, *tally statistics* are provided in an output file by MCNP. For inspection within MATLAB, only the *mean, median, and maximum relative errors* for every contoured volume of interest in the CT data set are read from the MCNP output. The mean, median, and maximum are calculated from all voxels with non-zero dose values associated to a contour. It should be noted that in MCNP a relative error of 0 % is associated to a voxel with a zero tally value even if this value might be non-accurate.

Absolute Dose Calculation

As discussed by Breitkreutz [9], differences of 16 % for neutrons and up to 50 % for gammas between the measured and the simulated dose deposition in water were reported in the past. This issue was further addressed by Jungwirth et al. [34] and Garny et al. [22] for example by adjusting the gamma fluence rate in the simulation to reproduce measured absolute dose rates in water. For this work, correction factors were generated for both the neutron and the gamma dose deposition to reproduce measured data for a field size of 9×9 cm^2 in 5 cm depth in water. Measured data was again taken from [75] and initial fluence rates for neutrons and gammas free in air at patient position using MLC 1 were set to $\dot{\Phi}_n = 3.2 \times 10^8$ cm^{-2}s^{-1} and $\dot{\Phi}_\gamma = 2.9 \times 10^8$ cm^{-2}s^{-1}. While the neutron spectrum and fluence rate are well known and were taken from the measurements by Breitkreutz et al. [11] with an absolute error of 0.2×10^8 cm^{-2}s^{-1}, very different values for the gamma fluence rate between 2.8×10^8 cm^{-2}s^{-1} [22] and 3.7×10^8 cm^{-2}s^{-1} [34] are reported so that no meaningful error is available. In order to obtain absolute values for the dose rate in reference to the initial particle fluence rates, two simulations needed to be run. One without the water phantom in order to obtain the particle fluence free in air for the chosen number of source particles and one simulation with the water phantom in place to obtain dose values in reference to this particular particle fluence free in air.

4.2.2 Results

In the following section, the results of the MC approach for dose calculation using MCNP are presented. Results are given using the example of an actual treatment from section 4.1.2. First, calculated *correction factors* for MLC 1 for *absolute dose calculation* of the neutron and gamma component of the beam are given. Second, results of the *tissue segmentation* associated to the MC dose engine and the set-up of the *simulation geometry* are discussed. Finally, results of a *retrospective calculation of the dose distribution* from the actual treatment performed in 2012 are shown. While all data presented in the results part of this section was generated for MLC 1, similar results are expected

for MLC 3.

Correction Factors for Absolute Dose Calculation

For the generation of correction factors for MLC 1, two separate sets of MC calculations were run with 5×10^9 starting neutrons and gammas, respectively. This number of starting particles was high enough to obtain relative tally errors below 5 % in the tally region. With the water phantom in place, neutron and gamma doses in 5 cm depth in water of $D_n = 4.147 \times 10^{-18}$ Gy ± 0.53 % and $D_\gamma = 1.802 \times 10^{-18}$ Gy ± 1.10 % normalized per source particle were obtained. From these values, dose rates were calculated using the initial values for $\dot{\Phi}_n$ and $\dot{\Phi}_\gamma$ to be $\dot{D}_{n,sim} = 0.352$ Gy/min $\pm 0.57\%$ and $\dot{D}_{\gamma,sim} = 0.166$ Gy/min $\pm 1.05\%$. From the measured dose values $\dot{D}_{n,meas} = 0.330$ Gy/min and $\dot{D}_{\gamma,meas} = 0.180$ Gy/min [75] corrections factors of $f_n = 0.9375 \pm 0.57$ % and $f_\gamma = 1.0840 \pm 1.05$ % were calculated for the neutron and gamma dose rate, respectively. From the error limits of the measured fluence rate of $\dot{\Phi}_n = 3.2(2) \times 10^8$ cm^{-2}s^{-1}, the correction factor for neutrons can be seen to correspond to the lower limit of $\dot{\Phi}_n = 3.0 \times 10^8$ cm^{-2}s^{-1}.

Even though correction factors can in principle be calculated to account for reported differences in calculated and measured absolute dose values, an improvement especially regarding measurements of the gamma spectrum and fluence rate are expected to give more confidence in the simulated absolute gamma dose. Due to the correspondence with the error limits of the neutron fluence, the calculated value for f_n is reasonable.

Results of Segmentation Process

Automatic segmentation and post-processing of the planning CT also used in section 4.1.2 were performed as described in the methods part of this section. The input data contained Hounsfield Units ranging from $HU_{min} = -1000$ to $HU_{max} = 3071$. In the post-processing, the skin thickness was set to 1 mm and 5563 voxels were re-defined to be either air or soft tissue. The data set contains a total number of 607569 voxels.

As discussed above, a *mean material density* is calculated for the different tissue types as input for the MCNP simulation. Histograms visualizing the number of voxels within density intervals calculated from the HU are given for soft tissue (st), skin (sk), and bone (b) in figure 4.22. The calculated mean densities for the three tissue types are $\rho_{st,mean} = (1.007 \pm 0.115)$ g/cm^3, $\rho_{sk,mean} = (1.014 \pm 0.260)$ g/cm^3, and $\rho_{b,mean} = (1.555 \pm 0.348)$ g/cm^3 and can be compared to the densities of $\rho_{st,NIST} = 1.000$ g/cm^3, $\rho_{sk,NIST} = 1.100$ g/cm^3, and $\rho_{b,NIST} = 1.850$ g/cm^3 given in the data-tables provided by NIST [47]. While the difference between the mean density calculated for soft tissue and the one given by NIST is below 1 % and therefore negligible, the calculated value for skin and bone are about 8 % respectively 16 % lower than the reference values.

The histogram plots in figure 4.22 suggest to adopt the HU interval from table 4.2 at least for bone by dividing it into a number of finer bins. Finer bins would then still

contain bone tissue but in a reasonable number of subsets of different mean densities. The large standard deviation around the mean value especially for bone could then be included. While the standard deviation of about 25 % of the mean value for skin is also large, it is probably advisable to keep the HU interval for skin unchanged. Thus, no conflicts will arise in transition regions where low HU and therefore low density values associated to skin can potentially lead to large but false dose values in the calculation process.

An axial view of the *contour information* is given as overlay on the CT data in figure 4.23a. Here, all voxels inside the patient except for cavities and the contoured bone and skin regions are passed to MCNP as soft tissue. The MCNP simulation volume is shown in figure 4.23b as visualized by the MCNP geometry plotter. Here, air, skin, soft tissue, and bone are indicated by purple, turquoise, yellow, and green, respectively. The black grid visible in figure 4.23b shows the MCNP tally that coincides with the voxels in the CT data. Other contoured regions like the PTV and the myelon shown in figure 4.23a are not further processed in the MC calculations but are subsequently used for dose evaluation. The isocenter used in matRad is indicated by the black cross in figure 4.23a.

Evaluation of KERMA and Total Dose Calculations

For a *comparison of the two options* for MC dose calculation using KERMA-factors (A) and total dose tallies (B), the surface source file generated using the MATLAB application for the actual treatment field (cf. figure 4.21) was positioned at a distance of 100 cm away from the matRad isocenter shown in figure 4.23a. As discussed above, the general expectation holds true that option B gives more accurate results while option A is expected to run faster due to the reduced number of transported particles. A comparison on patient CT data was chosen above a comparison in water since general good agreement with measured data of option B was already shown in section 4.1. Option B is therefore used as reference for the performance of A.

All simulations were run with about 1.1×10^7 starting neutrons or gammas read from the surface source file. While the expectation regarding the calculation speed of the MCNP simulation using KERMA-factors was met for gammas, the result was inverted for neutrons. For gammas, the simulation applying option A run faster by a factor of 1.1 compared to the simulation applying option B. For neutrons, a reduction in speed of option A regarding option B by a factor of 0.9 is reported. All MC calculations and data storage operations were executed by MCNP for neutrons and gammas within a reasonable time of $8 - 12$ hours in parallel mode using 20 Intel Xeon Platinum 8160 CPUs with 2.1 GHz each. About 20 GB of RAM are sufficient to run the individual simulations.

A quantitative comparison between the two options for dose calculation is performed using the *γ-evaluation-method* [41] with a 3 %/3 mm-criterion. A function for the gamma evaluation is already implemented in matRad and voxel-specific and contour-specific results can be obtained as output. For the evaluation, the dose cubes
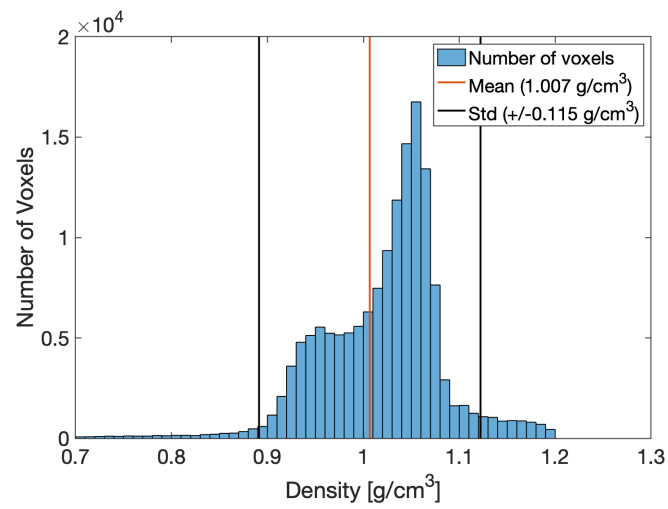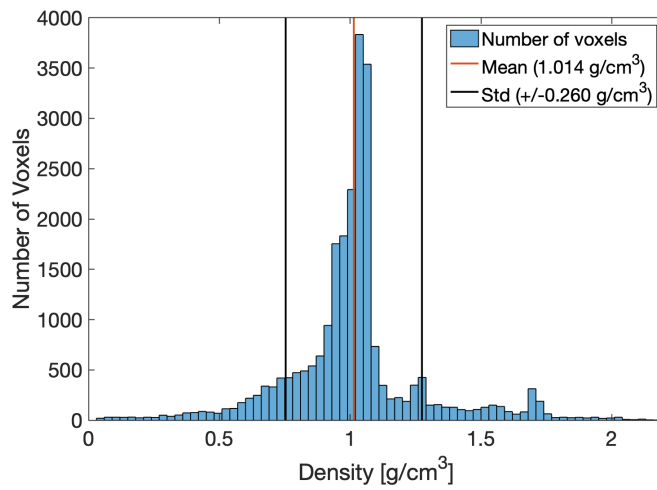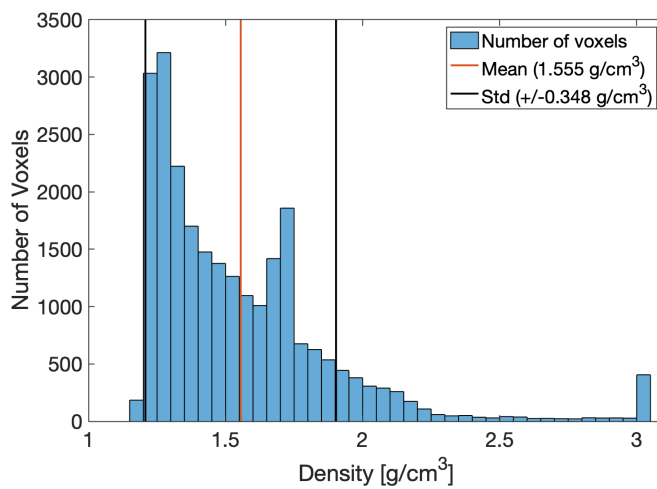
Figure 4.22: Density distribution of voxels associated to (a) soft tissue, (b) skin, and (c) bone.
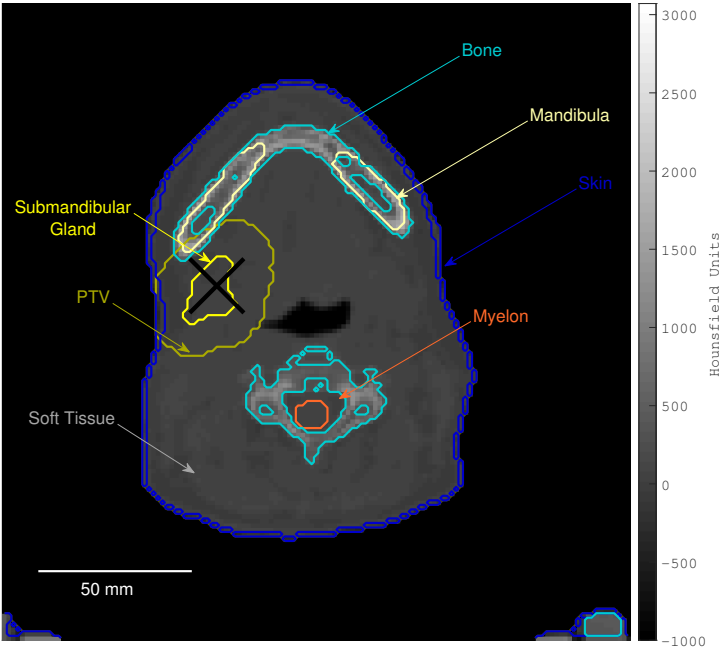
(a)
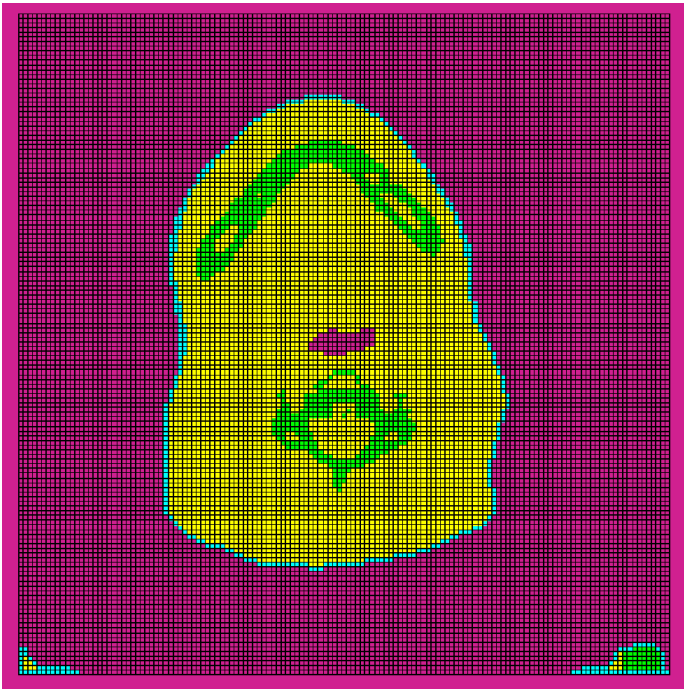
(b)

Figure 4.23: Visualization of patient anatomy and tissue information (a) on CT data as shown in matRad and (b) in combination with the tally grid visualized by MCNP plotter.

containing results from the total dose option were used as reference.

Results of the γ-evaluation for the neutron and the gamma component of the beam in axial view for the same CT slice as for example in figure 4.23a are visualized in figure 4.24. For neutrons, all organ- or contour-specific pass-rates are above 99 % except for bone where a pass-rate of 98.3 % was calculated. The good agreement between KERMA and total dose can be seen in figure 4.24a. For the gamma component of the beam, the dose is overestimated especially in the build-up region close to the surface as can be seen in figure 4.24b. While a pass-rate of 96.0 % is reported for the whole CT, pass-rates for the PTV and the submandibular gland are only 81.0 % and 81.7 %. The difference between KERMA and total dose for the gamma component of the beam was expected due to the larger range of secondary electrons as most important secondary charged particles from gamma interactions in contrast to protons and other ions from neutron interactions.

As already discussed in the context of dose calculations applying PBKs, verification measurements in heterogeneous media are also essential for reliable evaluation of the performed dose calculation using MCNP.

While a discussion or investigation of the difference in the performance of the KERMA and the total dose calculations in MCNP is not intended, option B can clearly be identified as favorable option for future dose calculations. While for neutrons the performance of the total dose option is better in terms of speed and accuracy, the slightly better performance of the KERMA option in speed for gamma radiation cannot balance the lack in accuracy. This is especially important since volumes from treatment indications for MEDAPP are mainly located close to the surface where the performance of the KERMA calculations is insufficient.

For both beam components, *relative error information* is provided in table 4.3 for the two dose calculation options. *Maximum, mean, and median relative errors* are given for the whole CT - i.e. all voxels - and for selected volumes of interest like the PTV or the brainstem. Mean and median are calculated from the relative errors of all non-zero tally values associated to a voxel inside the regarding volumes of interest. In general, relative errors below 10 % or even 5 % are recommended [81][p. 2-116] for MCNP

Table 4.3: Maximum, mean, and median relative error information calculated from MCNP tally-output for selected contours and different beam components.

	Option A: neutrons			Option B: neutrons			Option A: gammas			Option B: gammas		
	max.	mean	medi.	max.	mean	medi.	max.	mean	medi.	max.	mean	medi.
Whole CT	39.7 %	1.9 %	1.2 %	100 %	10.4 %	6.3 %	37.6 %	2.6 %	1.7 %	100 %	39.0 %	34.8 %
PTV	1.2 %	0.8 %	0.8 %	2.8 %	0.8 %	0.8 %	1.3 %	1.1 %	1.1 %	6.8 %	0.9 %	0.8 %
Subm. gl.	0.8 %	0.8 %	0.8 %	0.9 %	0.8 %	0.8 %	1.1 %	1.0 %	1.0 %	0.8 %	0.8 %	0.8 %
Brainst.	2.1 %	1.5 %	1.5 %	2.3 %	1.7 %	1.7 %	5.9 %	3.2 %	3.1 %	7.1 %	2.5 %	2.4 %
Laryxn	2.5 %	1.1 %	1.1 %	97.5 %	2.9 %	1.2 %	2.4 %	1.5 %	1.5 %	100 %	2.9 %	1.2 %
Mandib.	4.2 %	1.5 %	1.3 %	4.4 %	1.4 %	1.3 %	6.7 %	1.8 %	1.4 %	18.2 %	1.3 %	1.1 %
Myelon	1.5 %	1.1 %	1.1 %	2.1 %	1.3 %	1.3 %	5.6 %	2.3 %	1.9 %	14.1 %	2.0 %	1.5 %
Brain	3.2 %	1.4 %	1.3 %	3.5 %	1.8 %	1.7 %	9.0 %	3.1 %	3.0 %	100 %	4.9 %	4.5 %
Bone	50.8 %	3.8 %	1.8 %	57.2 %	3.1 %	1.7 %	29.0 %	3.6 %	2.2 %	76.5 %	4.6 %	2.0 %
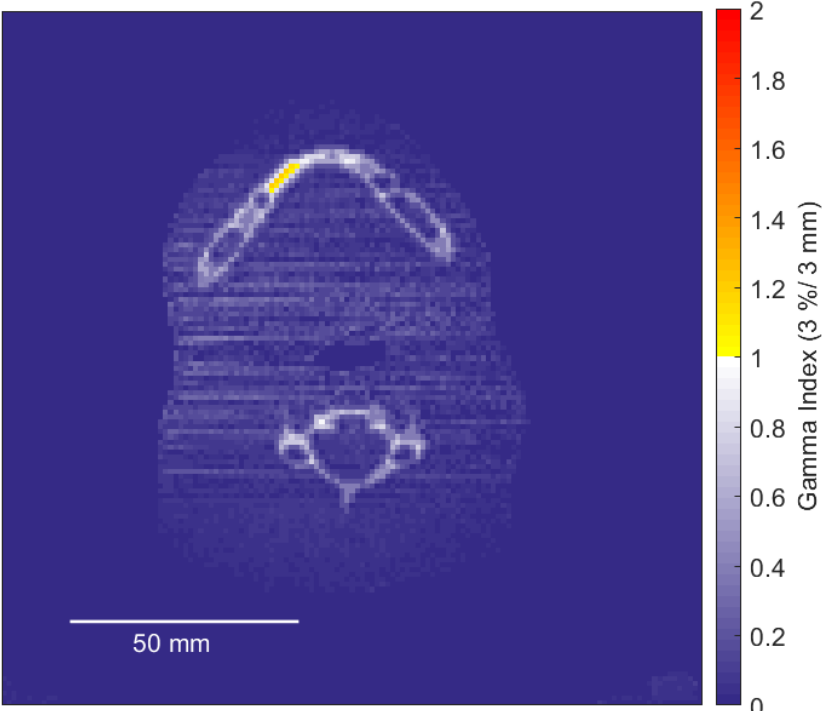
(a)
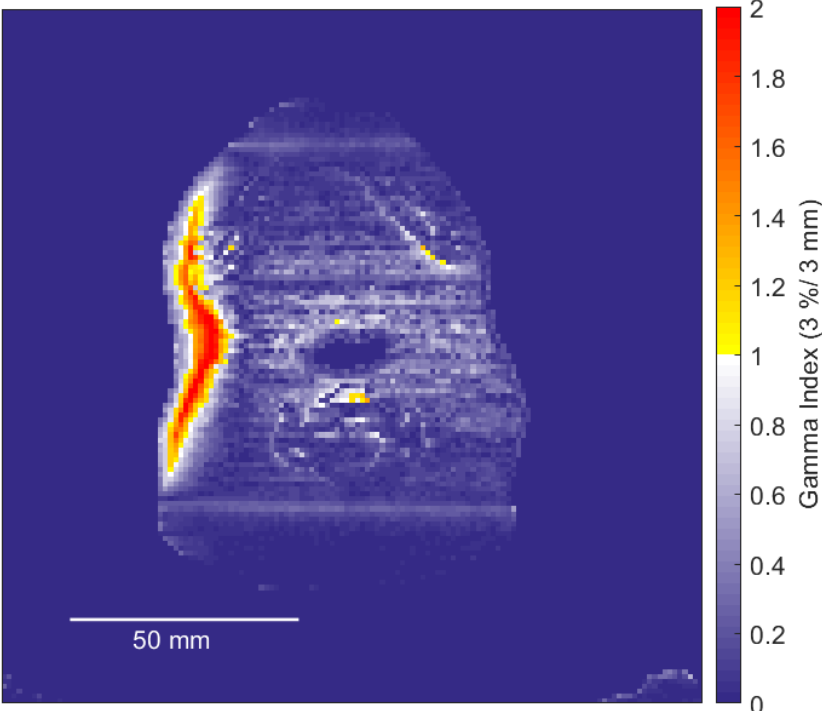
(b)

Figure 4.24: Visualization of γ-index evaluation with $3\,\%/3\,$mm-criterion for comparison of KERMA and total dose calculations for (a) the neutron and (b) the gamma component.

tallies. Since the simulation volume is separated into a large number of voxels that are partly located outside the irradiation site, this criterion cannot be matched for all voxels in the way the dose calculation is realized in the MC dose engine presented here. Nevertheless, maximum, mean, and median values for the relative errors allow an insight into the precision and partly also into the accuracy of the dose calculations.

From a comparison of the respective columns in table 4.3 it can be seen that for most volumes of interest and for the whole CT mean and median relative errors are lower for option A when compared to option B. Maximum relative errors are always lower for the KERMA calculations. This result was expected since tally statistics are also influenced by the number of particle species present in the transport calculation so that simple neutron and gamma fluence calculations give lower relative errors.

For some volumes of interest like the larynx and for the whole CT maximum relative errors up to 100 % are reported. As stated above, the main reason for that are unavoidable large uncertainties in voxels outside the irradiation field. In volumes of interest like the larynx where cavities are included in the contour, a difference between the implementations of option A and B additionally affects tally statistics. While for the KERMA option dose-to-air including the associated relative error is set to zero, the total dose deposition also includes voxels filled with air. Therefore, the number of voxels with non-zero results is conceptually different for the two options, which in turn affects the calculation of the relative error.

To gain confidence about the simulation outcome in terms of the relative error, it should be sufficient to run simulations with a large enough number of starting neutrons or gammas to achieve mean and median errors of around 10 % as recommended for MCNP. For the example discussed here, 1.1×10^7 starting particles were more than sufficient to reach that goal. Nevertheless, the maximum error should be examined carefully with regard to the location of the considered volume. In case a large maximum error is reported for a structure located directly within the irradiation field, the simulation input should be revisited. In such cases, the sampling of regions of interest inside the radiation field would probably inaccurate.

Regarding the relative error analysis it is important to keep in mind that the relative error as provided by MCNP can actually only provide information about the precision of the MC calculation. But the maximum errors reported for particular volumes of interest can help to also estimate at least the accuracy of the sampling in this region. Furthermore, the accuracy of the MC dose calculation is influenced by the input spectrum, the velocity vector distribution written to the surface source file, and by the physics modelled in MCNP. No real benefit regarding the relative error is provided by choosing the KERMA option for dose calculation.

Retrospective Dose Calculation on Patient CT

While PB calculations for the kernels discussed in section 4.1.2 are only meaningful for a distance of about 100 cm between the patient and the reactor wall, the position of the patient can be chosen with more flexibility for the MC calculations. As stated above, a

distance of 40 cm from the wall was used for the treatment. For the calculation of the dose distributions shown in figures 4.25, 4.26, and 4.27, a distance of 40 cm between the patient surface and the wall was defined. Therefore, the results give an *adequate retrospective dose distribution* for one fraction of the treatment performed in 2012. The neutron and gamma dose distributions shown in figures 4.25a and 4.25b, respectively, were calculated for initial fluence rates at patient position of $\dot{\Phi}_n = 3.2 \times 10^8 \ \mathrm{cm^{-2}s^{-1}}$ and $\dot{\Phi}_\gamma = 2.9 \times 10^8 \ \mathrm{cm^{-2}s^{-1}}$ including the correction factors discussed above. For all results presented in the following, the dose calculations were performed using the total dose option. While the correct separation of neutron and gamma component was performed for the calculation of the correction factors for the total dose calculation from primary neutrons and gammas, the total dose option falsely associates secondary gamma dose from primary neutrons to neutron dose. Therefore, a systematic error is expected in the separation of the neutron and gamma component but the total dose calculation is expected to be correct.

For the neutron component of the dose shown in figure 4.25a, a steep dose gradient with maximum values close to the surface can be seen. As expected, a build-up region cannot be identified. The reduction of dose deposited to bone tissue is clearly visible. A maximum neutron dose of $D_{n,max} = 1.269 \, \mathrm{Gy}$ is reported. The dose distribution of the gamma component shown in figure 4.25b shows a less steep dose gradient in comparison to the neutron component. Again, a build-up region can be identified close to the surface. The maximum gamma dose value is $D_{\gamma,max} = 0.321 \, \mathrm{Gy}$.

The calculated total dose for one fraction can be inspected in axial, coronal, and sagital view in figures 4.26, 4.27a, and 4.27b, respectively. At least from these perspectives, the PTV seems to be covered by the 50 % isodose line. The maximum total dose was calculated to be $D_{max} = 1.499 \, \mathrm{Gy}$ which nearly coincides with the prescribed dose per fraction of $D = 1.5 \, \mathrm{Gy}$.

For a quantitative evaluation, DVH-data can be used as provided by matRad and shown in figure 4.28. For example, 95 % of the PTV volume are covered by 0.735 Gy and 50 % by 1.227 Gy. The maximum dose to organs at risk like the brainstem, larynx, myelon, and skin were calculated to be 0.070 Gy, 0.988 Gy, 0.411 Gy, and 1.418 Gy, respectively. The mean dose to the larynx is 0.463 Gy.
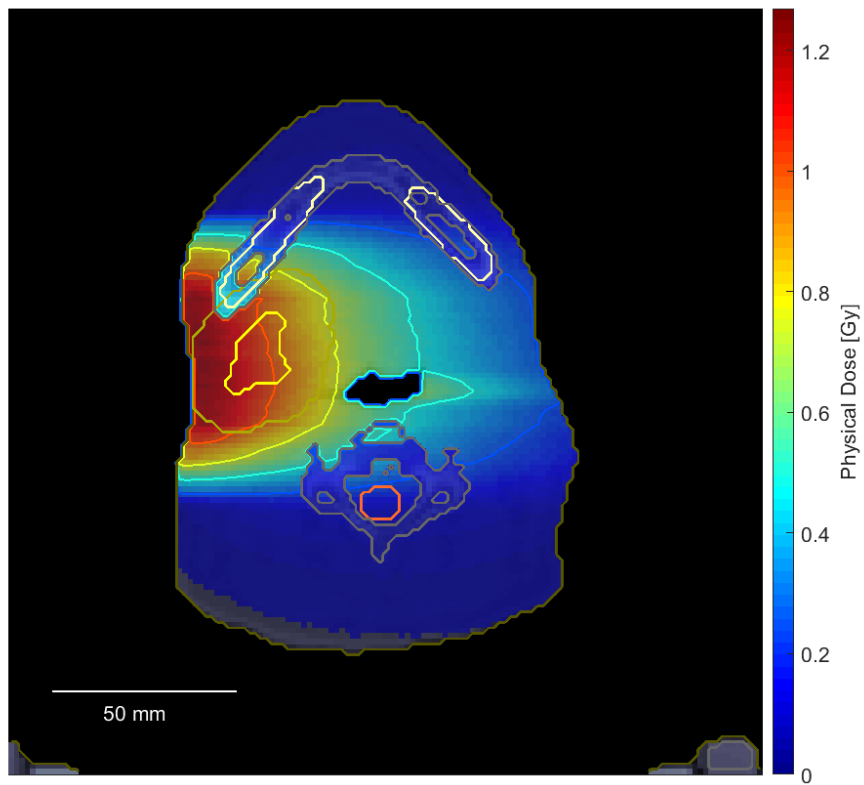
(a)
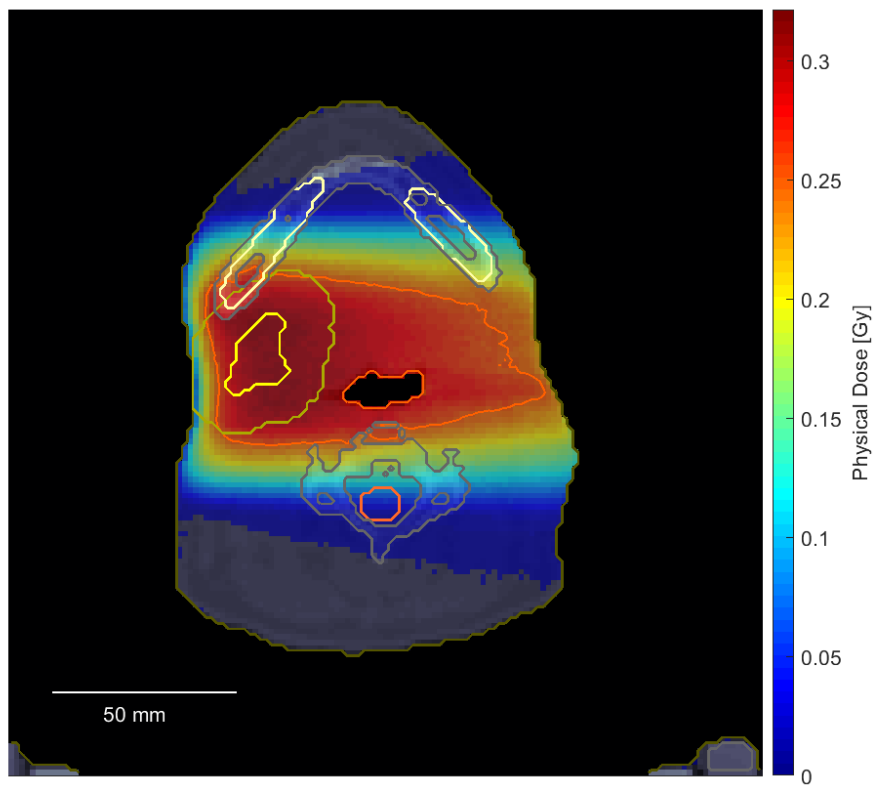
(b)

Figure 4.25: Result of retrospective dose calculation using MCNP for one fraction for (a) the neutron component and (b) the gamma component.
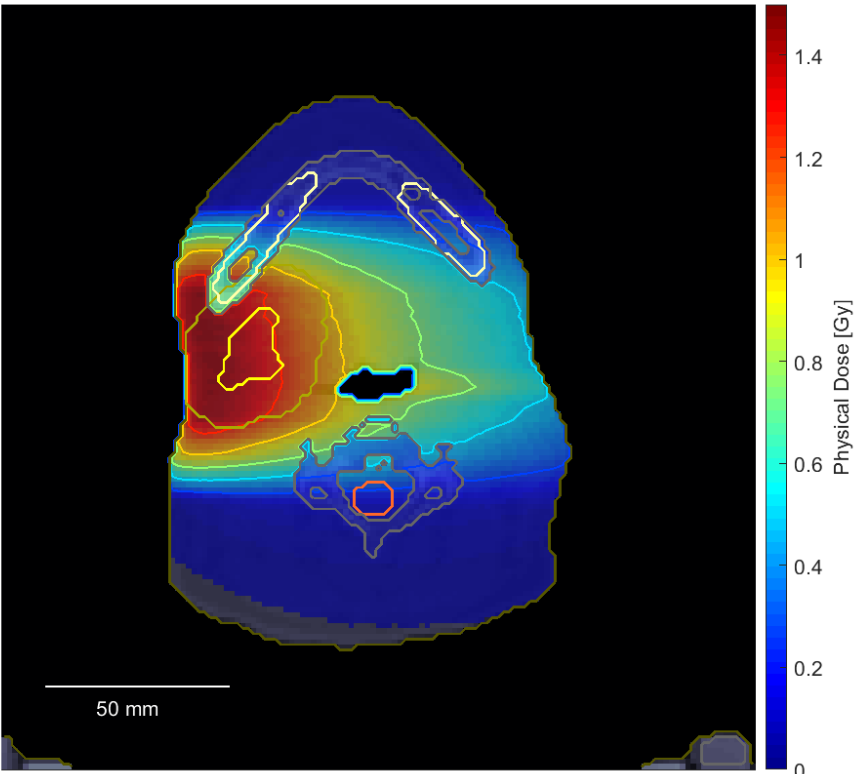
Figure 4.26: Result of retrospective total dose calculation using MCNP for one fraction.

(a)   (b)
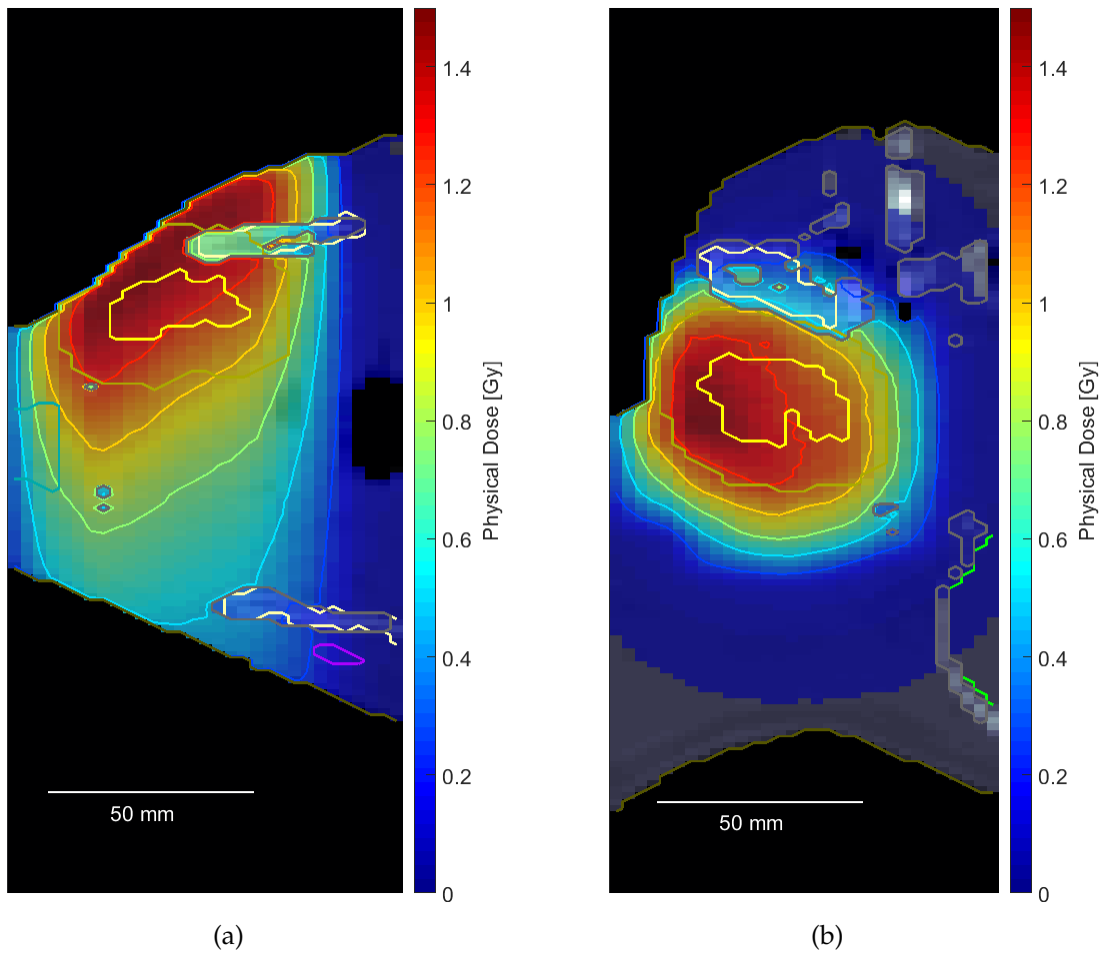
Figure 4.27: Coronal (a) and sagital (b) view of results from retrospective total dose calculation using MCNP for one fraction.
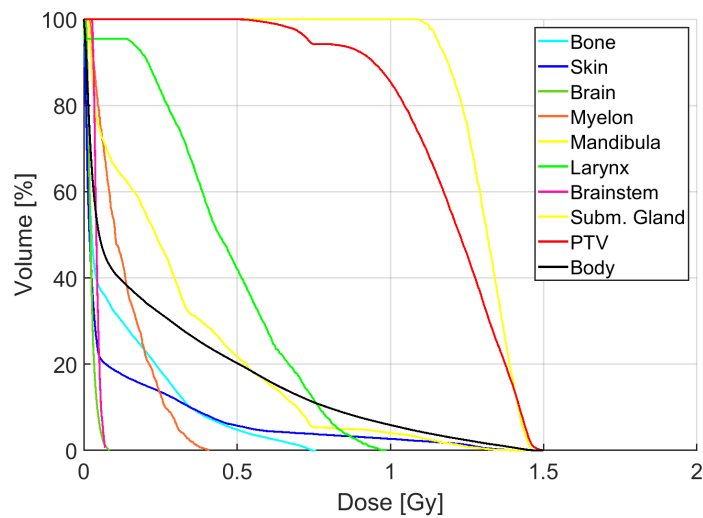
Figure 4.28: DVH calculated from retrospective dose calculation using MCNP.

Effect of Boron-10 Enriched Tissue on FNT

As discussed above, a pre-defined concentration of ^{10}B can be added to the material composition in a specified contour for BNCT. For clinical BNCT with thermal or epithermal neutron beams a ^{10}B-concentration of 20 µg per gram tissue is required (cf. [4] & [15]). For the fast neutron beam present at MEDAPP, a concentration of 20 µg per gram did not lead to a significant increase in deposited dose in the boron enriched tissue. For demonstration purposes, the concentration was increased by factors of 5 and 50 to 100 µg and 1 mg per gram tissue. For the Monte Carlo calculation, the submandibular gland contour was re-named to *PTV_BNCT* and the composition of the voxels within that contour was re-defined for BNCT according to the pre-defined ^{10}B-concentrations. The effect of the different boron concentrations can be inspected in figure 4.29. Here, the red curve indicates the depth dose curve on the central beam axis through the isocenter for the retrospective evaluation discussed in 4.2.2. The blue and green curves indicate the depth dose curve for the boron enriched submandibular gland contour for boron concentrations of 100 µg and 1 mg, respectively. The vertical black lines indicate the boundaries of the boron enriched volume. For the calculation of the dose deposition shown here, the same irradiation conditions regarding the MLC configuration and the neutron and gamma fluence were used as for the retrospective MC calculation.
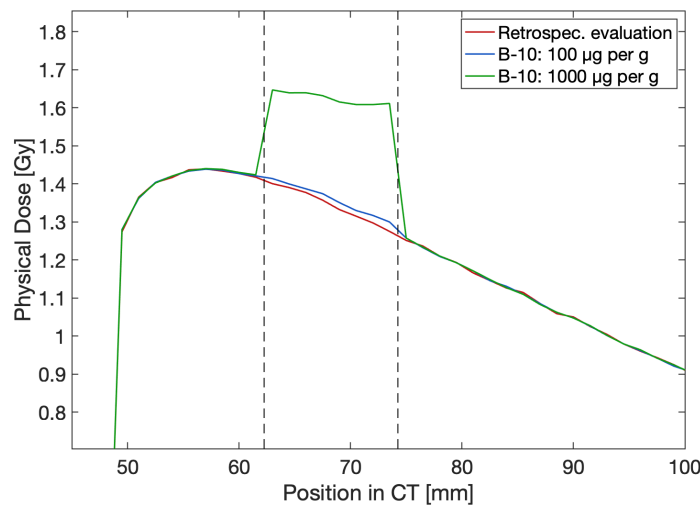
Figure 4.29: Depth dose curves on central beam axis calculated with MCNP for ^{10}B enriched target volume with reference dose deposition in soft tissue.

From figure 4.29, an increased dose deposition is visible within the boundaries of the boron enriched tissue in comparison to the unmodified soft tissue composition used for the retrospective evaluation. Outside the contour boundaries of the PTV for BNCT, the dose deposition is not altered significantly. When assessing the effect in the boundary region, the voxel size of 1.5 mm along the beam axis and the linear interpolation between the sampling points for visualization should be kept in mind.

4.2.3 Discussion

While pencil beam kernels used for dose calculations in heterogeneous media could be evaluated in reference to Monte Carlo simulations, verification measurements for the implemented MC dose engine for heterogeneous media are still necessary. Modifications and fine-tuning for example of the HU-intervals used in the segmentation process are therefore not pursued further in this work. As an example, reasonable results were generated regarding the retrospective evaluation of a head and neck treatment at MEDAPP. This includes the reproduction of the prescribed dose and the expected reduction of dose deposited in bone. Therefore, MC dose calculations are expected to give reasonable results also for retrospective dose calculations for other head and neck treatments and other treatment indications performed at MEDAPP. With the MC dose engine at hand, this potential could be exploited further in the scope of a more extensive retrospective investigation.

Also, the implemented BNCT option for the MC dose engine could be used for an investigation of a potential combination of FNT with a BNCT boost. For the particular example shown above, the ^{10}B-concentration currently available for BNCT was shown to be insufficient to gain a significantly increased dose deposition in the target volume. Nevertheless, the identification of potential treatment sites and the necessary ^{10}B-concentration could be investigated in a more profound feasibility study applying the presented calculation tool. While the optimal neutron spectrum for BNCT is usually considered to be in the thermal or epithermal neutron energy range (cf. [16] & [71]), the MEDAPP neutron spectrum for medical applications is fixed. Leaving aside the ^{10}B-concentration, the optimal location of the target volume and an optimization of the treatment parameters like the number of irradiation angles are the only variable parameters for BNCT feasibility studies at MEDAPP. Here, MC simulations of the spectral neutron fluence in a PE phantom provided by Breitkreutz [9] for the MEDAPP spectrum indicate potential for a combination of FNT and BNCT due to a build-up effect for thermal neutrons with a maximum in about 3 to 4 cm. For potential verification measurements of BNCT dose calculations, the limitations of the two chamber method should be kept in mind.

4.3 Evaluation of Implemented Dose Calculation Approaches

A final assessment of the pencil beam and the Monte Carlo dose calculation approaches is provided in the following. Again, the MC dose calculation is used for the evaluation of the PB approach by the γ-method. For the evaluation, the dose depositions calculated by the two approaches were normalized to 1 Gy in the isocenter in order to eliminate uncertainties in the absolute dose calculation. The isocenter or the reference position in matRad for patient positioning was shown for example in figure 4.23a. While for PB calculation a distance of 100 cm between the patient surface and the wall

Table 4.4: Pass rates of PBK calculations versus MC calculations for selected volumes of interest. Evaluation performed with a γ-criterion of 3 %/3 mm.

	PBK vs. MCNP Neutron Dose	PBK vs. MCNP Neutron Dose w/o Correction	PBK vs. MCNP Gamma Dose
Body	75.5 %	57.4 %	58.1 %
PTV	89.7 %	81.6 %	77.5 %
Subm. gland	88.5 %	87.4 %	77.0 %
Brainstem	100 %	100 %	92.5 %
Larynx	61.4 %	22.74 %	29.9 %
Mandibular	98.0 %	15.9 %	60.2 %
Myelon	68.3 %	61.7 %	55.5 %
Brain	86.5 %	74.4 %	62.1 %
Bone	98.5 %	2.5 %	41.1 %

was used, the patient was slightly moved towards the MLC in the MC calculation. Here, the distance between the wall and the isocenter in the simulation was set to 100 cm. The influence of this shift on the field size was calculated to be less than 0.5 % and is therefore negligible. For the evaluation with the γ-method, a criterion of 3 %/3 mm was used for both beam components.

A visualization of the γ-evaluation is shown in figure 4.30 for both beam components. The slice for the visualization is chosen identical to the slice in 4.23a and in most other axial visualizations. It can be seen from figures 4.30a and 4.30b that the PB algorithm clearly overestimates the dose to out-of-field regions for both beam components. Figure 4.30a shows that air cavities are challenging for the dose calculations using PBKs for neutrons so that the dose downstream from the the esophagus is overestimated by the PBKs. An overestimation of the gamma dose to bone by the PB algorithm is visible in figure 4.30b. Good performance by the PBKs for gammas is reported close to the surface.

Pass rates for the γ-evaluation are given in table 4.4. Here, the impact of the correction factors for neutrons on the dose calculation by PBKs can be analyzed more thoroughly. By comparing the first and second column that give the pass-rates with and without the application of the correction factors, it can be seen that the impact is rather low for organs that mainly consist of soft tissue. For example, pass-rates of the submandibular gland and the brainstem are only slightly improved or were already at 100 % without the correction. The impact is significant for organs that include voxels containing bone. For the contoured bone tissue, the pass rate improves from 2.5 % to 98.5 %. On a first glance, also the impact of the correction factors on the larynx contour seems high. But, this is due to a large number of bone voxels as part of the contoured larynx region.

As stated above for the gamma component, the last columns in table 4.4 shows low pass rates for out-of-field regions like the larynx with only 29.9 % and the bone
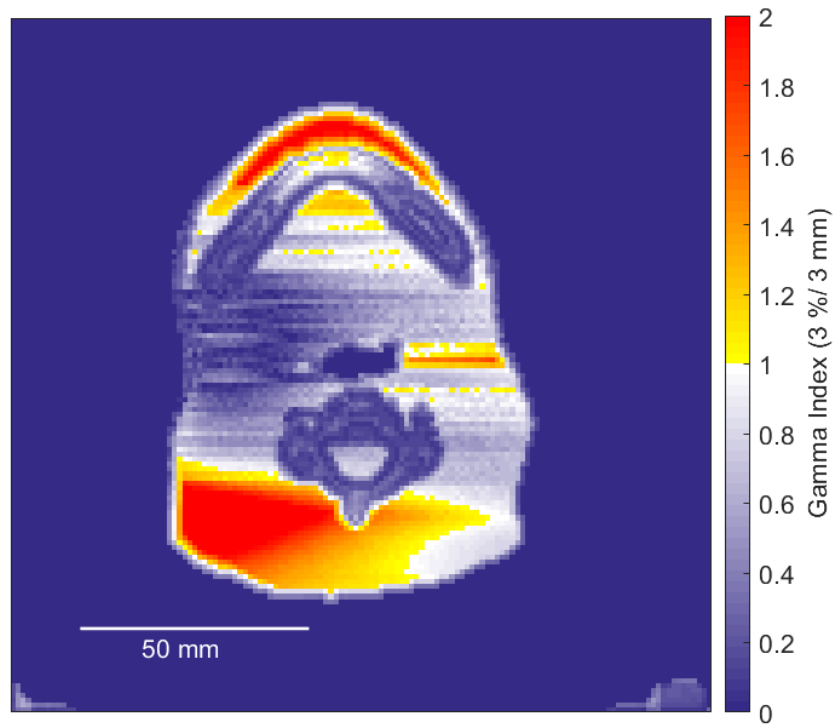
(a)
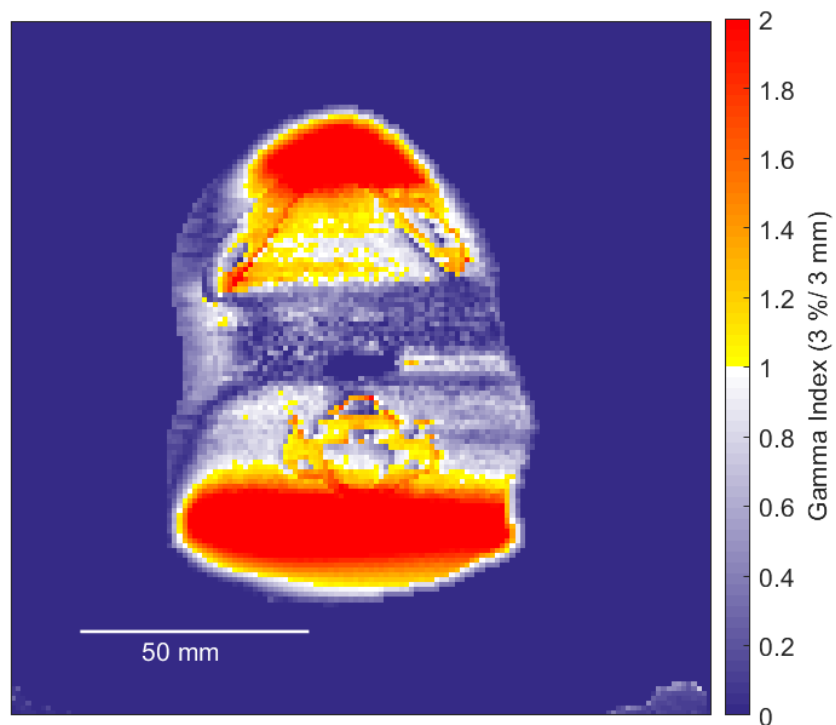
(b)

Figure 4.30: Visualization of γ-evaluation of dose calculations using PBKs with dose distributions from MC calculations as reference for (a) the neutron component and (b) the gamma component.

contour with 41.1 %.

4.3.1 Discussion

With the implemented pencil beam and the Monte Carlo approaches dose calculations for the mixed neutron-gamma radiation field at MEDAPP are now possible within the matRad treatment planning environment. In the calculation procedure, patient anatomy information gained from CT data can be used as input and the outcome of the dose calculations is easily accessible via the matRad interface or via Eclipse. The geometry of the beamline is accounted for and irregularly shaped treatment fields from both MLC versions can be evaluated.

For retrospective dose calculations of FNT treatments performed at MEDAPP, MC dose calculations would be the first choice. In addition, a combination of the time-efficient PB algorithm and the MC approach provide potential for prospective treatment planning - at least from a physicist's point of view. The treatment planning procedure was exemplified in section 4.1.2 for MLC 1 and can of course be extended to MLC 3. For prospective planning it is suggested to consider a combination of dose calculations applying both calculation approaches. For a first dose estimate, the PB algorithm in combination with the correction factors for different tissues is sufficient. In a second step, MC dose calculations could be run for the resulting treatment fields of the PB calculations to gain more confidence about the dose distribution or for quality assurance purposes.

Leaving regulatory issues for the clinical applications and prospective planning with matRad aside, treatment planning for clinical FNT at the CNTS in Seattle can - nevertheless - be taken as reference. For the CNTS, dose calculation is performed using the commercial photon treatment planning software Pinaccle also for fast neutrons. Here, the depth dose curves show deviations from measured data of less than 3 % [35]. While this holds true for all field sizes comparable to the ones used in the work presented here, it should also be kept in mind that the mean neutron energy at the CNTS is significantly higher than the one at MEDAPP. Therefore, the depth dose characteristics for the CNTS and for MEDAPP also differ significantly. From the discussion of the results presented here, it is clear that fine tuning of both the decomposition of PBKs and the input spectrum of the MC simulations is required.

As shown in the evaluation of the heterogeneity corrections, the reliability of the pencil beam algorithm in retrospective dose calculations depends on the considered scenario. The results from the PB algorithm with the heterogeneity corrections applied presented above is in good agreement with the results presented by Söderberg et al. [63]. In both cases, the agreement between MC simulations and the outcome of the dose calculation from the applied photon treatment planning software is highly improved by the application of heterogeneity corrections. Similar to the findings discussed in subsection 4.1.2, an overestimation of dose to the lung slab by the photon treatment planning software is reported by Söderberg et al. But since they

report dose-to-water in the comparison of the applied treatment planning software with MC calculations, a quantitative comparison with results from section 4.1.2 for dose-to-tissue cannot be provided here.

Unfortunately, a reduced number of reactor cycles during the last three years hindered final verification measurements in heterogeneous media. Here, only preliminary but non-reliable results from measurements during the last beamtime in the beginning of 2020 are available. In this first attempt, measurements of the dose distribution in a heterogeneous slab phantom comparable to the one used for calculations in section 4.1.2 were planned. For film dosimetry, it was intended to adopt dosimetry procedures discussed by Reinhardt et al. [53] using gafchromic EBT3 films. While calibration of the gafchromic films was performed for clinical photon and proton radiation in [53], it is expected that an analog calibration also works in a mixed neutron-photon beam. This is due to the fact that protons are the most important secondary charged particles in the energy range of the neutrons present at MEDAPP so that at least in charged particle equilibrium the calibration procedure should also be applicable. It is suggested to chose materials with a comparable hydrogen density ρ_H and in general similar elemental compositions as tissue substitutes like the tissue types that need to be substituted. For lung and soft tissue, polystyrene with $\rho_{H,PST} = 0.003\,\mathrm{g/cm^3}$ and polyethylene with $\rho_{H,PE} = 0.135\,\mathrm{g/cm^3}$ were used in the first attempt in 2020. For bone, capton $\rho_{H,CPT} = 0.037\,\mathrm{g/cm^3}$ would be the ideal candidate for a substitute.

5 On the Calculation of the Relative Biological Effectiveness of the MEDAPP Fission Beam

It is well known that particle and energy specific characteristics like the linear energy transfer have a high impact on the biological effect of charged particle radiation (cf. [13], [17], and [37]). It is therefore clear that knowledge about the secondary charged particle spectra from neutron and - to a minor degree - also gamma interactions within the body is crucial for an assessment of the biological effect of the mixed neutron-gamma radiation field present at MEDAPP. For this purpose, Monte Carlo methods are an optimal choice due to the abilities to model secondary particle production.

The concept of RBE was already discussed in section 2.4 together with equation 2.21 which can be used to calculate the RBE with respect to a given reference radiation. In the following chapter, the calculation of the input parameters RBE_{HD} and RBE_{LD} will be discussed together with an evaluation of the calculated RBE values for MEDAPP. For the purpose of RBE calculations, the repair-misrepair-fixation (RMF) model [13] was selected and the input parameters were calculated using a combination of the so-called Monte Carlo damage simulation (MCDS) and MCNP [66]. MCDS is a MC algorithm for the calculation of local clustering of elementary DNA damage (cf. [60], [61], [69]). This approach was already discussed for different types of irradiation modalities like FNT, ion therapy, and BNCT by Stewart et al. [67], [68] and Streitmatter et al. [70].

The importance to include a consideration of spatially varying RBE values into the treatment planning process for FNT was recently highlighted in a review on the clinical radiobiology of FNT by Jones [33]. Results of the RBE calculations will be given in comparison to measurements performed by Schmid et al. [57] in 2009 at the MEDAPP beamline. In addition, the retrospective dose calculation performed using the MC dose engine from section 4.2.2 is extended by the calculation of voxel-specific RBE values and will be discussed as an example.

5.1 Methods

In order to calculate the RBE for a given dose or fraction size D, the $(\alpha/\beta)_R$-value for the reference radiation R and the values for RBE_{HD} and RBE_{LD} as the ratio of the LQ-model parameter for test and reference radiation with the endpoint of cell

survival are needed as input for equation 2.21. As mentioned above and discussed in detail by Stewart et al. [67], the RMF-model input can be calculated by a combination of a general purpose MC algorithm like MCNP with the MCDS. In order to obtain dose-weighted values for RBE_{HD} and RBE_{LD} from MCNP tallies, equations

$$RBE_{HD} = \sqrt{\frac{\beta_n}{\beta_R}} = RBE_{DSB} = \frac{1}{D} \sum_i \int dE \, D_i(E) \, RBE_{DSB,i}(E) \qquad (5.1)$$

and

$$\begin{aligned} RBE_{LD} &= \frac{\alpha_n}{\alpha_R} = RBE_{DSB} + \frac{2 \, \bar{z}_F \, RBE_{DSB}^2}{(\alpha/\beta)_R} \\ &= RBE_{DSB} + \frac{2}{(\alpha/\beta)_R} \frac{1}{D} \sum_i \int dE \, D_i(E) \, \bar{z}_{F,i}(E) \, RBE_{DSB,i}^2(E) \end{aligned} \qquad (5.2)$$

can be used. Here, RBE_{DSB} and $\bar{z}_F \, RBE_{DSB}^2$ indicate the dose-weighted RBE for double strand breaks (DSB) and the dose-weighted product of frequency-mean specific energy and the square of RBE for DSB, respectively. Energy-dependent values $RBE_{DSB,\,i}(E)$ and $\bar{z}_{F,\,i}(E)$ were calculated for all simulated charged particles using the latest MCDS version 3.10A provided on the MCDS web page [65]. Individual charged particle species like ions and electrons are indicated by index i and $RBE_{DSB,\,i}(E)$ and the product of $\bar{z}_{F,\,i}(E)$ and $RBE_{DSB,\,i}^2(E)$ can be used as energy-dependent and particle-dependent tally multipliers in the MCNP simulation. For this purpose, F6 heating tallies are defined in the simulation with and without multipliers so that the dose-averaged values can be obtained as indicated by the sum and integral on the right side of equations 5.1 and 5.2.

As discussed by Semenenko and Stewart [60], the Monte Carlo damage simulation mainly focuses on the formation of local DNA-damage clusters and the RBE for DSB is calculated in reference to ^{60}Co gamma radiation. In the latest version of the MCDS algorithm, oxygen conditions within the cells from aerobic to hypoxic can also be included in the calculation of RBE_{DSB}. The implementation in the MCDS is based on the assumption that the oxygen effect arises from competing processes of oxygen fixation and chemical repair of damage produced by ionizing radiation [69].

In the MCDS, the frequency-mean specific energy for different types of directly ionizing radiation is calculated from $\bar{z}_F \approx LET/\rho d^2$ (cf. [68] & [28]) where the linear energy transfer and the material density are indicated by LET and ρ, respectively, and d indicates the diameter of the cell nucleus. For the diameter of the cell nucleus, a value of $d_{cell} = 5$ μm was chosen for the calculation. To allow a modification of this value after running the MCNP simulation, an additional parameter was introduced in the MATLAB evaluation scripts. As discussed in ICRU report 26 [28], the specific energy z_F indicates the energy imparted to a region of interest divided by this region's mass and the frequency-mean is calculated from the distribution of single energy deposition events in the region of interest.

The RBE calculations were included into the MC dose engine discussed in chapter 4. Again, tallies for dose deposition and tallying RBE parameters are positioned in every voxel of the simulation geometry. As discussed above, the used F6 heating tallies were modified by tally multipliers. Like for the MC dose engine, MATLAB functions for data storing and processing were implemented to be compatible with the matRad treatment planning environment. Since RBE modelling is available in matRad for protons and heavier ions, the visualization capabilities from matRad for RBE and RBE-weighted dose overlaid on CT data can also be used for the mixed neutron-gamma radiation. All RMF-model-parameters calculated in the MC simulations are stored on a grid so that voxel-specific information is available as input for equation 2.21. Therefore, $RBE(D)$-values can be re-calculated in dependency of the dose or fraction size and the cell diameter. Furthermore, $(\alpha/\beta)_R$-values for the reference radiation can also be modified for all volumes of interest contoured on the CT data.

Parameters for the calculation of RBE_{LD} and RBE_{HD} are available from the MCDS down to ion energies of $1\,keV$ and electron energies of $10\,eV$. High variations in the RBE parameters are reported especially in the low energy range. As a trade-off between simulation speed and accuracy, the ion and electron cut-off energies in MCNP were lowered down to $99\,keV$ and $49.9\,keV$, respectively, and for the tally bin with lowest energy the average value of all bins below that energy was taken.

Measured data for RBE as reference for the simulations discussed in the following were taken from Schmid et al. [57]. In the measurement, fresh peripheral blood samples were placed into a PE phantom and irradiated with single fractions at MEDAPP using MLC 1 with a large field size. For the measurement, the induction of dicentric chromosomes was chosen as endpoint for RBE calculations. The dose was measured in depths of $2\,cm$ and $6\,cm$ at the same positions where the irradiations of the biological samples were performed. Doses between $D_{min,2\,cm} = 0.14\,Gy$ and $D_{max,2\,cm} = 3.52\,Gy$ were applied in $2\,cm$ and $D_{min,6\,cm} = 0.18\,Gy$ and $D_{max,6\,cm} = 3.04\,Gy$ in $6\,cm$. For the reference radiation, Schmid et al. used a standard reference dose-response curve for ^{60}Co gamma radiation with $(\alpha/\beta)_R = 0.196\,Gy$. For the simulation, a virtual phantom made of soft tissue was generated in MATLAB with approximately the same outer dimensions as the PE phantom used for the measurement and a voxel size of $4 \times 4 \times 4\,mm^3$. While the media do not match exactly, good agreement is expected between dose deposition in soft tissue and polyethylene as discussed in section 4.3.1. The field size in the simulation was set to $9 \times 9\,cm^2$ in order to save computational resources. The area of the field size in the simulation only corresponds to about $18\,\%$ of the field size from the measurement but an approximately constant neutron-over-gamma ratio was measured in $5\,cm$ depth for MLC 1 (cf. [75]) for square fields with side lengths larger or equal to $9\,cm$. Therefore, only a minor influence from the increasing gamma component from an increasing number of (n, γ)-reactions for increasing field sizes is expected.

5.2 Results

As stated above, the results of the RBE calculations within the MC dose engine are given *first* in reference to measured RBE values for MEDAPP and *second* as outcome for the retrospective irradiation scenario used throughout chapter 4. For the comparison with measured data, the difference in the defined endpoints that also influence $(\alpha/\beta)_R$ should be kept in mind.

5.2.1 Comparison of Measured and Calculated RBE Values

In table 5.1, a comparison between the measured and calculated RBE values for well oxygenated cells is provided. In the two dark grey lines, the results of the RBE values measured by Schmid et al. [57] for depths of 2 cm and 6 cm in polyethylene are given for the minimum and maximum applied dose levels. Simulations for the soft tissue phantom were run twice in MCNP using two different MCDS tally modifiers for aerobic conditions with 100 % of cellular oxygen concentration and hypoxic conditions with 0 % oxygen concentration. Results of the two simulations with different oxygenation levels are provided in table 5.2. Oxygenation levels for the measurements are not provided in [57] but there is no reason to assume hypoxic conditions. Simulations were scaled to the same dose levels at reference depths as applied in the measurements. The reference depth and applied doses are indicated in columns two, three and five of table 5.1 and columns one, two and four of table 5.2, respectively. In the post-processing procedure for all RBE calculations according to equation 2.21, the cell nucleus diameter was re-scaled to $d_{cell} = 4$ μm. The $(\alpha/\beta)_R$-values for the reference radiation used for the evaluation are indicated in column two in table 5.1. Here, the lower value of 0.119 Gy is the lowest value of $(\alpha/\beta)_R$ within the error limits provided by Schmid et al. [57]. For the comparison of the two oxygenation levels, a constant $(\alpha/\beta)_R$ was used.

Better agreement of the measured and calculated RBE values is given for aerobic

Table 5.1: Comparison of measured and calculated RBE values for varying dose levels and reference depths. Simulations were performed for aerobic conditions. Endpoints for RBE are formation of dicentrics and cell survival for the measured and simulated data, respectively.

	$(\alpha/\beta)_R$ [Gy]	Depth [cm]	Dose [Gy]	RBE	Dose [Gy]	RBE
Measurement	0.196	2	0.14	5.9	3.52	1.6
Simulation	0.196	2	0.14	5.5	3.52	2.3
Simulation	0.119	2	0.14	5.6	3.52	2.3
Measurement	0.196	6	0.18	4.1	3.04	1.5
Simulation	0.196	6	0.18	4.3	3.04	2.3
Simulation	0.119	6	0.18	4.4	3.04	2.3

conditions set in the MCDS. As indicated in table 5.1 for aerobic conditions, the deviations are below 7 %. For the higher dose level, the measured RBE values are overestimated by the calculated ones by about 40 to 50 %. RBE values calculated for hypoxic conditions are substantially higher than for aerobic conditions (cf. table 5.2). Since the main objective of this work was to include RBE calculations into the MC dose engine, a detailed discussion of the radiobiology involved in the simulated processes in order to explain the differences between measured and simulated data is not provided here. Nonetheless, a few remarks can be provided as a plausibility check for the simulations. First, looking from a radiobilogical standpoint the difference in the selected endpoints comprises a systematic difference in the respective evaluation of measured and simulated data. Second, the general trend of decreasing RBE values with increasing dose seen in the measurement is reproduced by the simulations. And last, an increase in RBE for decreasing oxygen concentration when comparing higher LET radiation to ^{60}Co gamma radiation as for example discussed by Stewart et al. [69] is also reported in the simulated data.

In addition to the comparison provided above, figures 5.1 and 5.2 show calculated RBE values in combination with depth dose curves and beam profiles in 1.8 cm depth for the minimum and maximum dose from table 5.1 delivered to the reference position in 2 cm depth in the soft tissue cube under aerobic conditions. The blue and green curves refer to the left ordinate and indicate the physical and RBE-weighted dose, respectively. The red curves refer to the right ordinate and indicate the RBE values which correspond to the ratio between green and blue curves. Curves shown in figures 5.1a and 5.2a are scaled to a physical dose of $D_{min,2\,cm} = 0.14$ Gy and curves shown in figures 5.1b and 5.2b are scaled to $D_{max,2\,cm} = 3.52$ Gy.

While the calculated RBE values given in figure 5.1a for the low dose level show an alternation of decreasing, increasing, and again decreasing trends with increasing depth, an overall decrease with increasing depth is reported for the high dose level shown in figure 5.1b. For the latter, the decrease in RBE appears to be approximately linear for depths larger than about 20 mm. In figures 5.2a and 5.2b, a dependency of RBE on the lateral position within the beam can be seen for the two dose levels. As shown in figure 5.2a for $D_{min,2\,cm} = 0.14$ Gy, RBE values larger than 15 are reported for the lateral dose region below 10 % of the central axis dose so that the RBE-weighted

Table 5.2: Comparison for simulated RBE values for different oxygenation conditions for $(\alpha/\beta)_R = 0.196$ Gy. Aerobic conditions refer to 100 % cellular oxygen concentration and hypoxic to 0 %.

	Depth [cm]	Dose [Gy]	RBE	Dose [Gy]	RBE
Sim. (aerobic)	2	0.14	5.5	3.52	2.3
Sim. (hypoxic)	2	0.14	12.5	3.52	4.5
Sim. (aerobic)	6	0.18	4.3	3.04	2.3
Sim. (hypoxic)	6	0.18	10.3	3.04	4.1
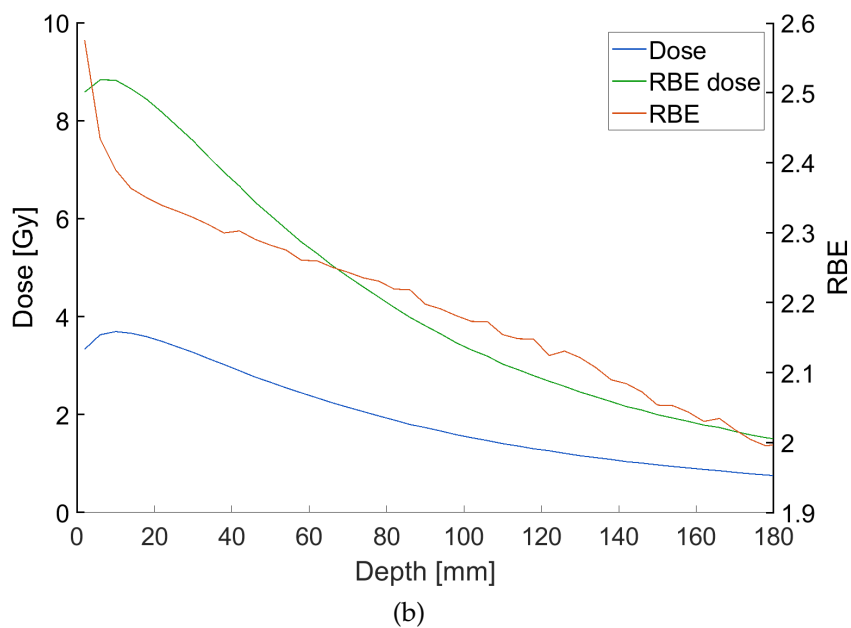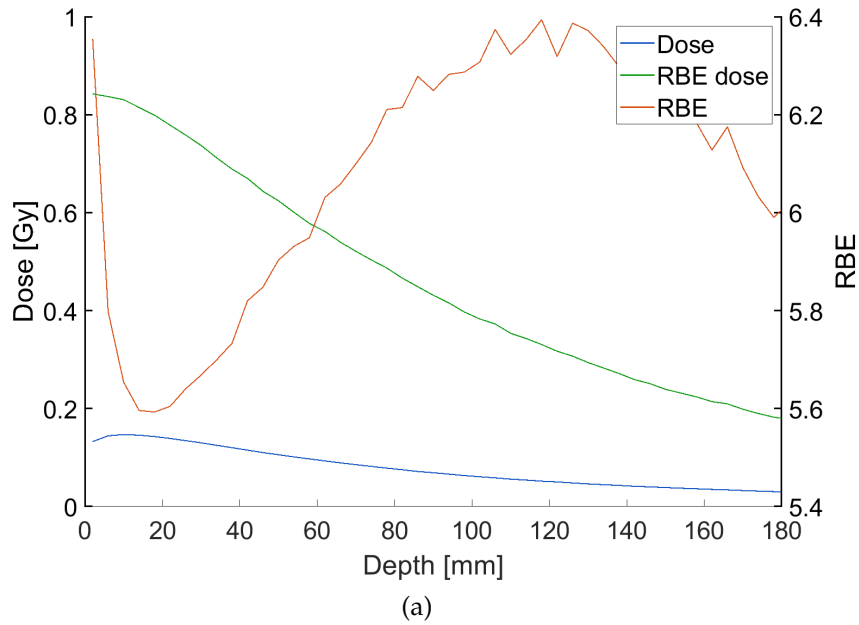
Figure 5.1: Depth-dependent dose and RBE-weighted dose curves (left ordinate) and RBE curve (right ordinate) calculated for $(\alpha/\beta)_R = 0.196\,\text{Gy}$ scaled to (a) $D = 0.14\,\text{Gy}$ and (b) $D = 3.52\,\text{Gy}$ in 2 cm depth.

(a)

(b)
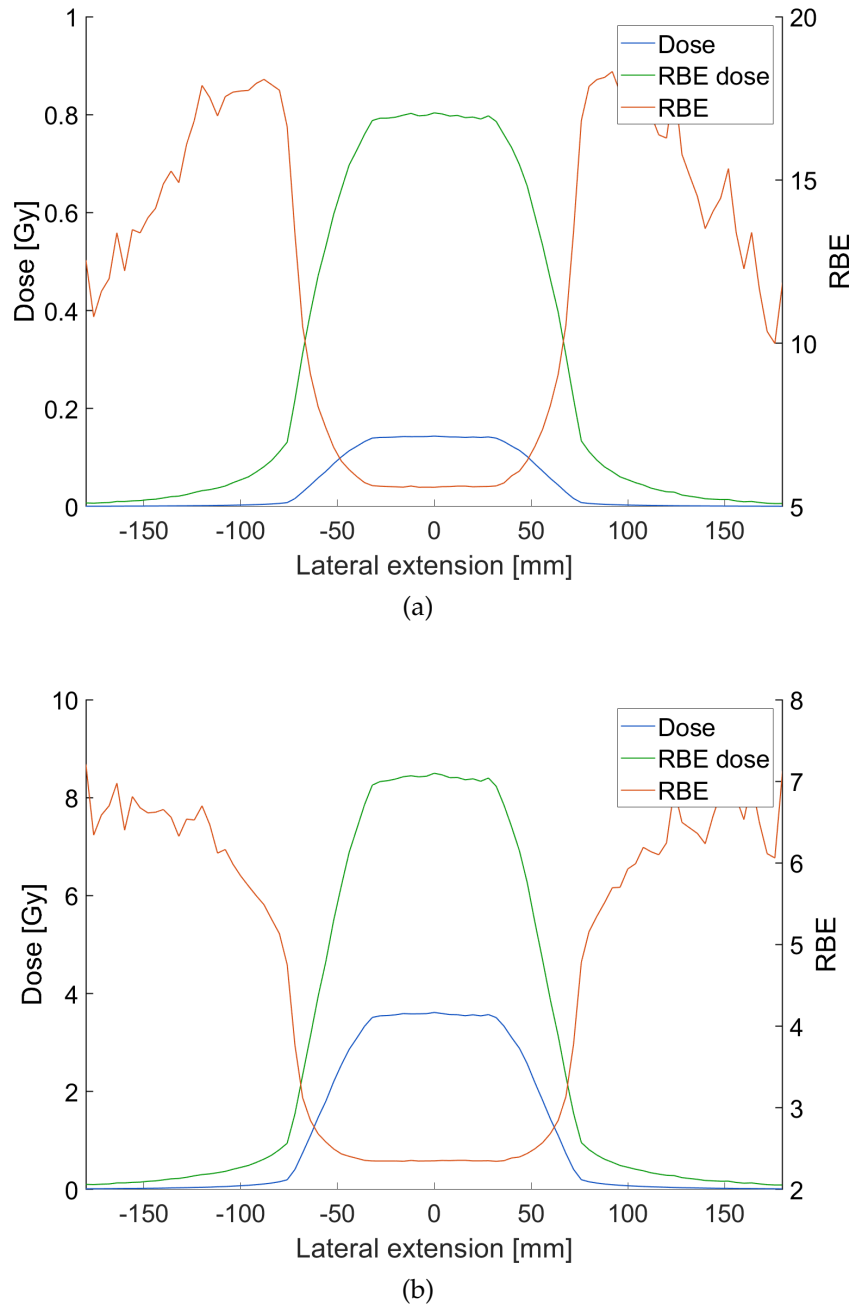
Figure 5.2: Lateral profiles of dose and RBE-weighted dose curves (left ordinate) and RBE curve (right ordinate) at $1.8\,\mathrm{cm}$ depth calculated for $(\alpha/\beta)_R = 0.196\,\mathrm{Gy}$ normalized at $2\,\mathrm{cm}$ depth to (a) $D = 0.14\,\mathrm{Gy}$ and (b) $D = 3.52\,\mathrm{Gy}$.

dose can be in the same order of magnitude as the physical dose on the central beam axis.

5.2.2 RBE Calculations on Patient CT Data

Figure 5.3 shows an axial view of CT data overlaid with calculated RBE values for the same CT slice as for example in figure 4.23a. The retrospective dose calculation was performed with the same irradiation parameters as described in section 4.2 but with the changes applied in the MC calculation as described in 5.1. The dose maximum from the summed charged particle heating was calculated to be 1.461 Gy which is about 3 % lower than the maximum calculated with the total dose tally applied in section 4.2. As shown in the figure 2.6b, a deviation of a few percent can be expected between total dose and summed charged particle heating close to the surface.

Results shown in figure 5.3 were generated with contour-specific $(\alpha/\beta)_R$-values for aerobic conditions defined for all voxels. Contours are shown in the same color coding as in figure 4.23a so that for example bone in gray and the submandibular gland in yellow. Only the PTV color differs and is set to black. $(\alpha/\beta)_R$-values were set to 3.5 Gy for all contours except the PTV, submandibular gland, bone, and skin. For the latter four, $(\alpha/\beta)_R$-values were set to 9 Gy. While the selection of the exact $(\alpha/\beta)_R$-values was ad hoc, the classification of skin, bone marrow, and many tumour as *early responding tissues* limited the range of reasonable $(\alpha/\beta)_R$-values to $7 - 10$ *Gy* [44]. All other tissues were assumed to be *late responding* suggesting $(\alpha/\beta)_R = 3 - 5$ *Gy*. A more detailed discussion of late and early reacting tissue is provided in [44] but is omitted here. The diameter of the cell nucleus was left unchanged from the MCDS calculations to be $d_{cell} = 5 \, \mu m$.

An increase in RBE with lateral distance to the central beam axis is clearly visible in figure 5.3. Furthermore, the dependency of the calculated RBE on the $(\alpha/\beta)_R$-values is also visible when for example comparing the RBE in the PTV-region with the RBE calculated for soft tissue in proximal beam direction.

The two white lines in figure 5.3 are given as reference for the two depth dose profiles shown in figure 5.4. Figure 5.4a corresponds to the lower line going through the isocenter and figure 5.4b corresponds to the upper line which is shifted by 15 mm in ventral direction. Again, the blue and green curves show the physical and RBE-weighted dose and RBE values are indicated in red. In figure 5.4a, PTV-boundaries are indicated by the solid black vertical lines. Here, depth characteristics of the RBE curve are comparable to figure 5.1b but the influence of the different $(\alpha/\beta)_R$-values inside and outside the PTV is visible as a shift in RBE. Along the depth profile, the RBE for adjacent voxels belonging to the PTV and soft tissue, respectively, is reported to change from $RBE = 2.52$ to $RBE = 2.86$. This corresponds to an increase of 14 % with approximately constant dose for the adjacent voxels. It should be kept in mind that the PTV and the surrounding soft tissue are defined to have the same elemental composition and density in MCNP. The influence of a changed elemental
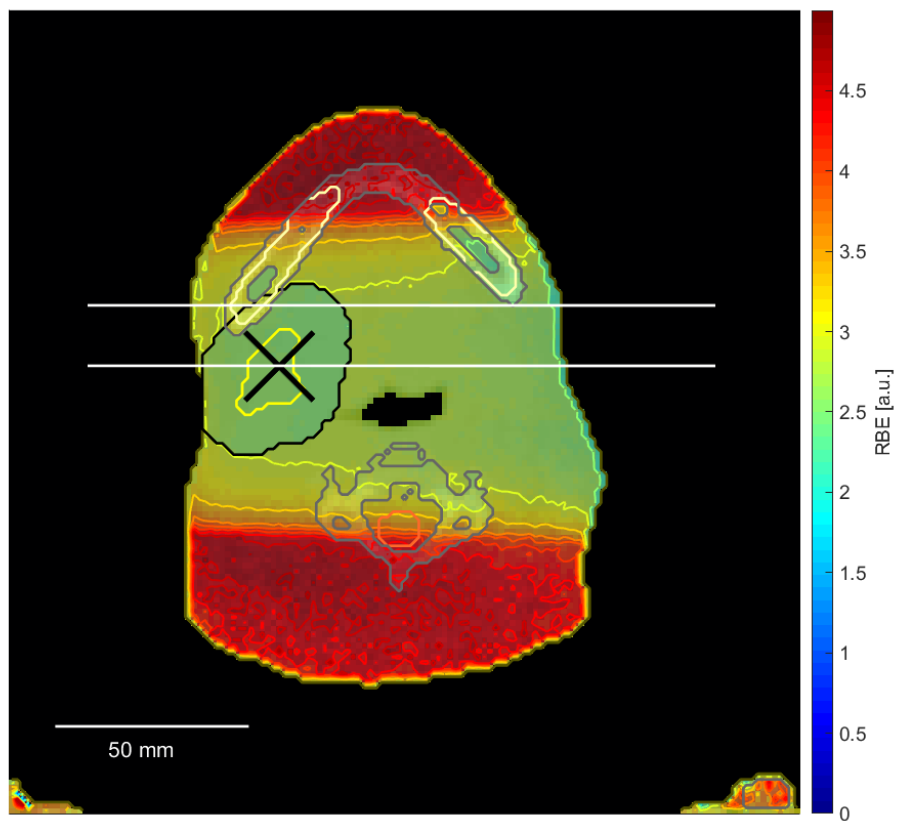
Figure 5.3: Result of retrospective RBE calculation using a combination of MCNP and MCDS for one fraction. Here, the PTV is indicated in black.
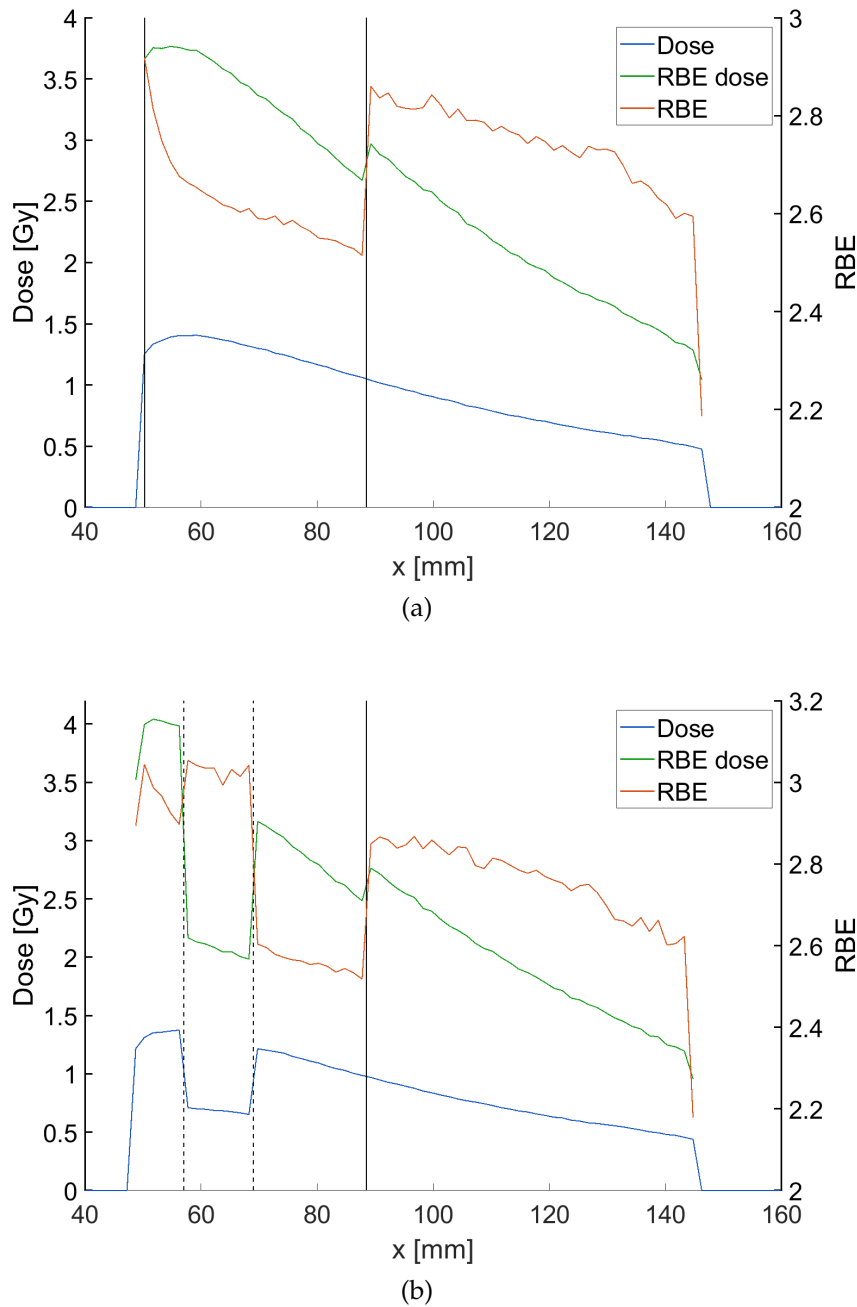
Figure 5.4: Depth profiles of dose and RBE-weighted dose curves (left ordinate) and RBE curve (right ordinate) calculated for retrospective calculation with contour specific $(\alpha/\beta)_R$-values. Curve (a) corresponds to the line through isocenter (black cross in figure 5.3) and curve (b) to the shifted line (upper line in figure 5.3). PTV extension in (a) indicated by solid black line and bone and PTV extension in (b) between dashed black lines and left dashed and solid line, respectively.

composition can be inspected in figure 5.4b where the beam also passes through bone. The depth-dependent bone extension is indicated by vertical dashed black lines and the PTV is limited by the right dashed line and the solid line. The region to the left of the left dashed line and to the right of the solid line contain material defined as soft tissue. For increasing depth in the patient - i.e. going from left to right in figure 5.4b through tissue regions of soft tissue, bone, PTV, and again soft tissue - the RBE values for adjacent voxels change by 5 %, less than -1 %, -14 % -3 %, and -13 %, respectively. Therefore, when comparing bone on the one hand and soft tissue or PTV on the other, not only the $(\alpha/\beta)_R$-values for the reference radiation influence the RBE values but also the material composition and the large variation in the dose level.

5.2.3 Discussion

While for fission neutrons with mean energy $\bar{E}_n = 1.9$ MeV a RBE of 2 to 7 was estimated by Schmid et al. [56] and the importance of RBE for the application of FNT at MEDAPP was for example highlighted by Specht et al. [64], organ- or tissue-specific RBE calculations were not available so far for an assessment of dose distributions and treatment scenarios. Even though a voxel-specific calculation of RBE is now conceptually available with the combination of the MC dose engine and the Monte Carlo damage simulation for the mixed neutron-gamma radiation field, neither a beam-specific verification of the RBE modelling in cell culture studies nor all input parameters are easily available for a clinical evaluation. Nevertheless, a modification of the input parameters for RBE calculations like fraction size D and $(\alpha/\beta)_R$ for the reference radiation is made available for post-processing in the implementation. A consideration of the impact of oxygenation conditions on RBE is also accessible from the two available extreme cases of hypoxic and aerobic environments.

Furthermore, the calculated RBE-weighted dose distributions and RBE values show once more the significance of RBE in FNT. For example, from figures 5.1 and 5.2 it is clear that caution is advisable when applying different dose levels due to large variations in RBE especially at low doses. This holds true for low doses on the central beam axis as well as for out-of-field regions where dose levels are also low.

Next steps for a potential verification and an integration of the presented calculation tool into retrospective studies for MEDAPP can only be performed in an interdisciplinary effort including radiation biology, medicine, and medical physics.

6 Conclusion and Outlook

In conclusion, the development and implementation of a treatment planning software for patient-specific 3D dose calculation was successfully realized in the presented work. In order to face the MEDAPP-specific challenges like the mixed neutron-gamma radiation field and the spatial extension of the source, two separate dose engines applying Monte Carlo methods and pencil beam kernels for dose calculation were embedded into the research treatment planning software matRad. Here, the final version of the dose engines in combination with the matRad environment provide a customized approach to perform the procedure of treatment plan calculation and evaluation for fast neutron therapy at MEDAPP. Especially for the considered neutron energy range up to 10 MeV, there is no reason to assume principle difficulties or inaccuracies with the Monte Carlo approach or the decomposed pencil beam kernels generated from simulated depth dose curves. The discussed validation efforts matched this expectation even though the validation of the dose calculation approaches was only possible to a limited extend and with reference to dose deposition in water.

In order to provide treatment planning on patient CT for MEDAPP, the suggested dose calculation methods provide complementary characteristics so that also principle prerequisites for the clinical workflow of radiation therapy could be matched. Time-efficient treatment planning for fast neutron therapy applying pencil beam algorithms was and is still used in clinical routine ([35] & [46]) and adequate correction procedures for fast neutron dose deposition in heterogeneous media were suggested in the past [63]. Therefore, strong background existed and could be used for the implementation of the dose engine based on pencil beam kernels. Regarding the dose engine based on Monte Carlo, the principle feasibility of the dose calculation and first steps towards a treatment planning software for MEDAPP applying the Monte Carlo code Geant4 were performed in a preceding doctoral thesis by Garny et al. (cf. [20], [22] & [23]). Picking up at the point to which these first steps had led, an automatic procedure for tissue segmentation based on Hounsfield unit intervals was added, the biological modeling for RBE calculations was extended applying the RMF-model, extensive effort was put into an easily accessible beam shaping interface, and the dose engine was integrated into the matRad treatment planning environment in order to support all steps from DICOM import to the evaluation and export of treatment plans. Here, MCNP was chosen over Geant4 in order to allow the use of existing beamline models for MEDAPP and to facilitate the intercomparison with Monte Carlo dose calculations performed at the University of Washington's fast neutron therapy facility. As a result, the overall good agreement between the time-efficient pencil beam dose engine and the more accurate Monte Carlo dose engine provides the basis for further dose calculation

efforts for MEDAPP. In addition to the physical dose calculation, the exchange with the UW also resulted in the implementation and integration of a mechanism-inspired RBE model into the Monte Carlo dose engine for the MEDAPP treatment field. Here, the general experimental trends could be matched by simulations. Regarding the verification of the physical dose calculation - which of course will also impact the verification of the RBE modeling - some known issues in the context of ionization chamber dosimetry applied at MEDAPP could be addressed in a pragmatic way. A profound investigation was not in the scope of this thesis and is rather part of the ongoing re-assessment of the dosimetry at MEDAPP. It is worthwhile to mention once again in the context of verification that the used gamma spectrum is of limited reliability.

Next steps regarding especially the verification but also the improvement of the simulation input can be clearly identified. For the verification of the treatment planning approaches focusing on neutron dose calculations, the most important next step will be the measurement of dose distributions in heterogeneous slab phantoms. A comparison between measurements in heterogeneous media and the simulated dose distributions will provide evidence on the remaining extent of necessary fine tuning of the presented dose calculation methods like for example in the tissue segmentation for Monte Carlo calculations. It is evident that this comparison will always depend on the simulation input. While the neutron spectrum is reliable for MEDAPP, the gamma spectrum should be measured or at least simulated in order to eliminate uncertainties in the comparison between measured and simulated dose. Unfortunately, this aspect is even more essential in case film dosimetry with no option to separate neutron and gamma dose should be used.

Since there is no reason to assume principle inaccuracies with the suggested dose calculation methods, going ahead and starting a retrospective investigation cross-referencing dose distributions calculated on CT data with patient follow-ups on fast neutron treatments performed at MEDAPP seems reasonable. Even though still under investigation, RBE calculations should be included in retrospective studies. Due to the provided ability to modify the input parameters of the RBE modeling after the time-consuming Monte Carlo calculations were run, correlations with observations in patient follow-ups could be investigated.

While a retrospective investigation might provide insight into the biological modeling of the mixed neutron-gamma beam RBE, an experimental verification should be pursued. In an interdisciplinary approach, the biological effects of the beam in different depth and therefore variable contributions from neutron and gamma dose deposition could be investigated. By defining a reasonable endpoint for such an investigation, a verification of the approach presented in this thesis could be aimed for.

As a result of the potential insights from the suggested next steps, a more elaborate background associated to current treatment indications could be gained and potentially even new treatment indications like for example in the context of BNCT could

be identified and investigated further.

Referring back to the aspects stressed by Jones to be critical for the success of fast neutron therapy, especially the first two on physically and biologically-weighted dose calculation were incorporated into this work. While neutron-hydrogen interactions are methodically included in dose calculations applying Monte Carlo simulations, it was also possible to account for heterogeneities in tissue composition by the applied correction method for the pencil beam algorithm. Furthermore, the contribution of secondary particles to the dose deposition in different tissues and different depths was made accessible by the Monte Carlo approach so that mechanism-inspired RBE modeling can be included. The third aspect on normal tissue damage and unintended side effects can now be addressed for fast neutron therapy at MEDAPP in the scope of a retrospective study on the basis of the presented treatment planning software.

Acknowledgments

Over the course of the doctoral thesis presented in the following, many people contributed on different ends to its successful realization. The project would not have been possible without the numerous scientific discussions, advises, suggestions, and support of all the people directly involved or simply just interested in its success. Special thanks goes to Prof. Jan J. Wilkens and Prof. Stephanie E. Combs from Klinikum rechts der Isar and Dr. Tobias Chemnitz from FRM II for their guidance as part of the thesis advisory committee. Prof. Wilkens' and Dr. Chemnitz' time and supportive critique in the proof reading process of this thesis and their commitment to the topic underlined in many additional discussions are highly appreciated. Furthermore, Dr. Markus Kellermeier's support in mentoring the presented project during the first month is also highly valued.

The dosimetry measurements partly discussed here were essential for the verification of the core dose calculations in this thesis. Dr. Chemnitz, Dr. Markus Kellermeier and Franz Wagner, all currently or formerly from FRM II, and Prof. Jan Wilkens and Severin Kampfer, both from Klinikum rechts der Isar, were involved in the revision of the dosimetry methods and/or the actual dosimetry measurements. For the revision of the dosimetry methods for MEDAPP, Dr. Kellermeier was the one who actually suggested the re-calibration of the dosimetry equipment and he also took the lead in performing the calibration measurements.

Models of the MEDAPP beamline for Monte Carlo simulations presented in the following were provided by Dr. Harald Breitkreutz formlerly from FRM II and Santiago Bazzana from the Argentine National Atomic Energy Commission. Even though not directly included in the simulations within this thesis, these models were highly valuable for the implementation of the discussed treatment planning approaches for MEDAPP.

The modeling of the biological effects of mixed neutron-gamma radiation as it is implemented in the Monte Carlo dose engine was suggested by Prof. Robert D. Stewart from the University of Washington. I would like thank him and Dr. Greg Moffitt, also from the UW, for their time for extensive discussions on biological modeling and their essential advice for the implementation of the models.

Besides the general support from people of the radiation oncology department of Klinikum rechts der Isar, Mathias Düsberg and Drazen Stajduhar, respectively, supported the visualization and evaluation of the calculated dose distributions by performing the treatment plan import into the clinical treatment planning software Eclipse and the contouring of additional risk organs, also in Eclipse.

Again, I would like to thank all the people involved in the project. I am grateful for the funding of my doctoral project by the German Research Foundation DFG and the opportunity to be part of DFG's research training group on advanced medical physics for image-guided cancer therapy (GRK 2274).

List of Figures

List of Tables

Own Publications and Ongoing Projects

Paper publications:

- Sommer, L., Kampfer, S., Chemnitz, T., Breitkreutz, H., Combs, S.E., Wilkens, J.J.: Therapeutic Dose Calculation for a Fission Neutron Source using Pencil Beam Kernels. Physics in Medicine and Biology, submitted in August 2022.

- Sommer, L., Chemnitz, T., Kampfer, S., Bausenwein, D., Beimler, A., Kellermeier, M., Schütz, R., Wilkens, J.J., Wagner, F.M.: A New Mulit Leaf Collimator for the Fission Neutron Therapy Facility at FRM II. Nuclear Instruments and Methods in Physics Research Section A: Accelerators, Spectrometers, Detectors and Associated Equipment, to be submitted in August/September 2022.

Conference contributions:

- Poster presentation at ESTRO: Development and Validation of a 3D Neutron Therapy Planning System for FRM II. (2020)

- Oral communication at ECMP: Development and Validation of a 3D Neutron Therapy Planning System for FRM II. (2021)

- Poster presentation at Dreiländertagung der ÖGMP, DGMP und SGSMP: Implementation and Verification of a 3D Neutron Therapy Planning Software for a Fission Neutron Source. (2021)

Contributions as co-author:

- Kumar, R., Sommer, L., Losko, A.S.: Gamma In Addition to Neutron Tomography (GIANT) at the NECTAR instrument. To be submitted in August 2022.

Ongoing projects:

- Bonete-Wiese, D., Sommer, L., Chemnitz, T., Röhrmoser, A., Reiter, C. et al.: Spectral characterization of the modified FRM II beamtube SR-10 using Monte Carlo methods. Ongoing since 2020.

- Sommer, L., Moffitt, G.B., Chemnitz, T., Combs, S.E., Wilkens, J.J., Stewart, R.D.: Benchmarking of RBE calculations for the FRM II fission neutron source and retrospective evaluation of calculated biological dose distributions. Ongoing since 2020.

- Alexander, F., Sommer, L., Schmid, T., Wilkens, J.J. et al.: A comparison between nanodosimetric and mechanistic inspired approaches to biological effectiveness of neutron radiation. Ongoing since 2021.

- Sommer, L., Düsberg, M., Chemnitz, T., Wilkens, J.J. et al.: Calculation of neutron dose deposition using the the RayStation photon beam model. Ongoing since 2022.

- Sommer, L, Bennan, A.B.A., Wikens, J.J., Wahl, N. et al.: Efforts to provide a ready-to-use integration of neutron dose calculation engines for FNT and BNCT into the research treatment planning software matRad. Ongoing since 2022.

Bibliography

[1] AAPM: Protocol for Neutron Beam Dosimetry (1980)

[2] Aljabab, S., Lui, A., Wong, T., Liao, J., Laramore, G., Parvathaneni, U.: A Combined Neutron and Proton Regimen for Advanced Salivary Tumors: Early Clinical Experience. Cureus **13**(5) (2021)

[3] Bangert, M., Ensminger, S.: Set of MATLAB functions computing the convolution kernels for a singular-value-decomposed pencil beam dose calculation algorithm. (2020). URL `https://github.com/e0404/photonPencilBeamKernelCalc[2021-09-21]`

[4] Barth, R.F., Zhang, Z., Liu, T.: A Realistic Appraisal of Boron Neutron Capture Therapy as a Cancer Treatment Modality. Cancer Communications **38**(1), 1–7 (2018)

[5] Bazzana, S.: MCNP model of MEDAPP with MLC 3 provided in personal communication. (2018)

[6] Bedford, J.L.: Calculation of Absorbed Dose in Radiotherapy by Solution of the Linear Boltzmann Transport Equations **64**(2), 02TR01 (2019). DOI 10.1088/1361-6560/aaf0e2. URL `https://doi.org/10.1088/1361-6560/aaf0e2`

[7] Berger M.J.and Coursey, J.Z.M., Chang, J.: ESTAR, PSTAR, and ASTAR: Computer Programs for Calculating Stopping-Power and Range Tables for Electrons, Protons, and Helium Ions (version 1.2.3). (2005). URL `http://physics.nist.gov/Star[2021-09-16]`

[8] Bortfeld, T., Schlegel, W., Rhein, B.: Decomposition of Pencil Beam Kernels for Fast Dose Calculations in Three-Dimensional Treatment Planning. Medical Physics **20**(2), 311–318 (1993)

[9] Breitkreutz, H.: Spektrale Charakterisierung des Therapiestrahls am FRM II (2007)

[10] Breitkreutz, H.: Neutron and gamma spectrum provided in personal communication. (2018)

[11] Breitkreutz, H., Wagner, F.M., Röhrmoser, A., Petry, W.: Spectral Fluence Rates of the Fast Reactor Neutron Beam MedApp at FRM II. Nuclear Instruments and

Methods in Physics Research Section A: Accelerators, Spectrometers, Detectors and Associated Equipment **593**(3), 466–471 (2008)

[12] Buzug, T.M.: Computed Tomography. In: Springer Handbook of Medical Technology, pp. 311–342. Springer (2011)

[13] Carlson, D.J., Stewart, R.D., Semenenko, V.A., Sandison, G.A.: Combined use of Monte Carlo DNA Damage Simulations and Deterministic Repair Models to Examine Putative Mechanisms of Cell Killing. Radiation Research **169**(4), 447–459 (2008)

[14] Chadwick, M.B., Herman, M., Obložinskỳ, P., Dunn, M.E., Danon, Y., Kahler, A., Smith, D.L., Pritychenko, B., Arbanas, G., Arcilla, R., et al.: ENDF/B-VII. 1 Nuclear Data for Science and Technology: Cross Sections, Covariances, Fission Product Yields and Decay Data. Nuclear Data Sheets **112**(12), 2887–2996 (2011)

[15] Chandra, S., Ahmad, T., Barth, R., Kabalka, G.: Quantitative Evaluation of Boron neutron Capture Therapy (BNCT) Drugs for Boron Delivery and Retention at Subcellular-Scale Resolution in Human glioblastoma Cells with Imaging Secondary Ion Mass Spectrometry (SIMS). Journal of microscopy **254**(3), 146–156 (2014)

[16] Coderre, J.A., Makar, M.S., Micca, P.L., Nawrocky, M.M., Liu, H.B., Joel, D.D., Slatkin, D.N., Amols, H.I.: Derivations of Relative Biological Effectiveness for the High-LET Radiations Produced During Boron Neutron Capture Irradiations of the 9L Rat Gliosarcoma in Vitro and in Vivo. International Journal of Radiation Oncology* Biology* Physics **27**(5), 1121–1129 (1993)

[17] Dale, R.G., Jones, B.: The Assessment of RBE Effects using the Concept of Biologically Effective Dose. International Journal of Radiation Oncology - Biology - Physics **43**(3), 639–645 (1999)

[18] DeMarco, J., Solberg, T., Smathers, J.B.: A CT-based Monte Carlo Simulation Tool for Dosimetry Planning and Analysis. Medical Physics **25**(1), 1–11 (1998)

[19] DIN: DIN 6802-6:2013-01: Neutron Dosimetry – Part 6, Methods for Determination of Absorbed Dose using Ionisation Chambers (2013)

[20] Garny, S.: Development of a Biophysical Treatment Planning System for the FRM II Neutron Therapy Beamline (2009)

[21] Garny, S., Mares, V., Roos, H., Wagner, F., Rühm, W.: Measurement of Neutron Spectra and Neutron doses at the Munich FRM II therapy beam with Bonner spheres. Radiation Measurements **46**(1), 92–97 (2011)

[22] Garny, S., Rühm, W., Wagner, F., Paretzke, H.: Neutron Therapy at the FRM II - Calculation of Dose inside a Voxel Phantom. In: World Congress on Medical Physics and Biomedical Engineering, September 7-12, 2009, Munich, Germany, pp. 437–440. Springer (2009)

[23] Garny, S., Rühm, W., Zankl, M., Wagner, F.M., Paretzke, H.G.: First Steps Towards a Fast-Neutron Therapy Planning Program. Radiation Oncology **6**(1), 1–12 (2011)

[24] Goorley, J.T., James, M.R., Booth, T.E., Brown, F.B., Bull, J.S., Cox, L.J., Durkee, J.W.J., Elson, J.S., Fensin, M.L., Forster, R.A.I., Hendricks, J.S., Hughes, H.G.I., Johns, R.C., Kiedrowski, B.C., Martz, R.L., Mashnik, S.G., McKinney, G.W., Pelowitz, D.B., Prael, R.E., Sweezy, J.E., Waters, L.S., Wilcox, T., Zukaitis, A.J.: Initial MCNP6 Release Overview - MCNP6 version 1.0. Los Alamos National Laboratory, Los Alamos, NM, LA-UR-13-22934 (2013)

[25] Gray, L.H.: An Ionization Method for the Absolute Measurement of γ-Ray Energy. Proceedings of the Royal Society of London. Series A-Mathematical and Physical Sciences **156**(889), 578–596 (1936)

[26] Hough, J.: A Modified Lead Attenuation Method to Determine the Fast Neutron Sensitivity kU of a Photon Dosemeter. Physics in Medicine & Biology **24**(4), 734 (1979)

[27] Hughes, H.G.: MCNP/X Transport in the Tabular Regime. In: AIP Conference Proceedings, vol. 896, pp. 91–101. American Institute of Physics (2007)

[28] ICRU: Report 26. Journal of the International Commission on Radiation Units and Measurements **os14**(1) (1976)

[29] ICRU: Report 45. Journal of the International Commission on Radiation Units and Measurements **os23**(2) (1989)

[30] ICRU: Report 46: Photon, Electron, Proton and Neutron Interaction Data for Body Tissues. Journal of the International Commission on Radiation Units and Measurements **os24**(1) (1992)

[31] ICRU: Report 63: Nuclear Data for Neutron and Proton Radiotherapy and for Radiation Protection. Journal of the International Commission on Radiation Units and Measurements **os32**(2) (2000)

[32] Jones, B.: The Apparent Increase in the β-Parameter of the Linear Quadratic Model with Increased Linear Energy Transfer during Fast Neutron Irradiation. The British Journal of Radiology **83**(989), 433–436 (2010)

[33] Jones, B.: Clinical Radiobiology of Fast Neutron Therapy: What was learned? Frontiers in Oncology **10**, 1537 (2020)

[34] Jungwirth, M., Breitkreutz, H., Wagner, F., Bücherl, T.: Determination of the Photon Spectrum in an Intense Fission Neutron Beam. Journal of Instrumentation **7**(03), C03022 (2012)

[35] Kalet, A.M., Sandison, G.A., Phillips, M.H., Parvathaneni, U.: Validation of the Photon Convolution-Superposition Algorithm applied to Fast Neutron Beams. Journal of Applied Clinical Medical Physics **14**(6), 133–154 (2013)

[36] Kampfer, S.: Umfassende Charakterisierung eines Spaltneutronenstrahls. Diploma thesis, Technical University of Munich (2006)

[37] Kellerer, A.M., Rossi, H.H.: A Generalized Formulation of Dual Radiation Action. Radiation Research **75**(3), 471–488 (1978)

[38] Landau, L.D., Lifschitz, E.D.: Lehrbuch der theoretischen Physik in zehn Bänden: Mechanik. 1. Verlag Harri Deutsch, Frankfurt a. M. (2007)

[39] Leroy, C., Rancoita, P.G.: Principles of Radiation Interaction in Matter and Detection, 4 edn. World Scientific, New Jery (2016)

[40] Loap, P., Kirova, Y.: Fast Neutron Therapy for Breast Cancer Treatment: An Effective Technique Sinking into Oblivion (2021)

[41] Low, D.A., Harms, W.B., Mutic, S., Purdy, J.A.: A Technique for the Quantitative Evaluation of Dose Distributions. Medical Physics **25**(5), 656–661 (1998)

[42] Macomber, M.W., Tarabadkar, E.S., Mayr, N.A., Laramore, G.E., Bhatia, S., Tseng, Y.D., Liao, J., Arbuckle, T., Nghiem, P., Parvathaneni, U.: Neutron Radiation Therapy for Treatment of Refractory Merkel Cell Carcinoma. International Journal of Particle Therapy **3**(4), 485–491 (2017)

[43] MATLAB: version 9.7.0.1319299 (R2019b). The MathWorks Inc., Natick, Massachusetts (2019)

[44] McMahon, S.J.: The Linear Quadratic Model: Usage, Interpretation and Challenges. Physics in Medicine & Biology **64**(1), 01TR01 (2018)

[45] Moffitt, G.B., Stewart, R.D., Sandison, G.A., Goorley, J.T., Argento, D.C., Jevremovic, T.: MCNP6 Model of the University of Washington Clinical Neutron Therapy System (CNTS). Physics in Medicine & Biology **61**(2), 937 (2016)

[46] Moffitt, G.B., Wootton, L.S., Hårdemark, B., Sandison, G.A., Laramore, G.E., Parvathaneni, U., Stewart, R.D.: Scattering Kernels for Fast Neutron Therapy Treatment Planning. Physics in Medicine & Biology **65**(16), 165009 (2020)

[47] NIST: National Institute of Standards and Technology: Material Composition Data. URL `https://physics.nist.gov/cgi-bin/Star/compos.pl?matno=001`[2022-01-11]

[48] NIST: National Institute of Standards and Technology: Material Composition Data. URL `https://www.nist.gov/pml/x-ray-mass-attenuation-coefficients`[2022-01-11]

[49] Nolte, R., Thomas, D.J.: Monoenergetic Fast Neutron Reference Fields: I. Neutron Production. Metrologia **48**(6), S263 (2011)

[50] Nolte, R., Thomas, D.J.: Monoenergetic Fast Neutron Reference Fields: II. Field Characterization. Metrologia **48**(6), S274 (2011)

[51] Podgoršak, E.B.: Radiation Physics for Medical Physicists, 1 edn. Springer (2006)

[52] Podgoršak, E.B.: Radiation Physics for Medical Physicists, 3 edn. Springer (2016)

[53] Reinhardt, S., Hillbrand, M., Wilkens, J., Assmann, W.: Comparison of Gafchromic EBT2 and EBT3 films for Clinical Photon and Proton Beams. Medical Physics **39**(8), 5257–5262 (2012)

[54] Rinard, P.: Neutron Interactions with Matter. Passive Nondestructive Assay of Nuclear Materials (375-377) (1991)

[55] Schlegel-Bickmann, D., Brede, H., Guldbakke, S., Lewis, V., Zoetelief, J.: Measurement of kU Values of Argon-Filled Magnesium Ionisation Chambers. Physics in Medicine & Biology **35**(6), 717 (1990)

[56] Schmid, E., Schlegel, D., Guldbakke, S., Kapsch, R.P., Regulla, D.: RBE of Nearly Monoenergetic Neutrons at Energies of 36 keV–14.6 MeV for Induction of Dicentrics in Human Lymphocytes. Radiation and Environmental Biophysics **42**(2), 87–94 (2003)

[57] Schmid, E., Wagner, F., Romm, H., Walsh, L., Roos, H.: Dose-Response Relationship of Dicentric Chromosomes in Human Lymphocytes obtained for the Fission Neutron Therapy Facility MEDAPP at the Research Reactor FRM II. Radiation and Environmental Biophysics **48**(1), 67–75 (2009)

[58] Schneider, U., Pedroni, E., Lomax, A.: The Calibration of CT Hounsfield Units for Radiotherapy Treatment Planning. Physics in Medicine & Biology **41**(1), 111 (1996)

[59] Schneider, W., Bortfeld, T., Schlegel, W.: Correlation between CT Numbers and Tissue Parameters needed for Monte Carlo Simulations of Clinical Dose Distributions. Physics in Medicine & Biology **45**(2), 459 (2000)

[60] Semenenko, V., Stewart, R.: A Fast Monte Carlo Algorithm to Simulate the Spectrum of DNA Damages Formed by Ionizing Radiation. Radiation Research **161**(4), 451–457 (2004)

[61] Semenenko, V., Stewart, R.: Fast Monte Carlo Simulation of DNA Damage Formed by Electrons and Light Ions. Physics in Medicine & Biology **51**(7), 1693 (2006)

[62] Siddon, R.L.: Fast Calculation of the Exact Radiological Path for a Three-Dimensional CT Array. Medical Physics **12**(2), 252–255 (1985)

[63] Söderberg, J., Carlsson, G.A., Ahnesjö, A.: Monte Carlo Evaluation of a Photon Pencil Kernel Algorithm Applied to Fast Neutron Therapy Treatment Planning. Physics in Medicine & Biology **48**(20), 3327 (2003)

[64] Specht, H.M., Neff, T., Reuschel, W., Wagner, F.M., Kampfer, S., Wilkens, J.J., Petry, W., Combs, S.E.: Paving the Road for Modern Particle Therapy–What can we learn from the experience gained with fast Neutron Therapy in Munich? Frontiers in Oncology **5**, 262 (2015)

[65] Stewart, R.D.: Monte Carlo Damage Simulation (MCDS) Software. (2011). URL `http://faculty.washington.edu/trawets/mcds/` [2022-01-25]

[66] Stewart, R.D.: Model implementation suggested in personal communication. (2020)

[67] Stewart, R.D., Carlson, D.J., Butkus, M.P., Hawkins, R., Friedrich, T., Scholz, M.: A Comparison of Mechanism-Inspired Models for Particle Relative Biological Effectiveness (RBE). Medical Physics **45**(11), e925–e952 (2018)

[68] Stewart, R.D., Streitmatter, S.W., Argento, D.C., Kirkby, C., Goorley, J.T., Moffitt, G., Jevremovic, T., Sandison, G.A.: Rapid MCNP Simulation of DNA Double Strand Break (DSB) Relative Biological Effectiveness (RBE) for Photons, Neutrons, and Light Ions. Physics in Medicine & Biology **60**(21), 8249 (2015)

[69] Stewart, R.D., Yu, V.K., Georgakilas, A.G., Koumenis, C., Park, J.H., Carlson, D.J.: Effects of Radiation Quality and Oxygen on Clustered DNA Lesions and Cell Death. Radiation Research **176**(5), 587–602 (2011)

[70] Streitmatter, S.W., Stewart, R.D., Moffitt, G., Jevremovic, T.: Mechanistic Modeling of the Relative Biological Effectiveness of Boron Neutron Capture Therapy. Cells **9**(10), 2302 (2020)

[71] Suzuki, M.: Boron Neutron Capture Therapy (BNCT): a Unique Role in Radiotherapy with a View to Entering the Accelerator-based BNCT Era. International journal of clinical oncology **25**(1), 43–50 (2020)

[72] matRad developer team: matRad wiki documentation on GitHub. (2021). URL `https://github.com/e0404/matRad/wiki` [2021-11-23]

[73] Treeby, B.E., Cox, B.T.: k-Wave: MATLAB Toolbox for the Simulation and Re-construction of Photoacoustic Wave Fields. Journal of Biomedical Optics **15**(2), 021314 (2010)

[74] Van Leeuwen, C., Oei, A., Crezee, J., Bel, A., Franken, N., Stalpers, L., Kok, H.: The Alfa and Beta of Tumours: A Review of Parameters of the Linear-Quadratic Model, Derived from Clinical Radiotherapy studies. Radiation oncology **13**(1), 1–11 (2018)

[75] Wagner, F., Kampfer, S., Kneschaurek, P.: Bericht zur Basisdosimetrie für medizinische Bestrahlung an der Strahlkonverteranlage am FRM II in Garching. (2006)

[76] Wagner, F.M., Breitkreutz, H., Loeper-Kabasakal, B., Specht, H.: Fast Neutron Therapy: A Status Report. Sibirskiy Onkologicheskiy Zhurnal **6**(IMPULSE-2017-00167), 5–12 (2015)

[77] Wagner, F.M., Kneschaurek, P., Kastenmüller, A., Loeper-Kabasakal, B., Kampfer, S., Breitkreutz, H., Waschkowski, W., Molls, M., Petry, W.: The Munich Fission Neutron Therapy Facility MEDAPP at the Research Reactor FRM II. Strahlentherapie und Onkologie **184**(12), 643–646 (2008)

[78] Werner, C., Bull, J., Solomon, C., Brown, F., McKinney, G., Rising, M., Dixon, D., Martz, R., Hughes, H., Cox, L., Zukaitis, A., Armstrong, J., Forster, R.A., Casswell, L.: MCNP Version 6.2 Release Notes. Los Alamos National Laboratory, Los Alamos, NM, LA-UR-18-20808 (2018)

[79] Werner, C.J.: MCNP Users Manual-Code Version 6.2. Los Alamos National Laboratory, Los Alamos, NM, LA-UR-17-29981 (2017)

[80] Wieser, H.P., Cisternas, E., Wahl, N., Ulrich, S., Stadler, A., Mescher, H., Müller, L.R., Klinge, T., Gabrys, H., Burigo, L., et al.: Development of the Open-Source Dose Calculation and Optimization Toolkit matRad. Medical Physics **44**(6), 2556–2568 (2017)

[81] X-5 Monte Carlo Team: MCNP A General Monte Carlo N-Particle Transport Code Version 5 Volume I: Overview and Theory. Los Alamos National Laboratory, Los Alamos, NM, LA-UR-03-1987 (2003)

[82] Zieb, K., Hughes, H., James, M., Xu, X.: Review of Heavy Charged Particle Transport in MCNP6.2. Nuclear Instruments and Methods in Physics Research Section A: Accelerators, Spectrometers, Detectors and Associated Equipment **886**, 77–87 (2018)